Optimal Control of a Floating Wind Farm Based on Turbine Repositioning

Z. Xie

Master of Science Thesis

TU Delft Delft University of Technology

Delft Center for Systems and Control

Optimal Control of a Floating Wind Farm Based on Turbine Repositioning

Master of Science Thesis

For the degree of Master of Science in Systems and Control at Delft University of Technology

Z. Xie

July 3, 2024

Faculty of Mechanical, Maritime and Materials Engineering (3mE) · Delft University of Technology

Delft University of Technology
Department of
Delft Center for Systems and Control (dcsc)

The undersigned hereby certify that they have read and recommend to the Faculty of Mechanical, Maritime and Materials Engineering (3mE) for acceptance a thesis entitled

Optimal Control of a Floating Wind Farm Based on Turbine Repositioning

by

Z. Xie

in partial fulfillment of the requirements for the degree of

Master of Science Systems and Control

Dated: July 3, 2024

Supervisor(s):

prof.dr.ir. J.W. van Wingerden

ir. D.G. van den Berg

ir. M. Becker

Reader(s):

dr.ir. A. Jarquin Laguna

dr. F. Taruffi

Abstract

This thesis investigates the concept of turbine repositioning to enhance energy production in floating wind farms. Due to the dense deployment of floating turbines, downstream units could potentially experience reduced wind speeds caused by the wakes of upstream turbines, leading to decreased power output—an effect known as the wake effect. To address this, methods such as power de-rating and yaw-based wake redirection have been extensively studied. Notably, for floating wind farms, the ability of turbine bases to move within a certain range has prompted the proposal of turbine repositioning as a novel wake mitigation strategy.

This study delves into optimal control strategies for turbine repositioning, with a particular emphasis on manipulating rotor yaw angles. It introduces two primary repositioning strategies: static repositioning, suitable for farms with relatively slack mooring lines, and dynamic repositioning, for those with tighter lines. Alongside, the research proposes optimization methods to identify the optimal control sequences for each repositioning strategy. Lastly, by analyzing rotor yaw angle control sequences in the frequency domain, this study distinguishes the frequency component crucial for repositioning turbines from that steering the wakes. The findings provide significant insights into enhancing the cost-effectiveness of power production in floating wind farms through effective wake interaction management.

Table of Contents

Acknowledgements

In the past year, I had a great time working on this thesis. Looking back, I am extremely fortunate to have a bunch of amazing people who helped me get here.

First, I'd like to thank Jan-Willem van Wingerden. Thank you for introducing me to the world of wind energy and providing top-notch opportunities for academic interaction. You never hesitated to compliment my work, and whether you realized it or not, those moments played a significant role in helping me overcome public speaking anxiety.

Next, I'd like to thank Daniel van den Berg and Marcus Becker. Your incredible ideas and constructive criticism during our weekly meetings have been one of the most amazing aspects of this journey. Sometimes I zoned out (I apologize) during our discussions, only to find myself thinking, "Wow, that's a brilliant point. I hope I can attain that level of depth and breadth in my thinking one day." Additionally, Daniel, I hereby acknowledge your music taste. Having a supervisor who also listens to Carly Rae Jepsen means a lot to me.

Then, I want to thank my parents for their unconditional love and support. Over the past year, you've said "Good job, kid" to me many times, and I remember every one of those moments. Thank you for being there for me 24/7 and for being such wonderful role models.

Last but not least, a big thank you to Lingbo, Chenyang, and Chengjian. Thank you for picking up my FaceTime calls and enduring my endless yappings. The special bonds we've forged are treasures I will hold close to my heart always.

Delft, University of Technology — Z. Xie
July 3, 2024

“Coming in like a western wind
Do you feel home from all directions?”

— *Carly Rae Jepsen*

Chapter 1

Introduction

1-1 Background and Significance

Wind energy is entering people's attention at an unprecedented speed. The website *Our World in Data* [79] produced a graphical representation delineating the global primary energy consumption across various energy sources, see Figure 1-1. Within this representation, one can see the historical and contemporary trajectory of human utilization of wind power.

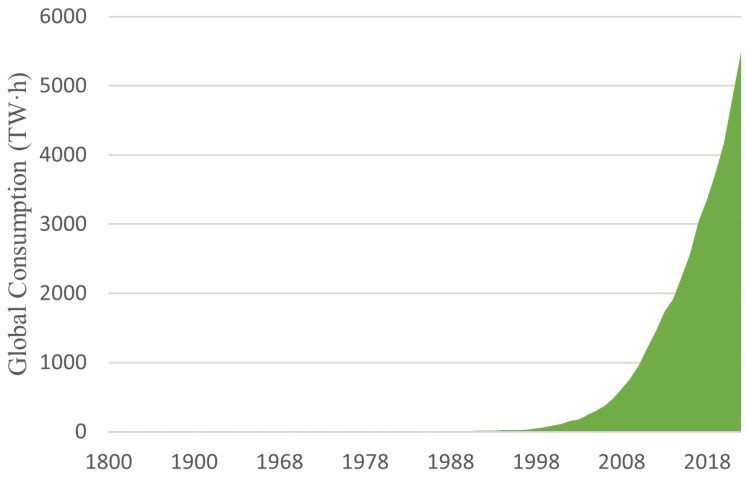

Figure 1-1: Global Wind Energy Consumption from 1800 to 2022 [79]

The booming development of wind energy is the result of the combined effects of multiple factors. On December 12, 2015, 175 parties signed a legally binding international treaty on climate change in Paris, France - the Paris Agreement. The overall goal of the agreement is "to limit the increase in the global average temperature to well below 2°C above pre-industrial levels," and to make efforts "to limit the temperature increase to 1.5°C above pre-industrial levels" [95]. To achieve the goals of the Paris Agreement, global decarbonization between 2022

and 2030 is essential [84], which has spurred the sustainable energy transition. The current energy transition specifically refers to shifting the power supply from fossil fuels to renewable energies, with the growth in renewable energies nowadays primarily relying on wind and solar power. Research indicates that to achieve net-zero greenhouse gas emissions by the middle of this century, the global penetration rate of wind energy must increase from 5% to 35% [46]. From the perspective of achieving policy goals, the successful development of wind energy plays a decisive role.

Additionally, external economic forces are also driving the development of the wind power industry. On one hand, the pursuit of lower electricity prices has never ceased, and on the other hand, the fact that wind energy is in a developmental stage and requires more investment hinders the reduction of electricity generation costs. Current research indicates that the cost of onshore wind power generation ranges between 4.5 to 8.7 Euro cents/kWh, while offshore wind power, due to its higher uncertainty, has generation costs between 6 to 11.1 Euro cents/kWh [16]. A study from 2007 estimated the generation costs of natural gas and coal to be 4.9 and 4.1 Euro cents/kWh, respectively [70]. Clearly, wind power is at a slight disadvantage in terms of generation costs. However, research by Blanco et al. suggests that if the costs associated with CO2 emissions are also factored into the generation costs of natural gas or coal, wind power would become a more cost-effective option [15]. In addition, the future trend of wind power costs is very optimistic. Numerous studies based on the wind energy learning curve suggest that the cost of wind power generation will further decrease with the increase in capacity and technological advancements [102, 26, 74].

1-2 Introduction to Floating Wind Farms

1-2-1 Onshore vs. Offshore Wind Turbines

Based on the location, wind turbines can be divided into onshore and offshore wind turbines. At early stage, onshore wind turbines have many inherent advantages: low installation costs, low maintenance costs, small investment risks, and relatively mature technology [14, 25].

However, the further expansion of onshore wind turbines faces numerous obstacles, for instance, residents' dissatisfaction with the noise and shadow flicker caused by wind turbines, conflicts between wind turbine sites and nature reserves, saturation of wind farms in certain areas, and the impact on local property values [32]. These surface manifestations can ultimately be summarized into two reasons: if one wants to increase the number of wind turbines, the demand for more land is not easily met; if the goal is to increase the power output of each turbine, the wind energy resources available on land may not be economically sufficient to support larger turbines.

Fortunately, where there are challenges, there are opportunities. Offshore wind energy technology provides solutions to these challenges to a certain extent. The ocean offers a broad area for wind turbines. Although site selection still needs to compete with industries such as fishing, transportation, and oil, the vast expanse and fewer uses of the ocean result in offshore wind turbines facing fewer land use restrictions. Additionally, a public opinion survey showed that there is a positive correlation between the distance of offshore wind farms from residential areas and people's support for establishing wind farms [71]. Offshore wind not only generally

has higher wind speeds than onshore wind but is also more consistent [65]. Coupled with the vast available sea area, this makes the wind resources at sea extremely abundant. A study assessing the offshore wind energy potential around Michigan concluded that if the maximum water depth is limited to 60 meters, the estimated offshore generation capacity could reach 102,592 MW; if the depth limit is extended to 200 meters, the estimated offshore generation capacity could reach 269,562 MW, which is 16 times greater than the onshore wind potential [2]. Besides, due to the lower roughness of the sea level compared to land, the wind shear over the sea is weaker, which imposes less requirement on the tower height of wind turbines [25]. These unique advantages endow offshore wind energy harnessing with inherent potential, especially with the continuous improvement of related supporting technologies over the past two decades.

Undoubtedly, offshore wind farms still have their unique challenges to overcome. Here, we focus on the challenge of installing bottom-fixed offshore wind turbines. When the water depth exceeds 50m, the sharp rise in installation costs and the limitations of seabed conditions make the deployment of bottom-fixed wind turbines economically unfeasible. The introduction of floaters and mooring systems has brought a glimmer of hope in solving this problem.

1-2-2 Advantages and Challenges of Floating Wind Turbines

Floating wind turbines are currently in the initial stages of commercialization. As of 2023, there are four floating wind farms in operation: Hywind Scotland and Kincardine in Scotland, WindFloat Atlantic in Portugal, and Hywind Tampen in Norway. The existing installation capacity of these turbines is a mere drop in the ocean compared to the global wind turbine installations. However, the fact that they have begun to be commercialized to some extent indicates the unique potential of this technology.

Here, we briefly introduce the three advantages of floating wind turbines: suitability for deep water, reduced transmission distances, and less environmental impacts. As previously mentioned, the initial intent behind introducing floating wind turbines was to address the limitation of bottom-fixed offshore turbines that cannot operate in deep waters. It is precisely this feature that grants floating turbines their greatest advantage — suitable for deep water. In Section 1-2-1, we referred to a study on the wind energy resources of Lake Michigan [2]. The study highlighted that due to the technical limitations of bottom-fixed turbines, wind energy in waters deeper than 60 meters, which constitutes almost 60% of the total wind energy resource, remains untapped. This case exemplifies how the advent of floating wind turbines could possibly overcome the technical constraints, enabling the harnessing of more wind energy and thereby potentially increasing the capacity factor. Secondly, floating turbines can reduce transmission distances for specific power generation tasks. This is achieved by situating floating power plants near load centers. A prime example is the Hywind Tampen wind farm [27], which is set up to provide power to offshore oil and gas installations. Hywind Tampen is located 140km off the coast of Norway in waters with depths of 260-300 meters. The floating setup enables it to be positioned near two load centers, thereby reducing transmission costs. Thirdly, floating wind turbines could potentially be more environmentally friendly towards marine life. Bottom-fixed wind turbines generate significant noise during the pile-driving process for tower installation, potentially disrupting the behavior of marine mammals within several kilometers and possibly causing hearing impairments at close distances [67].

In contrast, the installation of floating wind turbines involves merely securing anchors to the seabed, which generates less noise [69]. Additionally, the smaller size of the mooring lines could potentially have a lesser impact on the migration of seabed creatures.

Floating wind turbine technology also presents its own set of challenges. For example, for spar-type floating wind turbines, heavy-lift vessels and sheltered areas are required for installation and major repairs [63]. For Tension Leg Platform (TLP) type floating wind turbines, the design often necessitates on-site repairs. This is primarily because unhooking them for off-site maintenance can be challenging and complex due to their tension leg mooring systems [22]. Additionally, floating wind turbines need to consider platform stabilization and load reduction. The wind at sea and the waves acting on the turbine can potentially produce low-frequency excitation. If these environmentally-induced frequencies are close to the wind turbine's inherent frequencies, such as the first tower frequency or tower tilt rotation frequency, it can lead to significant vibration or platform motion. This phenomenon is also referred to as negative damping. Therefore, numerous studies have proposed solutions to prevent this phenomenon, such as using pole placement to reduce controller frequency [61], and employing methods inspired by Non-Minimum Phase Zeros compensation [52]. The need for load reduction work arises due to the more severe offshore conditions, which subject wind turbines to greater aerodynamic load asymmetry. Higher turbulence can lead to micro-cracking in the blades [82]. In response to this, many studies have employed independent pitch control strategies to balance the loads and restore platform torque [72, 73, 78].

1-3 The Wake Effect

When an upstream wind turbine harvests a portion of the available energy in the wind, the wind speed in the area behind its rotor decreases due to conservation of energy. When this air mass, which has a velocity less than the free stream, reaches the swept area of a downstream wind turbine, the production output of that downstream wind turbine is diminished. This effect is called the wake effect [60].

1-3-1 Impact of the Wake Effect

For a turbine as an individual, the wake effect increases the mechanical load on the downstream turbine due to the inevitable additional turbulence in the wake region, which in turn affects the service life and maintenance costs [92][62][31]. For wind farms, the overall energy yield is reduced by the wake effect [39][7], as the distance between turbines may not be as far as possible due to a variety of factors, such as government land zoning restrictions or transmission cost constraints. Moreover, numerous studies have quantified the reduction in wind farm efficiency resulting from wake effects. Barthelmie et al.'s researchs compared various Computational Fluid Dynamics (CFD) wake models in terms of their predictions of wind farm efficiency [8, 6]. The comprehensive results, based on data from the Horns Rev wind farm, indicated that for certain flow directions, wake losses amount to 10-20%. Their research also indicated that engineering wake models often underestimate the reduction in wind farm efficiency due to wake effects, whereas CFD models tend to overestimate wake losses. Therefore, accurate modeling of wakes is crucial for optimizing power output, although atmospheric conditions or interactions between turbines can complicate the modeling.

1-3-2 Existing Control-Oriented Wake Models

Modeling of fluid dynamics always involves a trade-off between accuracy and computation time, and this is no exception for wake modeling. Thus, current research categorizes wake models into high, medium, and low fidelity based on their precision.

High-fidelity wake models use Large Eddy Simulation (LES), which computes by solving the 3D Navier-Stokes equations, including SOWFA [23], UTDWF [68], etc. However, the high precision comes with lengthy computation times, taking several days or even weeks [18]. Clearly, these types of models are not suitable for real-time control. However, one advantage of these models is that they can be used for control method validation or the verification of low-fidelity wake models. To reduce computational load for control algorithm research, some studies have shifted towards wake models based on solving unsteady 2D Navier-Stokes equations, which are categorized as medium-fidelity models. Among them, WFSim developed by Boersma et al. [17] is a typical example of this type of model. The model uses a simplified turbulence model to improve accuracy. Additionally, although the model neglects the vertical dimension states, the correction terms added to the continuity equation partially mitigate the adverse effects of completely ignoring vertical information. Compared to high-fidelity models, this model significantly improves computational speed; for instance, a 1000s simulation approximately requires 1000s of computation time [57].

From the perspective of the control objectives, since retaining wake information in the X-Y plane is essential, further dimensional reduction from the 2D Navier-Stokes equations is not viable, necessitating the exploration of alternative approaches. Instead of using numerical calculation methods to solve the dynamics of the wake, research has been conducted using parameters to represent and simulate the behavior of the wake, such as wake deficit, wake expansion, centerline, etc. In 1983, Jensen [48] used a linearly expanding model to represent the expansion of the wake, becoming the forerunner of many subsequent analytical wake loss models. Jensen's model, also known as Park's model, adjusts the spread angle to fit data at distances larger than 4D (where D is the diameter of the wind turbine rotor) [53]. This approach results in large errors in the near wake zone, but their reasonable assumption that turbines are seldom placed closer than 4D justified that there is no need to worry about the large prediction error in the near wake zone. Although Jensen's model is not capable of predicting the redirected wake from rotor yawing and handling heterogeneous wind conditions, it has inspired research aimed at developing more accurate and comprehensive parametric control-oriented models.

The FLOw Redirection and Induction in Steady-state (FLORIS) model [34] is an extension of Jensen's model, integrating research from Jiménez et al. [49] to include wake deflection. FLORIS introduces more parameters to characterize the wake's decay, deflection, and expansion, and compared to Jensen's model, it better simulates situations with partial wake overlap. The parameters of the FLORIS model are fitted using data from the previously mentioned high-fidelity model SOWFA. A CFD simulation study demonstrates that FLORIS is capable of predicting the power output of each wind turbine in a wind farm with sufficient accuracy under various wind farm configurations [34]. However, the FLORIS model is susceptible to changing atmospheric conditions, thus, further parameter calibration, either online or offline, is still an ongoing topic for FLORIS [96, 20, 104].

Both Jensen's model and FLORIS can only describe the wake under steady-state conditions.

For floating wind farms, since this project involves the optimization control of the repositioning transient process, the dynamic changes in the wake caused by changes in wind turbine position or rotor yaw also need to be considered. Kheirabadi et al. [57] developed a wind farm model that includes a dynamic wake model, based on the researches of Shapiro et al [87, 86]. This model uses partial differential equations to capture wake transport. This model is one of the few that not only incorporates a dynamic wake model but also includes the dynamics of floating platforms, making it highly valuable for reference. In the model validation section, the study used FAST to validate the dynamics of the floating platform and employed experimental data from Bastankhah et al. [10] to quantitatively validate the steady-state transport behaviors of the wake. The results from both aspects indicate that the model possesses a certain level of accuracy. Naturally, the validation of wake dynamics in this wind farm model is supposed to be done. However, since existing high-precision CFD wind farm models are limited to bottom-fixed turbines, the assessment of wake transport dynamics in this study remains at an intuitive level. In summary, the study focuses on coupling wake dynamics with floating platform dynamics, but lacks dynamic validation of the wake model.

Another approach is to extend the widely recognized steady-state parametric wake models to incorporate the dynamics of wake behavior. A representative example of this is the FLOw Redirection and Induction Dynamics (FLORIDyn) model [37, 12]. This model achieves dynamic simulation of the wake by creating Observation Points (OPs). Each OP contains information on wind field states and turbine states and follows the wind direction of the free stream velocity [12]. In its latest version, the model introduces the concept of Temporary Wind Farms (TWFs). The creation of TWFs enables the decoupling of wake propagation under heterogeneous and changing conditions from the wake shape descriptionThe FLORIDyn framework has shown, through a nine-turbine case study, significant reduction in computational costs compared to its predecessor [13]. The paper's notable achievement is the ability to decrease computational cost by one to two orders of magnitude, enhancing viability for real-time control in wind farms with a large number of turbines. Based on the characteristics of the FLORIDyn framework, it combines low computational costs with the accuracy of the FLORIS model, offering an efficient and reliable solution for this project.

Besides using numerical or analytical methods to model wakes, with the rapid development of machine learning, some studies have also begun to use neural networks to characterize unsteady wake behaviors [93, 103, 64]. Ti et al. selected inflow wind speed and turbulence intensity as input variables for the neural network, and wind speed deficit and added turbulence kinetic energy as output variables [93]. The training data for the neural network came from a reduced-order turbine model based on the actuator disk model with rotation incorporating with Reynolds-averaged Navier-Stokes equations. The results showed that the neural network's predictions were in good agreement with numerical simulations and measurement data. The study conducted a lateral comparison with analytical models such as Jensen's model, and the results showed that the neural network's predictions were superior to Jensen's model. However, the study did not compare the neural network with more accurate and widely recognized models, such as FLORIS, in terms of performance. Therefore, it cannot be concluded that the neural network is definitively superior to analytical models. Additionally, the model in this study did not have the capability to predict dynamic wakes.

To include the dynamic wake, Zhang et al. used the proper orthogonal decomposition technique to reduce the dimensionality of the flow field and trained a long short-term memory neural network [103]. Their study shows that their wind farm model with dynamic wake

exhibits an overall prediction error of 4.8% with respect to the freestream and a short computation time. However, no comparison with an analytical wake model was implemented. Li believed that the dimensionality reduction in Zhang's model eliminated the spatial correlations, which led to a decrease in the model's prediction accuracy and would limit its long-term forecasting ability [64]. Consequently, Li et al. used a Bilateral Convolutional Neural Network to implement a machine learning-based dynamic wind farm model that does not require dimensionality reduction of the wind farm model. The study showed that this model highly aligns with high-fidelity simulation results, reducing the overall error to 3.7%. The use of neural networks for wake modeling indeed shows promising potential in current research.

1-4 Wake Mitigation Strategies

Up to now, three strategies of wake effect reduction have been widely researched and discussed: power de-rating, yaw-based wake redirection, and turbine repositioning. From the perspective of wind farms, these strategies provide different degrees of freedom for optimizing the efficiency of the wind farm. This section will elaborate on the basic ideas, current research status, and future research prospects of these three strategies.

1-4-1 Power De-rating

Power de-rating is also referred to as axial induction-based control [55]. This method involves adjusting the axial induction factors a, which in turn alters the thrust coefficient C_T and the power coefficient C_P for each turbine. As a result, it allows for the precise control of the rotor thrust forces and the turbines' power outputs, respectively. Typically, the C_P curve is relatively flat near its optimal blade pitch angle and TSR operating points, while the corresponding C_T curve is more sensitive to minor deviations in blade pitch angle or TSR [4]. Thus, a slight reduction in the power outputs of the upstream wind turbine can result in a significant decrease in thrust force, leading to a faster recovery of wind speed behind the rotor, which means a shorter wake, subsequently improving the power outputs of the downstream wind turbine. When the increase in output from the downstream wind turbine outweighs the sacrifice in output from the upstream turbine, the efficiency of the wind farm improves. For a clearer understanding of how adjusting axial induction factors could in theory facilitate wake mitigation, Figure 1-2 is provided: for $\hat{P}_0 < P_0$ and $\hat{P}_1 > P_1$, it is desired that $\hat{P}_0 + \hat{P}_1 > P_0 + P_1$.

(a) T0 under greedy operation **(b)** T0 de-rated

Figure 1-2: Illustration of Power De-rating in Wake Mitigation

The concept of axial-induction-based control has been widely researched since it was introduced by M. Steinbuch in 1988 [88]. Initially, this strategy was studied using engineering models of wake, and varying degrees of farm efficiency gains were observed. Horvat et al. [44] studied a series of eight wind turbines in tandem, modeling the wake using wind deficit, and observed a 2.85% increase in power generation. Similarly, Johnson and Fritsch et al. [50] conducted research on a series of three wind turbines in tandem, using the park wake model [53]. The optimized axial induction factors were identified using Extremum Seeking Control. In addition to achieving a 3.8% wind farm efficiency gain under low turbulence, the study also observed that the use of axial induction-based control can be counterproductive when the turbulence intensity is high. Moreover, studies indicate that the smaller the spacing between turbines, the more pronounced the effectiveness of axial induction control [100].

Furthermore, researchers have utilized high-fidelity wake models to determine the optimal configurations of axial induction factors. Among these, the study by Annoni et al. employed both the low-fidelity model FLORIS and the high-fidelity model SOWFA and drew comparisons between their performances [4]. In a two-turbine setup, both FLORIS and SOWFA indicated wind farm efficiency improvements after optimizing the axial induction factors. However, in a configuration with five turbines in series, the FLORIS model predicted an overall efficiency increase, while SOWFA indicated a decrease in overall efficiency. This discrepancy arose because FLORIS overestimated the wind speed recovery rate, resulting in the downstream turbines producing more power than in a more realistic scenario. To bridge this discrepancy, the study adjusted the wake expansion and recovery rate in FLORIS to accurately match the high-fidelity SOWFA model.

Lastly, several experiments and field tests targeting axial-induction-based control have been conducted. The experiment by J. Bartl et al. [9] indicated that no overall increase in power output was observed, no matter which method—changing the blade pitch or adjusting the TSR—was used to influence the axial induction factor. One explanation provided in the study is that the increased kinetic energy of the wake, resulting from the power reduction of the upstream turbine, largely diffused into the surrounding free stream flow, preventing any significant enhancement in the power output of the downstream turbine. Van der Hoek et al.'s 2019 field test reported positive results [98]. This field test was conducted on sixteen wind turbines arranged in three rows, with the first two rows each consisting of five turbines in series. For the five turbines in series in the first row, simulations indicated that adjusting the axial induction factor could lead to a 5.6% improvement in wind farm efficiency. Although the actual field test measured gain was smaller, it was still positive at 3.3%.

Due to variations in experimental setups, such as turbine size, inter-turbine spacing, and ambient wind conditions, different experiments yield diverse results that cannot be quantitatively or qualitatively generalized. However, one conclusion we can draw is that efficiency improvements predicted by low-fidelity wind farm models do not necessarily translate to increased output in actual tests. Nevertheless, since adjusting axial induction factors can influence the overall output of a wind farm and optimize the fatigue load distribution across turbines, the axial induction factor can be considered as a degree of freedom in wind farm optimization parameters.

1-4-2 Yaw-based Wake Redirection

In modern utility-scale wind turbines, a yaw motor is nearly always included to meet the requirement of aligning the rotor with the wind direction [77]. From the perspective of individual wind turbines, alignment with real-time wind direction is beneficial. However, from the viewpoint of wind farms and the wake effect, this might not be necessary. When the wind direction aligns with a turbine array, applying a yaw misalignment to the upstream turbines can steer their wakes away from the downstream turbines, as shown in Figure 1-3. This can increase the wind speed encountered by the downstream turbine, enhancing the overall efficiency of the farm. It's important to note that applying a yaw misalignment to a turbine will certainly reduce its individual output. Nonetheless, a moderately sized misaligning angle can still contribute to the overall output of the wind farm.

Figure 1-3: Illustration of Yaw-based Wake Redirection in Wake Mitigation

Van Dijk et al.'s research using the control-oriented low fidelity wake model FLORIS demonstrated that yaw redirection can enhance wind farm efficiency by 2.8% [99]. Additionally, the study also explored multi-objective wind farm optimization. Due to the redirected wake only partially overlapping with the rotor of the downstream turbine, asymmetric mechanical loads will be imposed on the downstream turbine. When considering both the objectives of increasing wind farm efficiency and reducing mechanical loads, Van Dijk's research showed that while ensuring a significant reduction in mechanical loads, wind farm efficiency can still achieve an improvement of 2.5%. Moreover, high-fidelity wake models based on CFD (Computational Fluid Dynamics) were used to validate the results from the low-fidelity wake model research. The results indicated that the power generation still showed an increasing trend [30, 35]. Furthermore, wind tunnel experiments and field tests on this topic also demonstrated its potential beneficial impact on enhancing wind farm efficiency [1, 11, 75, 45]. Adaramola et al. conducted research on yaw misalignment for two scaled tandem wind turbines in the large low-speed, closed-return wind tunnel of the Department of Energy and Process Engineering at Norwegian University of Science and Technology [1]. The results indicated that yawing the upstream turbine can increase the combined power output of the two turbines by 12%. Howland et al. conducted a full-scale field experiment in a wind farm in Alberta, Canada, with six utility-scale wind turbines arranged in a row [45]. The observed power generation growth rate, ranging between 7% and 13%, further corroborated the effectiveness of this strategy.

Besides, current research often involves combining axial-induction-based control with yaw-based wake redirection to optimize wind farm efficiency [5, 24]. These studies all indicate that the optimal values for axial induction factors are close to 1/3 and their contribution to improving wind farm efficiency is not significant. On the other hand, yaw angles emerge as the dominant optimization variable.

1-4-3 Turbine Repositioning

Unlike the first two wake effect mitigation strategies, turbine repositioning is only applicable to offshore floating wind farms. The fundamental principle of this strategy is to use existing or additional actuators to move the floating turbines a certain distance in the crosswind direction, as shown in Figure 1-4. This reduces the shadowing of the downstream turbines by the wake of the upstream turbines, thereby enhancing the power output of the wind farm.

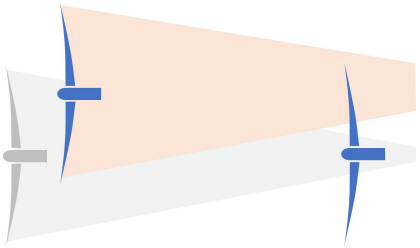

Figure 1-4: Illustration of Turbine Repositioning in Wake Mitigation

How to create a displacement of the wind turbine in the crosswind direction is a major focus of this strategy. Current research has branched into two areas: active repositioning, which involves adding additional actuators, and passive repositioning, which relies on utilizing aerodynamic forces for repositioning [55]. For active repositioning, popular methods include attaching a thruster and adjusting the mooring line length. Xu et al. conducted research on the additional attachment of thrusters, naming this approach the Dynamic Positioning System (DPS) [101]. The study indicates that in the absence of waves, approximately 50% of the electricity harvested by the wind turbine will be used for repositioning. When waves are present, this figure rises to 80%. Although there are no studies currently on using DPS for wind turbine repositioning to optimize wind farm efficiency, given the power consumption of this repositioning device, it is evident that it is not a very appealing option. On the other hand, the method of changing the mooring line length is also referred to as position mooring, which is typically implemented by a winch mechanism [21, 59, 81]. Studies on wind farm optimization using position mooring have all indicated that wind farm efficiency can be improved. However, there is currently no research on the energy consumption of the winch mechanism, so whether this approach can actually bring benefits remains to be studied. Furthermore, the variable length attribute introduces more non-linearity and new time-variability to the already non-linear mooring line, posing new challenges for wind turbine modelling.

In the context of passive repositioning, it predominantly denotes the utilization of aerodynamic forces for the repositioning of floating wind turbines. Intriguingly, while some papers categorize this as a “passive” solution, it fundamentally implies the omission of supplementary actuators for turbine repositioning. Nevertheless, this approach still leverages actuators that are already present in contemporary utility-scale turbines, such as nacelle yawing or blade pitching, to execute the repositioning. In the following section, this second research direction will be further elaborated upon. Current research on passive turbine repositioning has branched into roughly two directions. One focuses on controlling the dynamics of floating wind turbines at the turbine level, including both stabilizing and repositioning [33, 28, 42, 47]. This research direction is usually driven by a higher-level wind farm controller that provides

target positions and target power to accomplish repositioning and power regulation tasks. The other direction tends to simplify or sometimes even ignore the dynamics of floating wind turbines and emphasizes optimization control from the perspective of wind farm optimization. When the dynamics inherent to the floating wind turbine are entirely disregarded, this line of research emphasizes the optimization of the floating wind farm under steady-state conditions [56]. The optimization results can be fed as repositioning targets to the turbine controller in the first research direction we previously mentioned. When the dynamics of the floating wind turbine are incorporated into the floating wind farm optimization framework [58], the optimization results no longer require an additional turbine controller. Instead, they can be directly applied to the actuators of each turbine in the wind farm. In Section 1-5-2, this second research direction will be further elaborated upon.

Additionally, an interesting phenomenon based on rotor yaw misalignment for turbine repositioning is observed [66]: due to that altering the rotor yaw angle not only changes the turbine's position in the crosswind direction but also redirects the shape of its wake, the simultaneous existence of these two strategies, which are individually beneficial for wake mitigation, may counteract each other's effects. For instance, when a turbine employs rotor yaw misalignment to move in the +y direction, this misalignment induces a wake deflection in the -y direction, counteracting the benefits of its movement towards the +y direction. Therefore, controlling floating turbines to mitigate the counteracting effects between these two strategies presents a potential research direction.

1-5 Floating Offshore Wind Farm Control

In the previous section, three mainstream efficiency optimization strategies for floating offshore wind farms and their current research status were briefly introduced. As a result, the following three possible control degrees of freedom for wind farm optimization are obtained: axial induction factor, rotor yaw angle and turbine position. It is worth noting here that if the repositioning of the turbine is indirectly achieved by changing the axial induction factor or the rotor yaw, the actual control degrees of freedom, in this case, are only two, i.e., axial induction factor and rotor yaw angle [81, 58, 54]. If the repositioning of the turbine is accomplished by an additional actuator, then the turbine position can be used alone as a degree of freedom for steady-state wind farm control [56]. However, if dynamic optimal control of the wind field is involved and additional actuators are used for repositioning, the turbine position as a state can no longer be used as a control degree of freedom for the optimization of the wind farm, and instead a new degree of freedom may be the thruster's thrust force or the length of the variable mooring line. It can be seen that optimization methodologies for wind farms will diverge in two different directions with the need for steady-state or dynamic optimization.

1-5-1 Steady-State Floating Offshore Wind Farm Control

Many current studies focus on the optimization of efficiency during the steady state of floating offshore wind farms. This research direction first uses steady-state wind turbine models and steady-state wake models to establish a steady-state floating offshore wind farm model. Next, under the assumption that a predominant wind profile exists, certain optimization

algorithms are used to derive the optimal targets for each turbine under that wind profile [81, 56, 54]. The optimal targets mentioned here typically include optimal position, optimal axial induction factor, optimal rotor yaw angle, and optimal power. The optimization of this research direction is limited to steady-state performance, so when the postures and positions of the various floating turbines are not at these optimal targets, a secondary controller is needed to satisfy the steering of the turbines to the optimal position and track the optimal power [33, 28, 42, 47]. Furthermore, steady-state optimization for floating offshore wind farms, although different in name from that for bottom-fixed wind farms, shares some foundational methodologies. Research in this area can progress by integrating strategies used for optimizing layouts in bottom-fixed wind farms [83, 85] with those for adjusting induction factors and/or yaw angles [5, 24]. This approach merges two distinct areas of study, as the transient process of floater movement is not considered in the optimization problem.

In the study conducted by Kheirabadi et al.[56], a framework was established to identify optimal targets for each floating wind turbine. The research further examined how initial layout parameters of the wind farm—such as mooring line length, mooring system orientation, and turbine spacing—affect the efficiency of the optimized wind farm and the mobility of the turbines. For example, observations such as a longer mooring line length can improve the efficiency of the optimized wind farm, and the mooring system orientation should not exceed 20 degrees, otherwise, the efficiency of the wind farm will drastically decrease. This indicates that for the steady-state efficiency optimization of floating wind farms, the optimization process involves more than just the turbine's own degrees of freedom, like the axial induction factor and yaw angle. Various initial layout parameters of the wind farm, including mooring line length, mooring system orientation, turbine spacing, and the neutral position of the floater [54], also play a significant role in affecting the steady-state power production of the floating wind farm. Alkarem et al. [3] proposed the Turbine Repositioning Technique for Layout Economics (TRTLE) method for optimizing floating wind farms based on wind farm layout parameters. Instead of using rotor yaw misalignment to achieve turbine repositioning, this study achieves the movement of turbines in different directions within a wind farm solely by using different mooring system orientations. The TRTLE method achieves up to a 30% reduction in wake losses, increasing energy production, and offers cost-effective, reliable layout flexibility without the need for active controls. The absence of active controls benefits actuator loads and the overall lifespan of the turbine system. However, its limitation is that this optimization approach is only applicable before the deployment phase of the turbines.

The current research on this optimization strategy should pay attention to the following points. First is the connection issue between the farm level controller and the turbine level controller. In current research, the steady-state farm controller and the turbine dynamic repositioning controller are studied separately, and there is no research that connects the two altogether. For example, the wind farm controller often provides a target axial induction factor, while the turbine repositioning controller often assumes a given target blade pitch angle and target generator torque, which means that the connection between the two levels of controllers needs to involve the translation of the axial induction factor to the blade pitch angle and generator torque. Second is the optimality of this strategy. Since the optimization of this strategy is limited to steady-state power optimization and does not involve the transient process during turbine repositioning, the overall wind farm control can improve the efficiency of the wind field but is still only suboptimal. This also inspires dynamic control of floating wind farms, which will be detailed in the next section. Lastly, there is the question of whether

it has the capability to handle time-varying wind profiles. If the change in the wind condition is not fast, the secondary repositioning controller's response can keep up with the changes in the wind farm controller targets, then this steady-state-based optimization strategy is feasible. But if the wind profile is constantly changing, which is indeed the case in reality, then a real-time dynamic control of the floating wind field would be expected.

1-5-2 Real-Time Dynamic Floating Offshore Wind Farm Control

The conceptual difference from the previous floating wind farm optimization strategy is that, in the methodology described in this section, the dynamic performance within a wind farm will now be included in the optimization problem. Therefore, the research on this strategy must be based on a floating wind farm model that includes all the main dynamics. Given the inclusion of dynamics, the optimization problem will be based on the behavior of the floating wind farm over a period of time. Consequently, the optimization algorithm will provide control signals for each control degree of freedom for each floating wind turbine at every time step within this period, effectively generating an optimal control sequence, as shown in Figure 1-5.

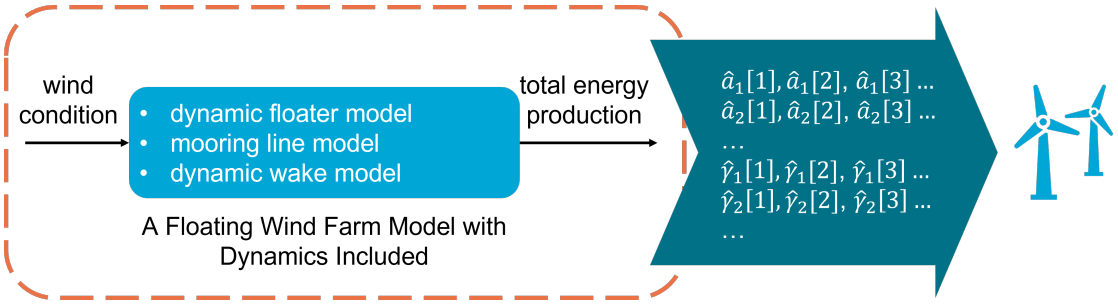

Figure 1-5: Illustration of Real-Time Dynamic Floating Offshore Wind Farm Control

Unlike steady-state wind farm optimization, dynamic wind farm optimization, due to the inclusion of a dynamic model for the floating wind turbines, obviates the need for a secondary turbine repositioning controller. Assuming that the actual wind profile matches the wind profile known to the optimizer, the optimal control sequence determined by the optimizer can be directly applied to each floating wind turbine in the wind farm at every time step to achieve maximized energy production during this period.

Given the inherent variability of wind conditions, it is impractical for a dynamic wind farm efficiency optimizer to obtain or predict wind profiles in real time for the foreseeable future. Under such circumstances, Model Predictive Control (MPC) can be employed. When wind conditions fluctuate, this dynamic wind farm efficiency optimizer can be seamlessly incorporated into an economic model predictive control framework as the optimization module, enabling real-time optimal control of the floating wind farm. As we discussed in Section 1-3-2, the dynamic models for control-oriented floating wind farms are still at an embryonic stage, with only a handful of studies undertaken to develop them [57, 76]. Consequently, research on real-time optimization and control using these control-oriented dynamic models for floating wind farms is also very limited. Kheirabadi et al. [58] were the first to apply economic Model Predictive Control to the real-time optimization and control of floating wind farms. The controller is based on their team's previously proposed dynamic wind farm model [57],

which notably utilizes neural networks to simulate the dynamics of floating wind turbines. The simulated environment for this study was a fluctuating wind profile resembling a sinusoidal function. The study conducted a comprehensive analysis of the behavior of individual turbines under the controller's influence in downwind and crosswind orientations, which is consistent with the theoretical expectations of their movement dynamics. The results indicated a 20.2% increase in power generation compared to greedy control, laying a foundation for wind farm optimization strategies and eliciting a positive response.

1-6 Problem Statement

This research addresses the problem of maximizing the energy production of a floating wind farm by investigating and optimizing the combination of multiple wake mitigation strategies. Specifically, this study focuses on two primary strategies:

1. **Wake Steering**: This is achieved by altering the rotor yaw angle, redirecting the turbine wake away from downstream turbines.
2. **Turbine Repositioning**: This can be achieved by altering the rotor yaw angle or by adjusting both the axial induction factor and the rotor yaw angle.

The objective of this research is to determine the optimal control sequences for rotor yaw angles that maximize the energy production of the floating wind farm over a specified period of time. To achieve this, a dynamic model of a floating wind farm is first developed. This model simulates the interactions and dependencies between turbines under different control inputs. Subsequently, optimization algorithms are employed to find the optimized control sequences for the rotor yaw angles. Finally, a thorough analysis is conducted on the impact of the optimized control sequences.

1-7 Outline

The outline of this thesis is structured as follows: In **Chapter 2**, a dynamic floating wind farm model is developed. First, the floater dynamics are modeled. By integrating the developed floater model with a dynamic wake model, the dynamic floating wind farm model used in this study is constructed. The functionality of this model is then demonstrated. In **Chapter 3**, optimization of the floating wind farm aiming for maximum energy production is performed. The optimization results indicate that there are two optimal operating modes for floating wind farms: static repositioning and dynamic repositioning. Qualitative explanations of these two operating modes are provided in this chapter. Moving to **Chapter 4**, a comprehensive analysis of these two working modes is provided, aiming to provide quantitative explanations. In **Chapter 5**, the conclusions of this study are presented. Additionally, the limitations of this research are discussed, along with suggestions for future research directions and prospects.

Chapter 2

Modelling of Floating Wind Farms

In this chapter, a dynamical floating wind farm model is developed, which serves as a basis for optimization and control research. In Section 2-1, the dynamics of the floater will be first described. To represent the interactions between turbines, this research utilizes the dynamical wake model FLORIDyn [12]. Therefore, a brief explanation of the working principle of FLORIDyn is provided in Section 2-2. Additionally, the modelling of the floating wind farm is achieved by incorporating the dynamics of the floater into FLORIDyn. The setup and layout of a two-turbine floating wind farm are detailed in Section 2-3. Finally, the capabilities of the developed floating wind farm model are demonstrated through case studies in Section 2-4.

2-1 Modelling of the Floater

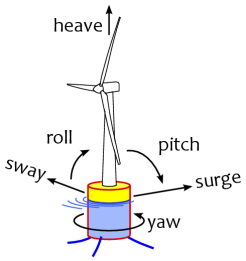

Figure 2-1: The floater and mooring lines introduce six additional degrees of freedom to the system: platform surge, sway, heave, roll, pitch, and yaw. Figure credit: [41].

For a floating wind turbine, the floater and the mooring lines introduce six additional degrees of freedom to the system: platform surge, sway, heave, roll, pitch, and yaw. These are illustrated in Figure 2-1. For different control problems, these six new degrees of freedom are either fully or partially incorporated into the modeling of the floating wind turbine [89]. For current research focused on turbine stabilization control or small-range repositioning control (of a magnitude of 0.1 rotor diameter), all six degrees of freedom are considered in their models, as detailed in [43, 42, 28]. In contrast, for strategies aimed at enhancing wind farm

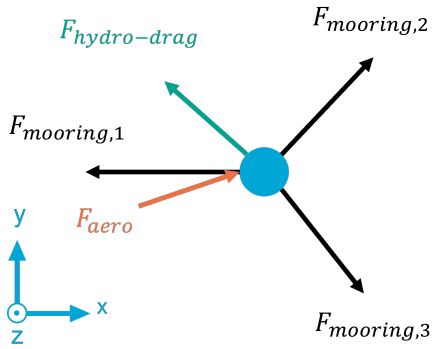

Figure 2-2: Illustration of the three main types of forces acting on a floating wind turbine: mooring line force, hydrodynamic drag force, and aerodynamic thrust force.

energy production through relatively large-range repositioning control (with a movable range normally exceeding at least half of the rotor diameter), only the platform surge and sway are taken into consideration, as detailed in [58, 33, 57]. Given that the focus of this study aligns more closely with the second type of research mentioned above, a 2D planar floating turbine model on the X-Y plane is developed. Here, the X-Y plane is defined to be coplanar with the water surface; consequently, the positive direction of the Z-axis points from the water surface towards the sky.

The floating wind turbine selected for this study is the 5MW semi-submersible floating turbine developed by the National Renewable Energy Laboratory (NREL) [51, 80]. It has a rotor diameter D of 126 meters and a total system weight m_{turbine} of 1.3473×10^7 kg (including ballast).

The states of the floater model are defined as

$$\mathbf{x} = [x_1\, x_2\, x_3\, x_4]^T = [p_x\, p_y\, v_x\, v_y]^T$$

where p_x and p_y represent the center position of the floating wind turbine in the x and y directions, and v_y and v_y represent its velocity in the x and y directions. Focusing on the motion of the floating wind turbine in the X-Y two-dimensional plane, it is primarily influenced by three types of forces: the mooring line force, the hydrodynamic drag force, and the aerodynamic thrust force, as shown in Figure 2-2. According to Newton's second law, the dynamics of the system can be expressed as:

$$m_{\text{turbine}} \begin{bmatrix} \dot{x}_3 \\ \dot{x}_4 \end{bmatrix} = \mathbf{F}_{\text{mooring}} - \mathbf{F}_{\text{hydro}} + \mathbf{F}_{\text{aero}} \tag{2-1}$$

where the bolded $\mathbf{F}$ represents a 2×1 force vector, with the first element representing the component in the x-direction and the second element representing the component in the y-direction. Furthermore, the dynamics of the floater can be formulated into the following state-space form:

$$\begin{bmatrix} \dot{x}_1 \\ \dot{x}_2 \\ \dot{x}_3 \\ \dot{x}_4 \end{bmatrix} = \begin{bmatrix} x_3 \\ x_4 \\ \frac{1}{m_{\text{turbine}}+m_{\text{added}}} \left(\mathbf{F}_{\text{mooring}}(x_1, x_2) - \mathbf{F}_{\text{hydro}}(x_3, x_4) + \mathbf{F}_{\text{aero}}(x_3, x_4, \mathbf{U}_{\text{eff}}, \gamma, a)\right) \end{bmatrix} \tag{2-2}$$

where $\mathbf{U}_{\text{eff}} = [U_{\text{eff},x}, U_{\text{eff},y}]^T$ is the instant effective wind speed, γ is the rotor yaw angle and a is the axial induction factor. The added mass m_{added} comes from the hydrodynamic load. Its specific composition will be addressed in the subsequent calculation of the hydrodynamic drag force $\mathbf{F}_{\text{hydro}}$.

The specific calculations of these three forces are as follows:

Mooring line force $\mathbf{F}_{\text{mooring}}(p_x, p_y)$: The force exerted on the floating wind turbine by the mooring system in the X-Y plane is the resultant force arising from the horizontal tensions of the three mooring lines, given by:

$$\mathbf{F}_{\text{mooring}}(p_x, p_y) = \sum_{i=1}^{3} \mathbf{F}_{\text{mooring,i}}(p_x, p_y)$$

The force from the ith mooring line in the X-Y plane, $\mathbf{F}_{\text{mooring,i}}(p_x, p_y)$, is calculated as follows:

$$\mathbf{F}_{\text{mooring,i}}(p_x, p_y) = F_{\text{HT}}(d_i(p_x, p_y)) \frac{\mathbf{p}_{\text{anchor,i}} - \mathbf{p}_{\text{fairlead,i}}(p_x, p_y)}{d_i(p_x, p_y)} \tag{2-3}$$

Here, $\mathbf{p}_{\text{anchor,i}}$ is the constant position vector of the ith anchor, $\mathbf{p}_{\text{fairlead,i}}(p_x, p_y)$ is the position vector of the ith fairlead, $d_i(p_x, p_y) = ||\mathbf{p}_{\text{anchor,i}} - \mathbf{p}_{\text{fairlead,i}}(p_x, p_y)||$ is the horizontal distance between the ith fairlead and its corresponding anchor, as illustrated in Figure 2-3. For the sake of simplicity, $d_i(p_x, p_y)$ will be referred to as the horizontal anchor-fairlead distance in the following text. Besides, $F_{\text{HT}}(d_i(p_x, p_y))$ is the horizontal tension provided by mooring line i.

The position of the ith fairlead $\mathbf{p}_{\text{fairlead,i}}(p_x, p_y)$ is calculated specifically by the following equations:

$$\begin{aligned}
\mathbf{p}_{\text{fairlead,1}}(p_x, p_y) &= [p_x, p_y]^T + \left[-\tfrac{1}{2} d_{\text{fairlead}} \cos\tfrac{\pi}{6}, 0\right]^T \\
\mathbf{p}_{\text{fairlead,2}}(p_x, p_y) &= [p_x, p_y]^T + \left[\tfrac{1}{2} d_{\text{fairlead}} \tan\tfrac{\pi}{6}, \tfrac{1}{2} d_{\text{fairlead}}\right]^T \\
\mathbf{p}_{\text{fairlead,3}}(p_x, p_y) &= [p_x, p_y]^T + \left[\tfrac{1}{2} d_{\text{fairlead}} \tan\tfrac{\pi}{6}, -\tfrac{1}{2} d_{\text{fairlead}}\right]^T
\end{aligned}$$

where d_{fairlead} is the distance between every fairlead, as annotated in Figure 2-3a.

Using the calculated distance $d_i(p_x, p_y)$, the horizontal tension $F_{\text{HT}}(d_i(p_x, p_y))$ provided by mooring line i can be obtained according to the lookup table provided by NREL [80], visually illustrated in Figure 2-4. The data from this lookup table were derived numerically using FAST for the scenario of an unstretched mooring line length of 835.5 meters and a vertical anchor-fairlead distance of 186 meters. The use of a lookup table in this study is intended to reduce computational cost.

Hydrodynamic drag force $\mathbf{F}_{\text{hydro}}(v_x, v_y)$ and the added mass m_{added}: To incorporate the impact of water on the dynamics of the floating wind turbine, the Morison equation is used. When a floating turbine moves in an oscillatory flow, the Morison equation suggests that the hydrodynamic loads can be calculated as follows [90, 57]:

$$\begin{aligned}
\mathbf{F}_{\text{hydro}}(\mathbf{v}, \dot{\mathbf{v}}, \mathbf{U}, \dot{\mathbf{U}}) = & \underbrace{\frac{1}{2}\rho \sum_{i \in \mathcal{D}} (C_{d,i} A_{d,i})(\mathbf{U} - \mathbf{v})||\mathbf{U} - \mathbf{v}||}_{\text{Drag force}} + \underbrace{\rho \sum_{i \in \mathcal{D}} (C_{a,i} A_{a,i})(\dot{\mathbf{U}} - \dot{\mathbf{v}})}_{\text{Hydrodynamic mass force}} \\
& + \underbrace{\rho V \dot{\mathbf{U}}}_{\text{Froude-Krylov force}}
\end{aligned} \tag{2-4}$$

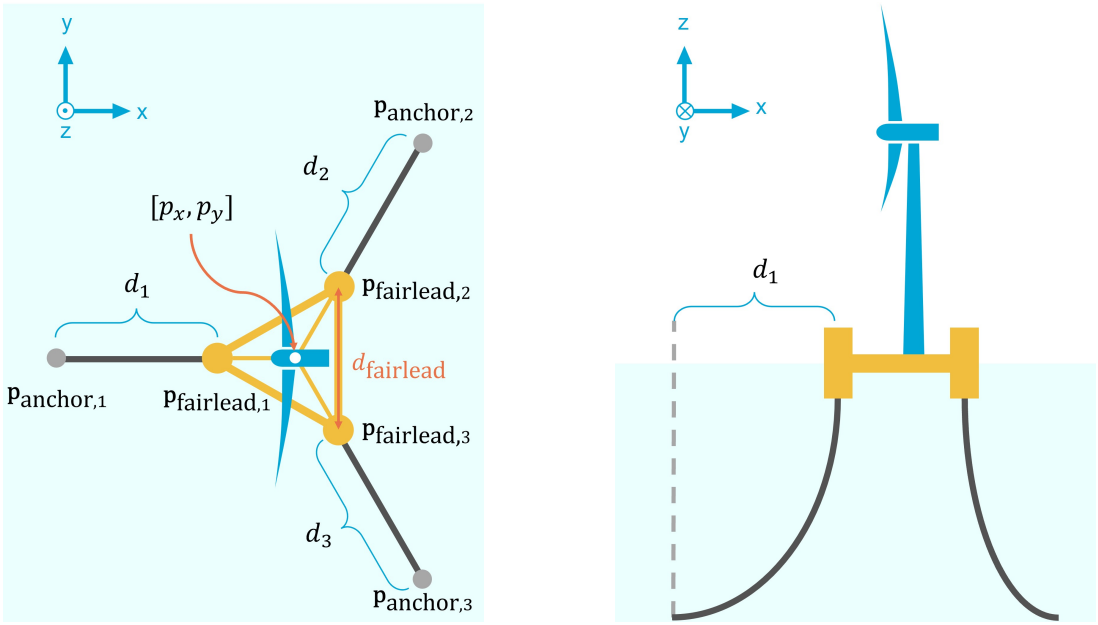

(a) top view (X-Y plane) **(b)** side view (X-Z plane)

Figure 2-3: Illustration of the anchors, fairleads, and horizontal anchor-fairlead distances. Note that this figure is for illustrative purposes only; the proportions of the mooring line lengths and turbine dimensions are intentionally distorted.

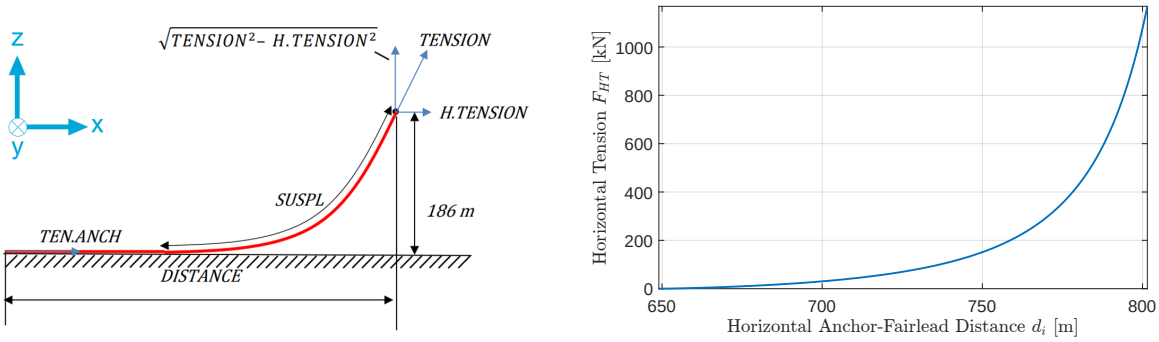

(a) Force analysis on a single mooring line **(b)** Horizontal tension by one mooring line

Figure 2-4: (a) The free body diagram of a single mooring line is shown [80]. (b) The horizontal tension F_{HT} (the *H.TENSION* in (a)) resulting from different horizontal anchor-fairlead distances for a mooring line of fixed length is plotted.

where ρ is the density of the flow, $C_{d,i}$ and $A_{d,i}$ are the drag coefficient and reference area of the submerged component i, $\mathbf{U}$ is the velocity vector of the flow, $\mathbf{v} = [v_x, v_y]^T$ is the velocity vector of the turbine, $C_{a,i}$ and $A_{a,i}$ are the added mass coefficient and reference area of the submerged component i, and V is the cylinder volume per unit cylinder length. Here, $\mathcal{D}$ denotes the set including all the submerged components of this turbine.

Here, we assume still water conditions, i.e., the velocity vector $\mathbf{U}$ and its time derivative $\dot{\mathbf{U}}$ are both zero. Consequently, the hydrodynamic load on the turbine can be expressed as:

$$\mathbf{F}_{\text{hydro}}(\mathbf{v}, \dot{\mathbf{v}}) = \underbrace{\frac{1}{2}\rho \sum_{i\in\mathcal{D}} (C_{d,i}A_{d,i})\mathbf{v}||\mathbf{v}||}_{\text{Drag force}} - \underbrace{\rho \sum_{i\in\mathcal{D}} (C_{a,i}A_{a,i})\dot{\mathbf{v}}}_{\text{Hydrodynamic mass force}} \tag{2-5}$$

Since the hydrodynamic mass force term contains the first derivative of the velocity states, $\dot{\mathbf{v}} = [\dot{x}_3, \dot{x}_4]^T$, we here define $m_{\text{added}} = \rho \sum_{i\in\mathcal{D}} (C_{a,i}A_{a,i})$. In this way, this term can be moved to the left side of the state-space equation and incorporated into m_{turbine} by summation. Meanwhile, the remaining drag force term is considered the hydrodynamic drag force acting on the floating wind turbine:

$$\mathbf{F}_{\text{hydro}}(v_x, v_y) = \frac{1}{2}\rho \sum_{i\in\mathcal{D}} (C_{d,i}A_{d,i})\mathbf{v}||\mathbf{v}|| \tag{2-6}$$

Aerodynamic thrust force $\mathbf{F}_{\text{aero}}(v_x, v_y, \mathbf{U}_{eff}, \gamma, a)$: Considering that the rotor may misalign with the wind direction, the modelling of the aerodynamic thrust force follows the vortex cylinder model of a yawed actuator disc [19]. The specific calculations are based on the work of Kheirabadi et al. [57], as follows:

$$\mathbf{F}_{\text{aero}}(v_x, v_y, \mathbf{U}_{eff}, \gamma, a) = \frac{1}{8} C_t(v_x, v_y, \mathbf{U}_{eff}, \gamma, a)\rho_a \pi D^2 \left\|\mathbf{V}_{\text{rel}}(v_x, v_y, \mathbf{U}_{eff})\right\|^2 \mathbf{n}(\gamma) \tag{2-7}$$

where ρ_a represents the density of the air, D is the diameter of the rotor plane, and $\mathbf{n}(\gamma) = [\cos\gamma, \sin\gamma]^T$ is the unit vector based on the rotor yaw angle at this moment. $\mathbf{V}_{\text{rel}}(v_x, v_y, \mathbf{U}_{\text{eff}})$ is the relative effective incoming wind speed:

$$\mathbf{V}_{\text{rel}}(v_x, v_y, \mathbf{U}_{\text{eff}}) = \mathbf{U}_{eff} - \mathbf{v} = \begin{bmatrix} U_{eff,x} - v_x \\ U_{eff,y} - v_y \end{bmatrix} \tag{2-8}$$

$C_t(v_x, v_y, \mathbf{U}_{\text{eff}}, \gamma, a)$ is the thrust coefficient, calculated as follows:

$$C_t(v_x, v_y, \mathbf{U}_{\text{eff}}, \gamma, a) = 4a\left(\cos\gamma_{\text{rel}} + \tan\frac{\chi}{2}\sin\gamma_{\text{rel}} - a\sec^2\frac{\chi}{2}\right) \tag{2-9}$$

Here, $\gamma_{\text{rel}} = \gamma - \tan^{-1}\left(\frac{U_{\text{eff},y} - v_y}{U_{\text{eff},x} - v_x}\right)$ is the relative rotor yaw angle, which takes into account the velocity of the turbine itself. And χ is the wake skew angle immediately past the rotor, calculated as $\chi = (0.6a + 1)\gamma_{\text{rel}}$.

2-2 Modelling of Floating Wind Farms

In order to model the dynamic behaviors of a floating wind farm, the wakes generated by the turbines must be incorporated to effectively capture their interactions. This section will first

briefly introduce the wake model FLORIDyn (FLOw Redirection and Induction Dynamics) used in this study, followed by an explanation of how the dynamics of floaters are integrated with the FLORIDyn wake model.

FLORIDyn is a wake model capable of characterizing dynamic wake behavior in response to changes in turbine states, such as rotor yaw angle and axial induction factor, as well as variations in wind conditions. [38, 13, 12]. FLORIDyn generates new Observation Points (OPs) at each simulation timestep to record the current turbine states. Meanwhile, existing OPs, which preserve the historical states of the turbines, propagate at the free stream velocity. This propagation of the existing OPs also includes deflection based on the current wind field, calculated using FLORIS [36]. The wind speed reduction experienced by each turbine is calculated based on the two OPs in each OP chain that are closest to the turbine. Using these two OPs, a temporary wind farm, referred to as TWF in [12], is established to compute the foreign reduction caused by the wake. Due to the chosen method of OP propagation and the TWF approach, this wake model accurately captures the dynamics of the wake while maintaining exceptional simulation speed, enabling real-time control of wind farm flow. For example, for an 1800-second simulation horizon, FLORIDyn requires only 0.2 seconds of simulation time on a laptop equipped with a 12th Gen Intel(R) Core(TM) i7-12700H processor.

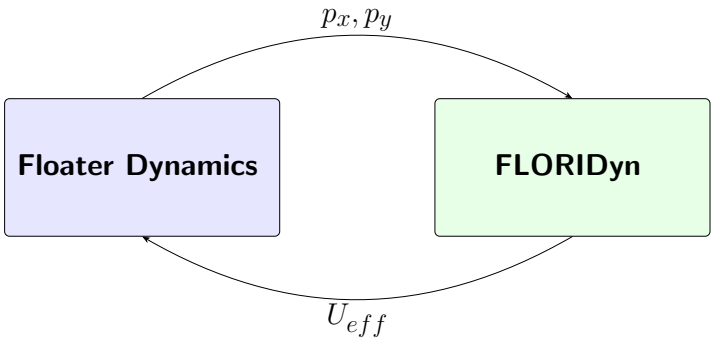

Figure 2-5: Diagram illustrating the connection between the floater's dynamics and the FLORIDyn model. The floater's dynamics provide position coordinates (p_x, p_y) to the FLORIDyn model for generation of the new OPs, while FLORIDyn computes the effective wind speed (U_{eff}) that influences the floater's dynamics.

By integrating the floater model described in Section 2-1 with the FLORIDyn wake model, we obtain the dynamic floating wind farm model required for this study. Figure 2-5 illustrates how these two components are interconnected. In each simulation timestep, the update of turbine positions and velocities relies on the effective wind speed U_{eff} experienced by the turbines, which is provided by FLORIDyn. Concurrently, the global positions of the new OPs in FLORIDyn are generated from the current positions of the floating turbines $[p_x, p_y]$. Additionally, the local positions of existing OPs in FLORIDyn are updated relative to the current positions of the turbines to ensure their global positions remain unchanged.

In Figure 2-6a, the transportation of the existing OPs (indicated by solid arrows) and the creation of a new OP are shown. By considering the current turbine states and wake deflection under the current wind conditions, the new positions of each OP at the end of step k are obtained. Here, $OP_{i,k-1}$ represents the position of the OP with index i at the end of step $k-1$ (depicted by hollow circles), and $OP_{i,k}$ represents the position of the OP with index

i at the end of step k (depicted by solid circles). Meanwhile, the turbine moves from its old position $[p_{x,k-1}, p_{y,k-1}]$ to its new position $[p_{x,k}, p_{y,k}]$, a process illustrated by the dashed arrow. Simultaneously, a new OP is created at the turbine's new position, labeled as index 5 in Figure 2-6a.

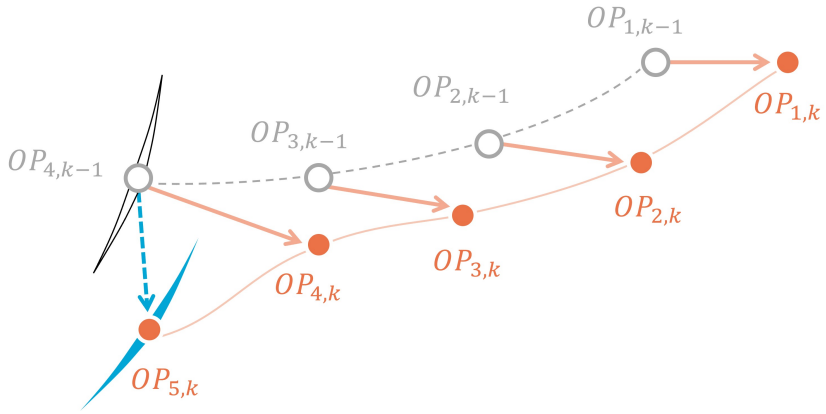

(a) Propagation of the Observation Points (OPs)

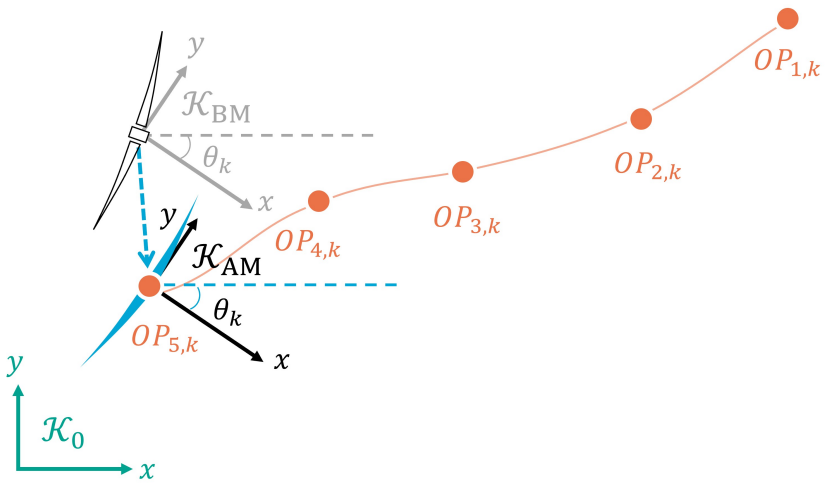

(b) Definition of the Local Coordinate Systems

Figure 2-6: (a) Illustration of the propagation of observation points (OPs). The hollow points represent the OPs in simulation step $k-1$, while the solid points represent the propagated OPs at the end of step k. Additionally, a new $OP_{5,k}$ is created at the end of step k, located at the new turbine position. (b) Definition of the local coordinate systems before and after the turbine moves, denoted by $\mathcal{K}_{BM}$ and $\mathcal{K}_{AM}$, respectively. "BM" stands for Before the Movement, and "AM" stands for After the Movement. $\mathcal{K}_0$ represents the global coordinate system, with its origin located at the turbine's neutral position.

In Figure 2-6b, three coordinate systems are defined: $\mathcal{K}_0$, $\mathcal{K}_{BM}$, and $\mathcal{K}_{AM}$, where "BM" stands for Before the Movement, and "AM" stands for After the Movement. $\mathcal{K}_0$ is the global coordinate system, with its origin located at the neutral position of the turbine. $\mathcal{K}_{AM}$ is the local coordinate system at the end of step k. Its origin is at the turbine's position at step k, $[p_{x,k}, p_{y,k}]$, and its x-direction is orthogonal to the rotor plane at step k. In terms of orientation, $\mathcal{K}_{AM}$ can be obtained by rotating $\mathcal{K}_0$ around its z-axis by $-\theta_k$. $\mathcal{K}_{BM}$ is the

local coordinate system based on the old turbine position $[p_{x,k-1}, p_{y,k-1}]$. $\mathcal{K}_{\text{BM}}$ has the same orientation as $\mathcal{K}_{\text{AM}}$.

After the simulation step k, the coordinates of every OP with respect to $\mathcal{K}_0$ and $\mathcal{K}_{\text{AM}}$ should be stored for later calculation. However, within the step k, after the existing OPs complete their transportation under FLORIDyn, their local coordinates are still with respect to $\mathcal{K}_{\text{BM}}$. Therefore, it is necessary to update their local coordinates to $\mathcal{K}_{\text{AM}}$ to ensure that the change in the origin of the local coordinate system does not alter the global coordinates of the existing OPs.

The coordinates for the existing OPs under $\mathcal{K}_{\text{AM}}$ are obtained using the following equation:

$$\begin{bmatrix} OP_{i,k,x} \\ OP_{i,k,y} \end{bmatrix}_{\mathcal{K}_{\text{AM}}} = \begin{bmatrix} OP_{i,k,x} \\ OP_{i,k,y} \end{bmatrix}_{\mathcal{K}_{\text{BM}}} + \begin{bmatrix} \cos\theta_k & -\sin\theta_k \\ \sin\theta_k & \cos\theta_k \end{bmatrix} \begin{bmatrix} p_{x,k} - p_{x,k-1} \\ p_{y,k} - p_{y,k-1} \end{bmatrix}_{\mathcal{K}_0} \tag{2-10}$$

where $[\cdot]_{\mathcal{K}_{(\cdot)}}$ specifies which coordinate system the coordinate inside of the brackets is with respect to.

The reason why $\mathcal{K}_{\text{BM}}$ and $\mathcal{K}_{\text{AM}}$ have the same orientation is as follows: here we define another coordinate system, $\mathcal{K}_{k-1}$, to represent the local coordinate system of the turbine at the end of step $k-1$, as shown in Figure 2-7. $\mathcal{K}_{k-1}$ shares the same origin as $\mathcal{K}_{\text{BM}}$, but has a different orientation. The x-axis of $\mathcal{K}_{k-1}$ is orthogonal to the rotor plane at the end of step $k-1$, and the orientation angle here is θ_{k-1}. Generally, under time-varying wind conditions or rotor yaw angle changes, $\theta_{k-1} \neq \theta_k$. This means that at each simulation step, the local coordinate system undergoes a translational change due to the turbine's repositioning, and a rotational change due to time-varying wind conditions or rotor yaw angle. The latter rotational transformation has already been accounted for by FLORIDyn, as the local coordinates of each OP have been updated from $\mathcal{K}_{k-1}$, oriented at θ_{k-1}, to $\mathcal{K}_{\text{BM}}$, oriented at θ_k. However, the former translational transformation needs to be considered in a floating wind farm. This is why it is necessary to update the local coordinates of the OPs from $\mathcal{K}_{\text{BM}}$ to $\mathcal{K}_{\text{AM}}$, and why $\mathcal{K}_{\text{BM}}$ and $\mathcal{K}_{\text{AM}}$ have the same orientation.

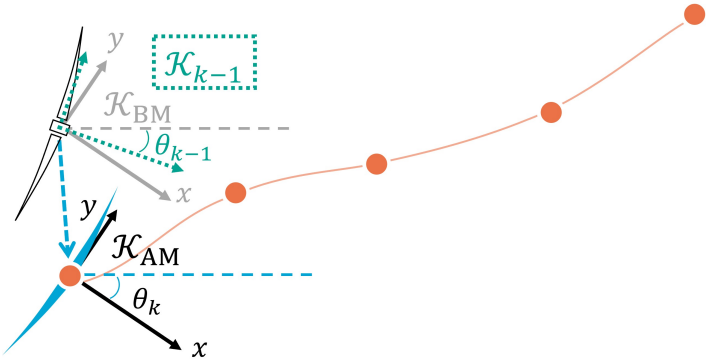

Figure 2-7: Three coordinate systems are illustrated here: $\mathcal{K}_{k-1}$, $\mathcal{K}_{\text{BM}}$, and $\mathcal{K}_{\text{AM}}$. The local coordinates update from $\mathcal{K}_{k-1}$ to $\mathcal{K}_{\text{BM}}$ is performed within the FLORIDyn framework. The further local coordinates update from $\mathcal{K}_{\text{BM}}$ to $\mathcal{K}_{\text{AM}}$ is done using (2-10), aiming to incorporate the information of the turbine position change.

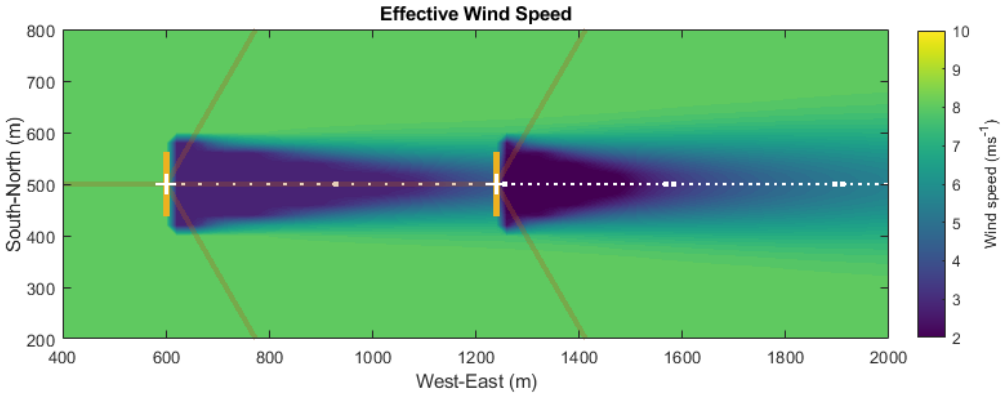

Figure 2-8: Schematic of the Two-Turbine Floating Wind Farm Setup

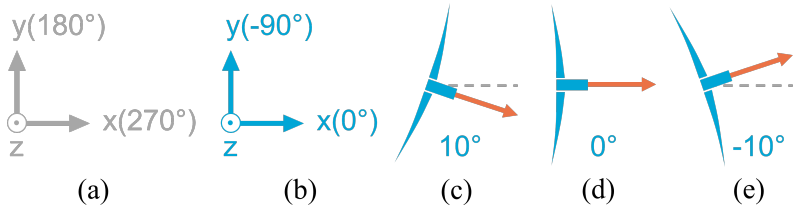

Figure 2-9: Definition of Wind Direction and Yaw Angle for the Study

2-3 Description of a Two-Turbine Floating Wind Farm Setup

This section introduces a two-turbine floating wind farm, as shown in Figure 2-8.

First, for clarity, the definitions of wind direction angle and rotor yaw angle are explained here. Conventionally, due east (the +x direction in Figure 2-8) is set as 270 degrees, and due north (the +y direction in Figure 2-8) as 180 degrees, as shown in Figure 2-9(a). However, since the angles involved in this study are all in the vicinity of 270 degrees, the definitions of angles in this research are uniformly subtracted by 270 degrees from the conventional definitions for simplicity, as shown in Figure 2-9(b). Additionally, the definition of the rotor yaw angle is the angle between the +x direction (0 degrees as just defined) and the normal vector to the rotor plane facing downwind. Illustrations can be found in Figure 2-9(c), (d), and (e).

The layout and relevant parameter settings for this two-turbine floating wind farm is explained as follows: under no-wind conditions, the upstream floating wind turbine is located at its neutral position [600, 500] m, and the downstream floating wind turbine is at its neutral position [1240, 500] m.

2-4 Demonstration of Model Capabilities

In this section, the functionalities of the constructed dynamic floating wind farm model will be demonstrated. This model can take varying axial induction factor and varying rotor yaw angle as control inputs. Additionally, wind direction as an environmental variable can also be

time-varying. Therefore, the following three cases will be presented: Varying Axial Induction Factor, Varying Rotor Yaw Angle, and Varying Wind Direction.

Case 1: Varying Axial Induction Factor The upstream turbine T_0 undergoes derating while the axial induction factor of the downstream turbine T_1 remains constant. The specific control sequences can be found in the left panel of Figure 2-10a. In this case, the wind direction remains constant at 0 degrees, and the rotor yaw angle of both turbines is also maintained at 0 degrees. The resulting power output trajectories and turbine movement trajectories can be found in the remaining panels of Figure 2-10. In Figure 2-13a, a snapshot of the floating wind farm at $t = 1000$ s is presented to provide a clearer visualization.

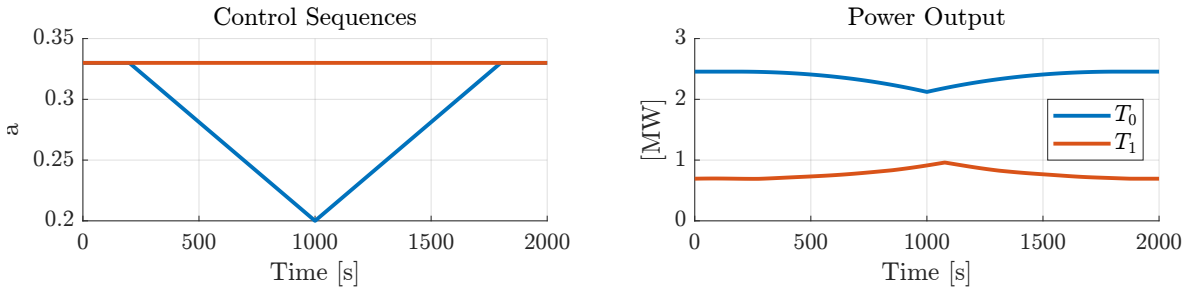

(a) The left panel illustrates the control sequences of the axial induction factor. The axial induction factor of the upstream turbine T_0 falls below 0.33 for a period of time, while that of the downstream turbine remains constant. The right panel depicts the resulted power output trajectories. It is evident that T_0 experiences a power de-rating, while simultaneously, the power output of T_1 increases. This is attributed to the de-rating of T_0 providing higher wind speeds to T_1.

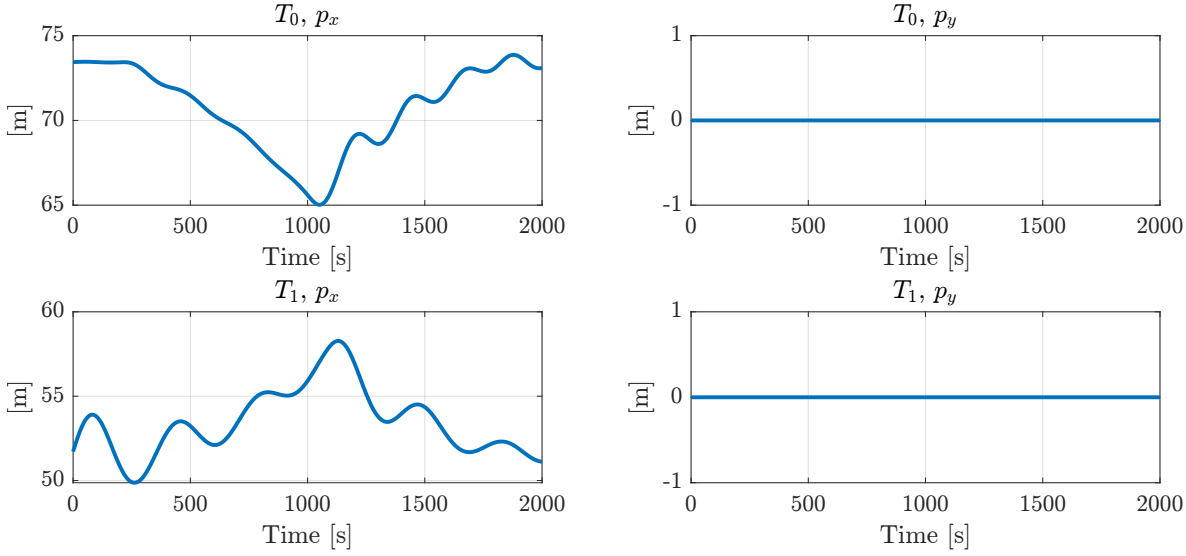

(b) This figure illustrates the impact of changing the axial induction factor on turbine positions. The top left panel shows that T_0 returns to its neutral position in the x-direction during derating due to the reduced aerodynamic thrust force. The bottom left panel indicates that T_0 deviates from its neutral position during derating, resulting in increased wind speed for the downstream turbine T_1. Consequently, T_1 experiences a larger aerodynamic thrust force, moving it away from its neutral position.

Figure 2-10: Case 1: Varying Axial Induction Factor

Case 2: Varying Rotor Yaw Angle The rotor yaw angle of T_0 follows a signal varying between -15 degrees and 15 degrees, while the rotor yaw angle of T_1 remains at 0 degrees. The specific control sequences can be found in the left panel of Figure 2-11a. In this case, the wind direction remains constant at 0 degrees, and the axial induction factor of both turbines remains constant at 0.33. The resulting power output trajectories and turbine movement trajectories can be found in the remaining panels of Figure 2-11. In Figure 2-13b, a snapshot of the floating wind farm at $t = 600$ s is presented to provide a clearer visualization.

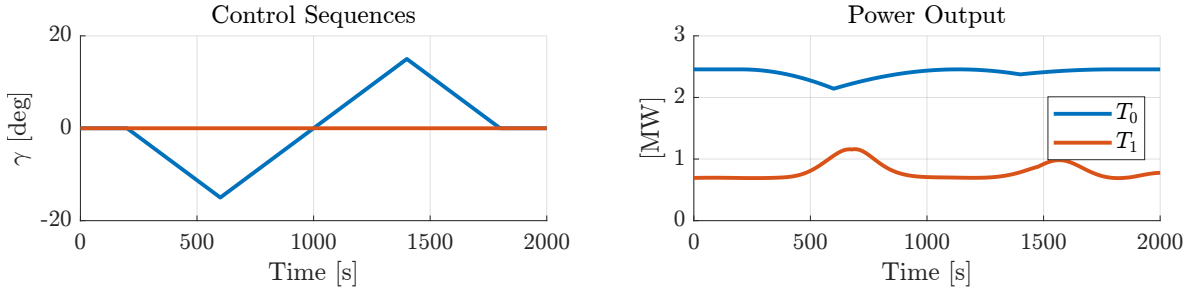

(a) The left panel describes the control sequences for rotor yaw angles. The rotor yaw angle of T_0 varies between -15 degrees and +15 degrees, while T_1 maintains a constant rotor yaw angle of 0 degrees. The right panel shows the resulted power output trajectories. It is evident that T_0 experiences two power output valleys due to misalignment of the rotor with the wind direction. T_1 exhibits two power output peaks because the yaw misalignment of T_0 induces crosswind turbine repositioning, which can be observed in the upper right panel of (b). As a result, the overlap between T_0's wake and T_1's rotor decreases, providing T_1 with higher wind speeds.

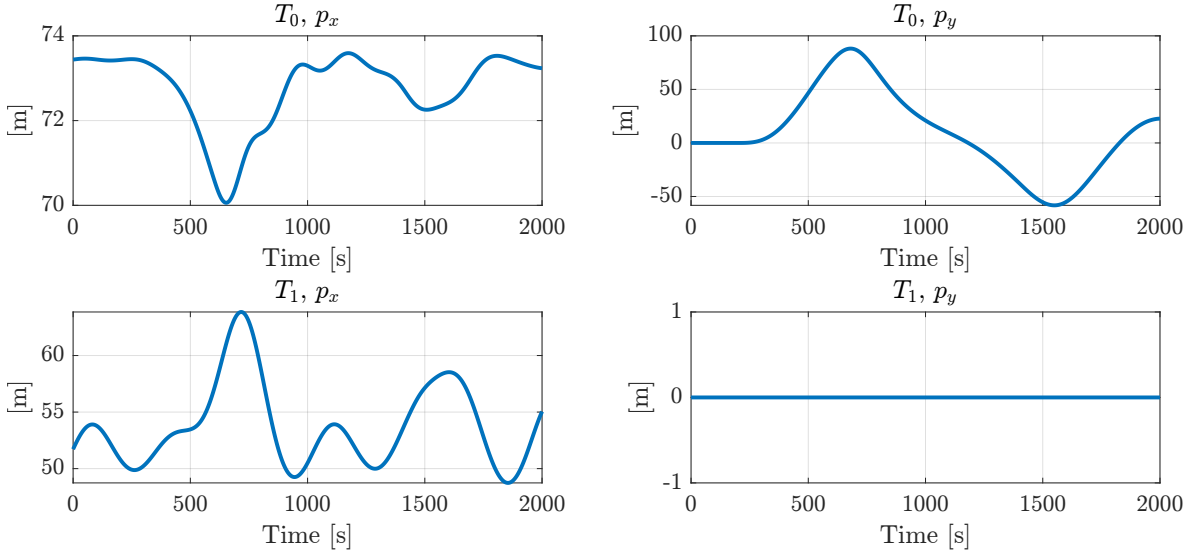

(b) This figure illustrates the impact of changing the rotor yaw angle on turbine positions. For T_0, yaw misalignment reduces the x-wind component of the aerodynamic thrust force, causing it to approach its neutral position twice in the x-direction, as seen in the top left panel. Simultaneously, yaw misalignment introduces an aerodynamic thrust force component in the y-direction, resulting in significant repositioning in the y-direction, as shown in the top right panel. For T_1, since its rotor remains aligned with the wind direction, there is no movement in the y-direction. However, due to the intermittent sweeping of T_0's wake across T_1, small fluctuations in the x-direction are observed.

Figure 2-11: Case 2: Varying Rotor Yaw Angle

Case 3: Varying Wind Direction In this case, the wind direction varies between -15 degrees and 15 degrees. The specific control sequence can be found in the left panel of Figure 2-12a. Here, the rotor yaw angles of both turbines remain at 0 degrees, and the axial induction factors remain at 0.33. The resulting power output trajectories and turbine movement trajectories can be found in the remaining panels of Figure 2-12. In Figure 2-13c, a snapshot of the floating wind farm at $t = 600$ s is presented to provide a clearer visualization.

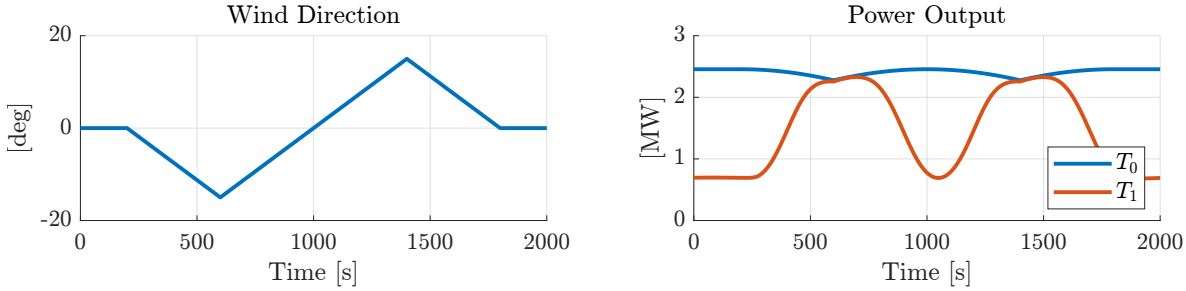

(a) The left panel depicts the variation trajectory of the wind direction in the wind farm. The right panel shows the resulting power output trajectories. The power output of T_0 exhibits two valleys due to rotor misalignment with the wind direction at those times. Conversely, T_1's power output shows two peaks as T_0's wake nearly completely avoids T_1's rotor during these periods.

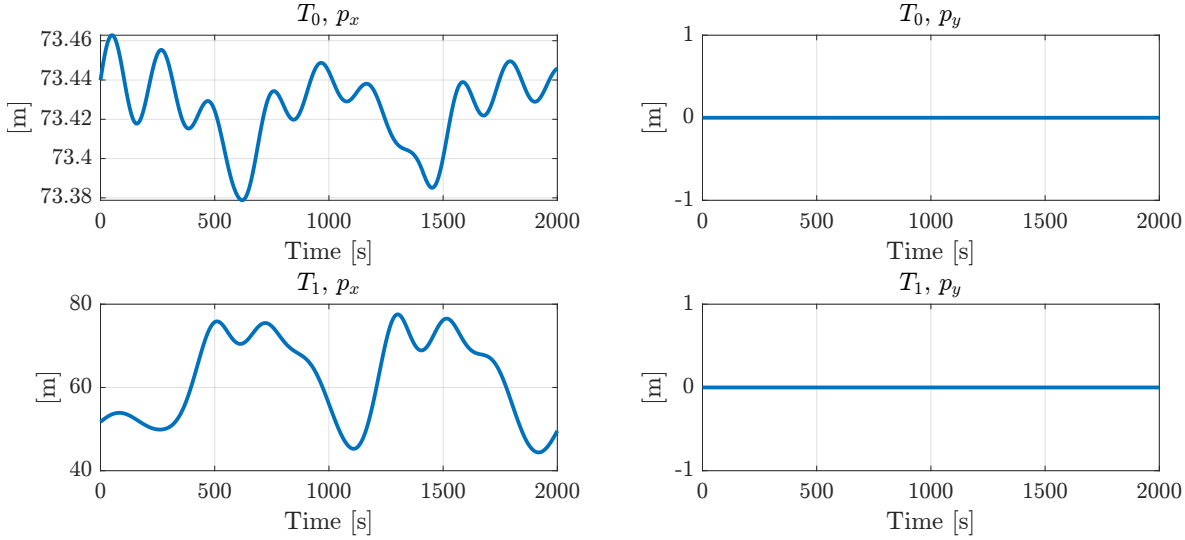

(b) This figure illustrates the impact of changing the wind direction on turbine positions. Since the rotor yaw angles of both turbines remain at 0 degrees, there is no movement in the y-direction. T_0 exhibits negligible movement in the x-direction. In contrast, T_1 shows significant movement in the x-direction with two peaks, as it experiences higher wind speeds at these times, pushing it further from its neutral point.

Figure 2-12: Case 3: Varying Wind Direction

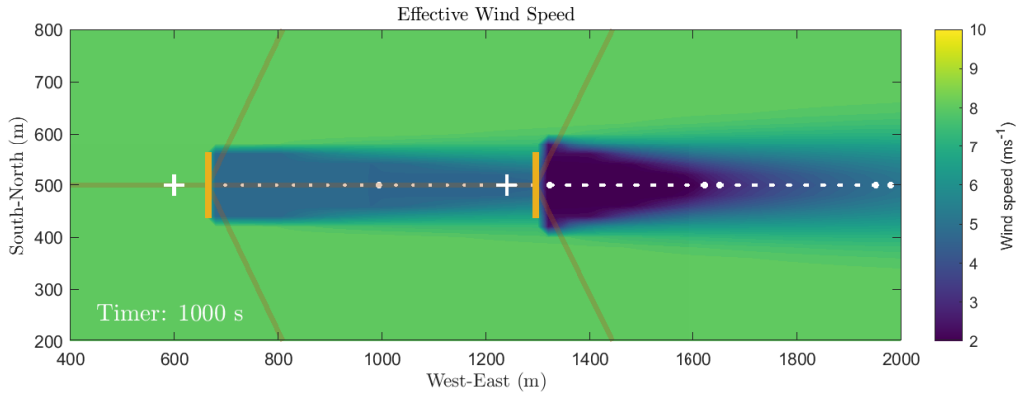

(a) Case 1: Varying Axial Induction Factor

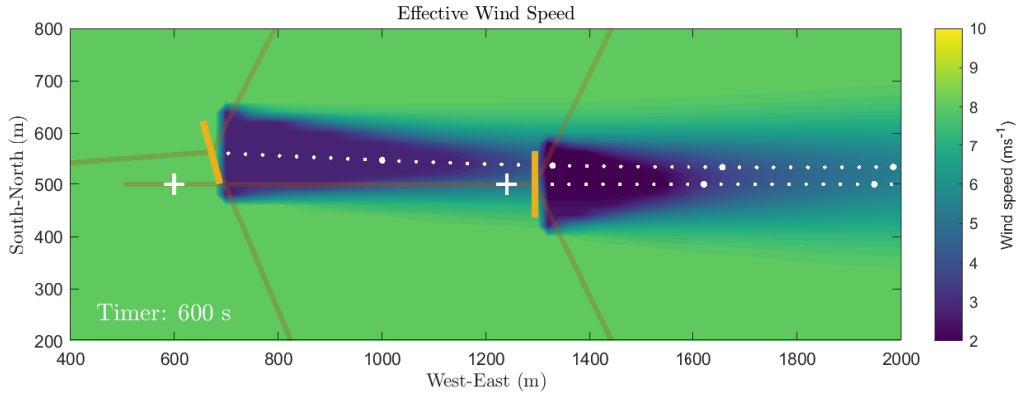

(b) Case 2: Varying Rotor Yaw Angle

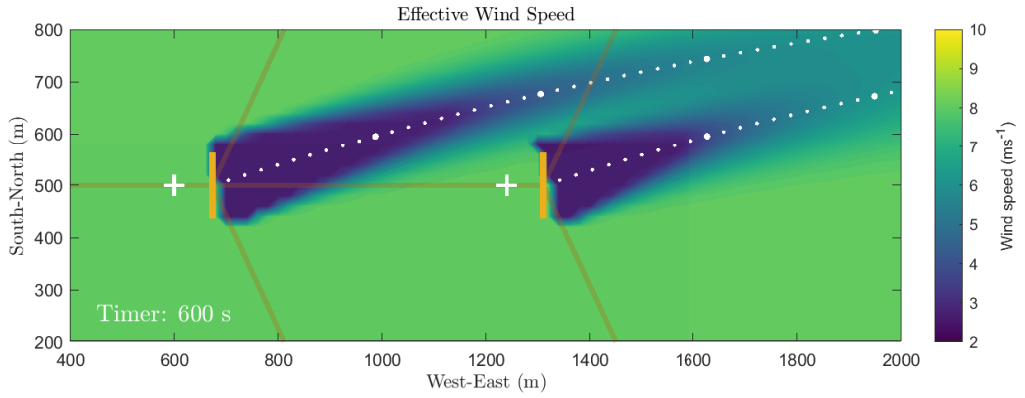

(c) Case 3: Varying Wind Direction

Figure 2-13: Three snapshots illustrating different cases: (a) varying axial induction factor at $t = 1000$ s, (b) varying rotor yaw angle at $t = 600$ s, and (c) varying wind direction at $t = 600$ s.

Chapter 3

Optimization Under Constant Wind Conditions for Maximum Energy Production

This chapter introduces a time-domain optimization approach for floating wind farms. The purpose of this chapter is to explore and analyze the optimal control sequences that can maximize the overall energy production of the previously defined two-turbine floating wind farm. Given that the mooring line stiffness of the floating turbine system influences both turbine stabilization and the turbine's movable range, this chapter specifically selects a series of different mooring line stiffness values to examine their impact on wind farm energy production and optimal control sequences. The chapter is organized as follows: in Section 3-1, the essential elements for performing the optimization are detailed. In Section 3-2, the optimized results in terms of total energy production and optimal control sequences over different mooring line stiffness are presented. Additionally, qualitative interpretations of the results are provided.

3-1 Optimization Framework

Due to the nonlinear nature of the floater's dynamics and the need to impose constraints on the control degrees of freedom, the task is categorized as a constrained nonlinear optimization problem. Therefore, the MATLAB function `fmincon` is selected [91]. In this section, the essential aspects that need to be considered for optimization will be explained.

Objective Function: Given the goal of maximizing the energy production of the floating wind farm over a period of time, the accumulated energy production during this period is formulated as the objective function. Considering the property of the `fmincon` function, which seeks the minimum, a negative sign is manually added in front of the accumulated energy production. Mathematically, the objective function can be expressed as follows:

$$Obj = -\sum_{i=0}^{n-1}\sum_{j=1}^{k}(P_{i,j}\cdot\Delta t)\ \text{[Joule]} \tag{3-1}$$

where n is the number of turbines in this wind farm, k represents the number of steps throughout the simulation, $P_{i,j}$ is the instantaneous power output for turbine T_i at time step j, and Δt is the duration between each simulation step. For this study, the optimization horizon for the two-turbine wind farm is set to 1800 seconds with a simulation step Δt of 4 seconds, resulting in 450 simulation steps.

Optimization Variables: Due to the lack of detailed prior knowledge about the optimal control sequence, the optimization variables are chosen as a series of equidistant sample points for each control degree of freedom for each turbine in the time domain. The behavior of the control degrees of freedom between each sample point is obtained through linear interpolation.

For the study in this chapter, the selection of optimization variables for the $1800s$ optimization horizon is explained as follows. For turbine T_i, the rotor yaw angle $\gamma_{i,1}$ at $t = 25s$ is chosen as the first optimization variable. Subsequently, every $\Delta t_\gamma = 25s$ interval of the rotor yaw angle is also treated as an optimization variable. The rotor yaw angle at $t = 0s$ is not optimized and is set to 0 degrees to ensure a smooth transition as it begins to change. This setup results in the control sequence for one turbine having 72 optimization variables, leading to a total of 144 optimization variables for the two-turbine floating wind farm.

It should be noted that the study in this chapter concentrates on the rotor yaw angle as the control degree of freedom. The axial induction factor at each time point is not optimized and is kept constant at 0.33.

Constraints: Two types of constraints are imposed on the control inputs: the upper and lower bounds of the control inputs, and the maximum rate of change of the control inputs. The latter constraint is due to the limited ability of the yaw mechanism to rapidly follow changes. These constraints can be expressed as:

$$\begin{cases} \gamma_{i,m} < \textit{upper bound} \\ \gamma_{i,m} > \textit{lower bound} \\ \gamma_{i,m+1} - \gamma_{i,m} < \Delta\gamma_{max} \cdot \Delta t_\gamma \\ \gamma_{i,m} - \gamma_{i,m+1} < \Delta\gamma_{max} \cdot \Delta t_\gamma \end{cases}$$

where $\gamma_{i,m}$ represents the mth rotor yaw angle in the control sequence for turbine i, $\Delta\gamma_{\max}$ is the maximum yaw angle changing rate in units of deg/s, and Δt_γ is the interval between each adjacent optimization variable. Here the upper bound is set to be 40 degrees, the lower bound is -40 degrees, $\Delta\gamma_{\max}$ is set to be 0.3 deg/s [97], and $\Delta t_\gamma = 25$s.

Initial Guesses: Due to the nonlinear nature of the optimization problem and unknown convexity, the choice of an initial guess is crucial for convergence speed and finding the global optimum. Three approaches were considered: zero initialization, intuitive values, and multi-start. For this study, we employed the second approach, setting initial guesses based on intuitive values aligned with the problem context. Specifically, optimization variables for the upstream turbine were set to +10 degrees and for the downstream turbine to -10 degrees, based on the hypothesis that this arrangement would create distance between the turbines in the crosswind direction.

Optimization Algorithms: The `fmincon` function in MATLAB provides various optimization algorithms, such as the interior point, trust region-reflective, sequential quadratic programming (SQP), and active set methods. According to MATLAB's recommendation, the

interior point method is primarily used. However, since the interior point method is designed for convex problems, it may only reach local minima if it's used on non-convex problems. Thus, SQP is also employed to compare its optimization results with those obtained using the interior point method to determine if there are differences. Experimental results during this study indicate that both SQP and the interior point method yield nearly identical optimal control sequences, with no significant difference in convergence time. Therefore, the interior point method is chosen as the optimization method for this study. For stopping criteria, both step tolerance of 1×10^{-3} and optimality tolerance of 1×10^{-2} are set.

Wind Field Setting: The wind conditions are set at a wind speed of 8.2 m/s, which lies in the below-rated region for the chosen NREL 5MW turbine. The wind direction is 0 degrees, blowing from due west to due east.

3-2 Optimized Results and Initial Observations

This section demonstrates the enhancement of energy production after optimization under various mooring line stiffness, the optimal sequence for rotor yaw angles, and the trajectories of the turbines in crosswind directions. The motivation for studying the impact of different mooring line stiffness on optimization results stems from the role of mooring lines in turbine platform stabilization. In floating wind turbine systems, mooring lines are designed to maintain the stability of the wind turbine. Therefore, tighter mooring line settings can reduce the burden on turbine stabilization tasks. However, for turbine repositioning, tighter mooring lines may decrease the effectiveness of wake mitigation due to the reduced movable range of the floating turbine. Motivated by this, the study investigates the effects of various mooring line stiffness settings on optimization results.

In this study, the mooring line stiffness is altered by changing the horizontal anchor-fairlead distance at the turbine's neutral position while keeping the mooring line length constant. Nine different distances, ranging from 717 m to 797 m in intervals of 10 m, are selected for optimization. Note that a larger horizontal anchor-fairlead distance implies greater stiffness, indicating a tighter mooring line setting.

In Figure 3-1, the average power output over an 1800-second optimization horizon across different anchor points is plotted. The average power output is calculated by dividing the accumulated energy production in megajoules by the optimization horizon in seconds. It can be observed that the farther the anchor is placed from the turbine's neutral position, the smaller the energy production increase that can be achieved through optimization.

In addition, the average power outputs for the no control cases are also plotted in Figure 3-1. Here, "no control" refers to the condition where the rotor yaw angles of both turbines continuously align with the wind direction. The dashed line represents the power output of the no control case with fixed-bottom turbines. Since the position of the turbines does not change in this scenario, their power output remains constant at 3.178 MW regardless of changes in the anchor point. The solid line with triangle markers represents the power output for the no control case with floating turbines. It can be observed that as the anchor point is positioned further away, this value gradually increases and approaches 3.178 MW, the power output of the no control case for fixed-bottom turbines. This is because the more slack the mooring line, the greater the range of movement allowed, enabling the upstream

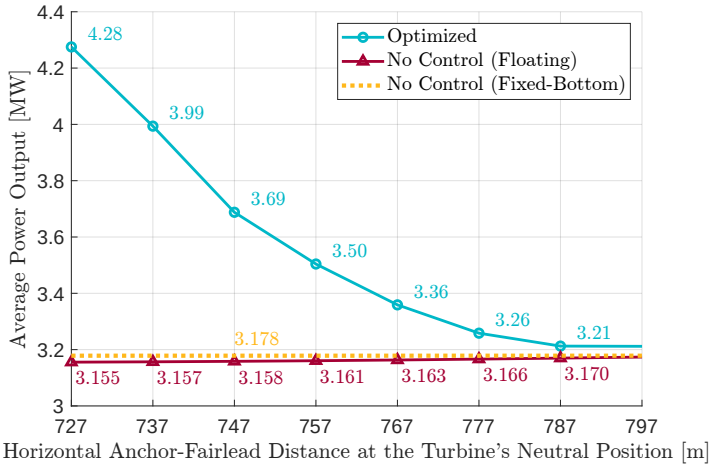

Figure 3-1: The solid cyan line with circle markers shows the total average power output after the optimization. It can be observed that as the mooring line gets tighter, the resulting total average power output enhancement through optimization becomes weaker. Additionally, the total average power outputs for two no-control cases, one based on a floating wind farm and one based on a fixed-bottom wind farm, are plotted using a ruby solid line and a yellow dashed line, respectively.

turbine to shift further in the downwind direction under steady conditions. This, in turn, slightly reduces the distance between the two turbines in the downwind direction, resulting in lower wind speeds faced by the downstream turbine and thus a lower overall power output compared to settings with tighter mooring lines.

We now turn to the examination of the optimal control sequences. When the mooring line is relatively slack, the optimal control sequences, shown in Figure 3-2a, are in line with the intuitive expectation. After a brief period of transient behavior at the beginning, the optimized rotor yaw angles of the upstream and downstream turbines each stabilize at a constant value, with opposite signs. These control sequences result in relocating the upstream turbine to a new position in the -y direction while steering the downstream turbine to a new steady-state position in the +y direction. The complete crosswind direction trajectories of the turbines can be found in Figure 3-4a. Since the optimization results under the relatively slack mooring line settings tend to reposition the turbines to a stationary position over time, we refer to this outcome as static repositioning. Comparing the optimal yaw sequences for the 717m, 727m, and 737m cases in Figure 3-2a, it can be observed that in steady-state conditions, the tighter the mooring line, the greater the yaw misalignment. This is because a larger mooring line force requires a greater aerodynamic thrust force to achieve a balance of forces while maintaining a certain distance between the two turbines in the crosswind direction.

For a more intuitive understanding of how this static repositioning works, a snapshot at $t = 400$s from the animation portraying the optimization result for the 737m case is shown in Figure 3-3. Additionally, the movement trajectories of the turbines over the first 400 seconds are depicted using color-coded lines, with the same color indicating the positions of the turbines at the same time step. The positions marked in red represent the initial locations of the turbines, while the positions marked in dark navy blue indicate the new positions to which the turbines are repositioned at $t = 400$ seconds.

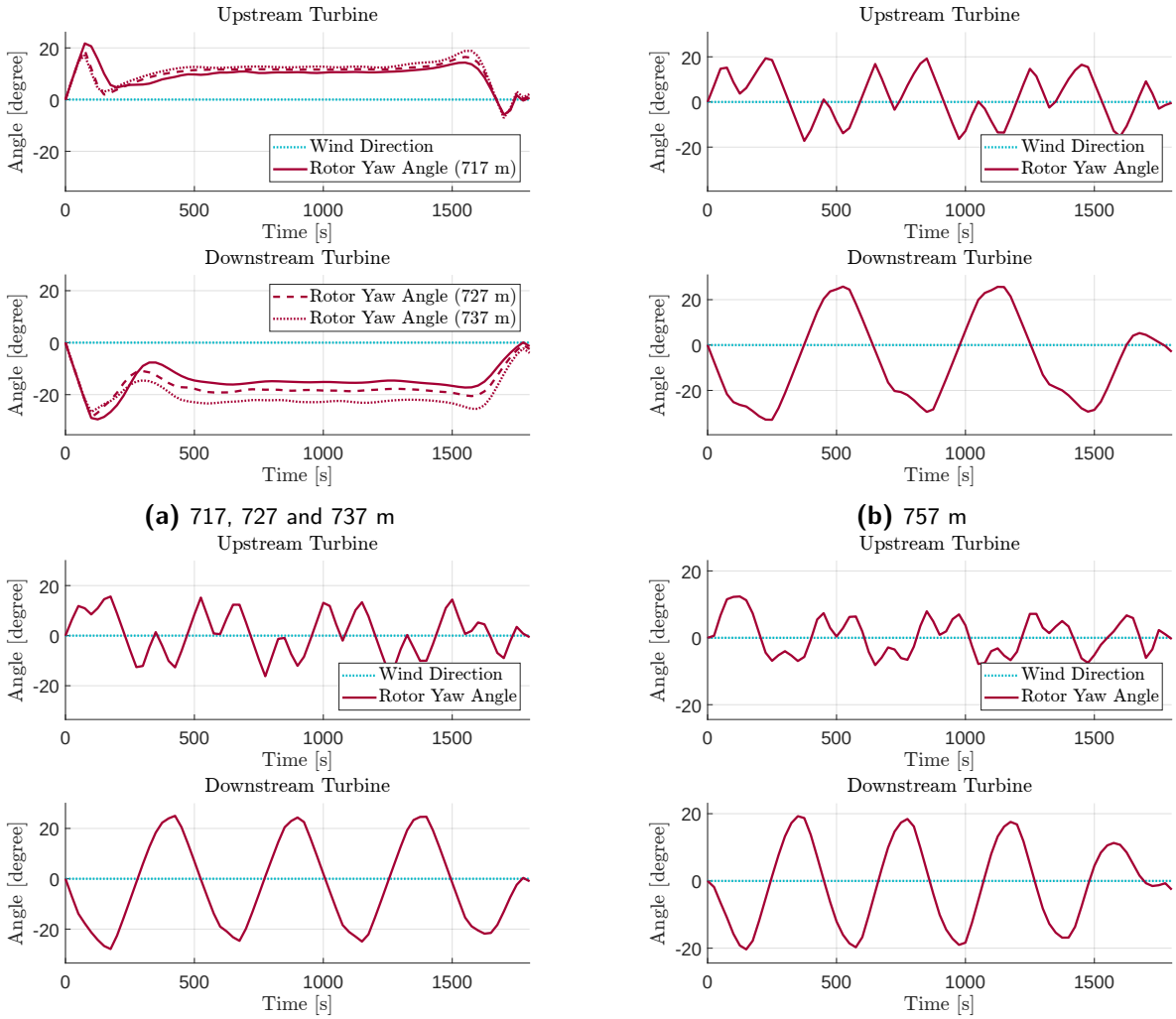

(a) 717, 727 and 737 m

(b) 757 m

(c) 767 m

(d) 777 m

Figure 3-2: Optimal Control Sequences under Different Horizontal Anchor-Fairlead Distances at the Turbine's Neutral Position

Next, we observe the shape of the optimal control sequence when the mooring line becomes tighter. Here we examine the 757m, 767m, and 777m cases, as shown in Figure 3-2b, c and d. An interesting phenomenon occurs: the optimal control trajectories under these mooring line settings exhibit periodicity, despite the fact that the wind conditions remain constant and the initial guesses contain no additional frequencies. For now, let us examine the 767m case to understand how the optimized control sequences influence the turbines' trajectories in the crosswind direction. As depicted in Figure 3-4b, the quasi-sinusoidal control inputs from Figure 3-2c result in both turbines moving in a sinusoidal pattern in the crosswind direction. Due to the fact that the turbines are repositioned in a dynamic manner, we refer to this type of optimized result as dynamic repositioning.

This oscillating behavior in the crosswind direction indicates that the wake of the upstream turbine periodically sweeps over the downstream turbine, which might seem counter-intuitive considering the basic idea is to keep the downstream turbine as far away from the wake as

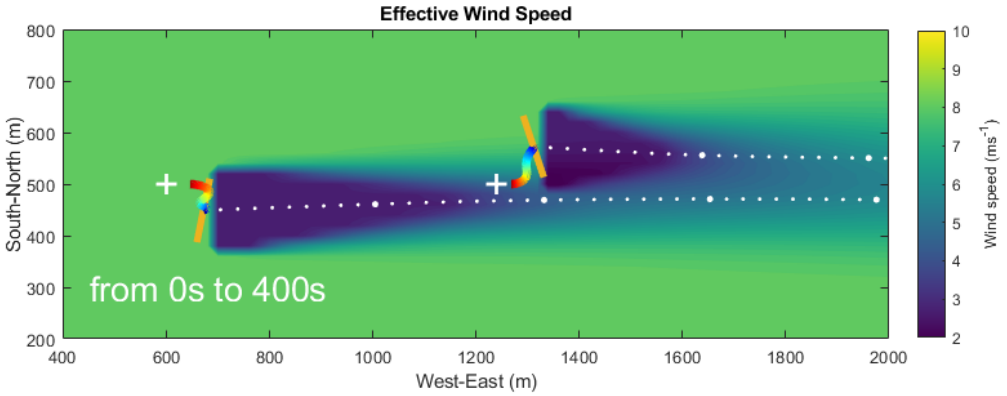

Figure 3-3: A visualization for the static repositioning. The movement trajectories from $t = 0$ seconds to $t = 400$ seconds for two turbines are shown using the rainbow-colored lines. The positions marked in red represent the initial locations of the turbines, while the positions marked in dark navy blue indicate the new positions to which the turbines are repositioned at $t = 400$ seconds. Additionally, the background shows the effective wind speed at $t = 400$ seconds.

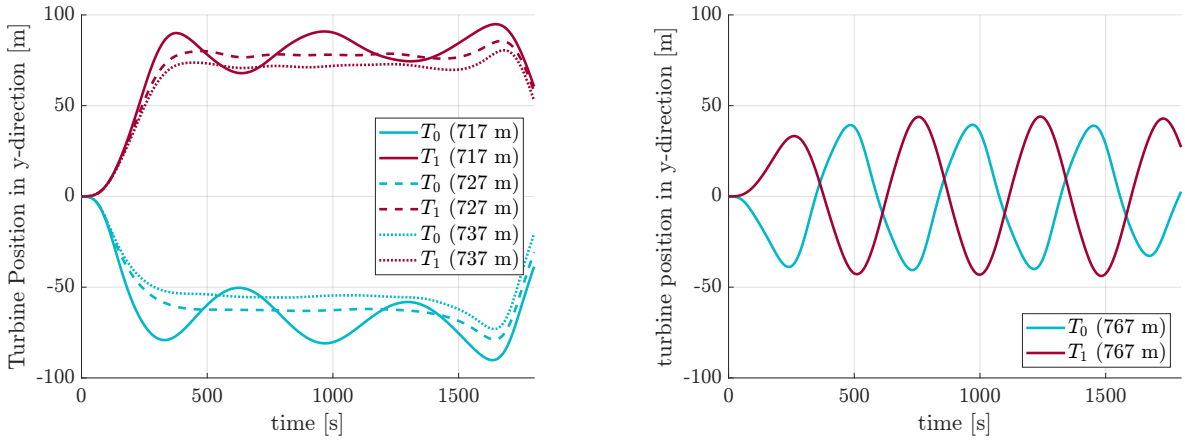

(a) Static Repositioning **(b)** Dynamic Repositioning

Figure 3-4: Two Patterns from Optimization Across Different Mooring Stiffness

possible. However, in fact, such a dynamic repositioning approach is reasonable. This is because for floating wind farms with tight mooring lines, merely considering static repositioning results in a limited movable range for the turbines, which is insufficient to effectively allow downstream turbines to avoid the wake of upstream turbines. In other words, it is not feasible to ensure that downstream turbines continuously benefit from high wind speeds.

However, when considering that turbines have a certain speed and the mooring line acts like a spring, the moving turbines can travel to farther positions, even if they cannot statically stay at those positions because they will be pulled back by the mooring line. The control concept of dynamic repositioning leverages this increased movable range provided by the moving turbines, allowing downstream turbines to periodically and intermittently benefit from high wind speeds, thereby enhancing the overall energy production of the wind farm.

3-3 Summary

In this chapter, the optimization provides us with the following information regarding the optimal control signals: for wind farms with relatively slack mooring lines, the optimal control signals follow the concept of static repositioning; for wind farms with relatively tight mooring lines, the optimal control signals follow the concept of dynamic repositioning.

This insight leads to the subsequent research question of this study: whether dynamic repositioning can bring higher energy production gains to wind farms with relatively slack mooring lines, and conversely, whether static repositioning can bring higher energy production gains to wind farms with relatively tight mooring lines. The next chapter investigates the shapes of the optimal control sequences under these two control strategies in detail and provides answers through grid-search-based optimization approaches.

Chapter 4

Static and Dynamic Repositioning: A Comprehensive Analysis

This chapter builds on the findings of Chapter 3, providing an in-depth analysis of the control signal shapes for both static repositioning and dynamic repositioning control strategies.

4-1 Static Repositioning

In this section, the control strategy of static repositioning is thoroughly investigated. The goal of this section is to determine whether applying this static repositioning strategy to wind farms with tight mooring lines can result in higher energy production gains. Section 4-1-1 analyzed the composition of the optimal control sequences under static repositioning and provided the analytic expression for control sequences that enable wind farms to undergo static repositioning. Section 4-1-2 uses a grid search to obtain the optimal control signals for each mooring line stiffness setting and the resulting energy production gains. Section 4-1-3 compared the results from the grid search with those obtained using `fmincon` in Chapter 3, and discussed the implications of static repositioning.

4-1-1 Derivation of the Analytical Expression for Control Sequences

From Figure 4-1, it can be observed that the optimal control sequences consist of three phases: an initial transient phase, a steady-state middle phase, and a final transient phase.

From the optimizer's perspective, this optimization result, which includes two transient phases and one steady-state phase, corresponds to the turnpike effect in the field of optimal control [94, 40, 29]. The turnpike describes a situation where the optimal trajectory of a dynamic system spends most of the time near a certain steady-state path (metaphorically like a turnpike road in reality).

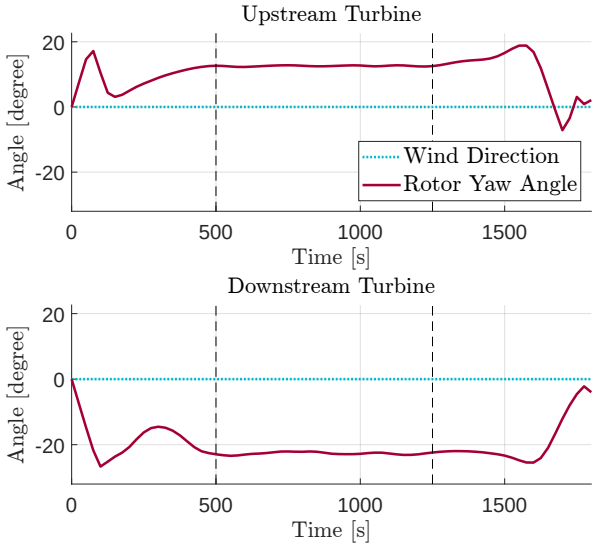

Figure 4-1: Optimal control sequences for the 737 m case, demonstrating static repositioning.

For a long optimization horizon, the optimal control strategy often spends a significant portion of the time near a steady-state solution, because this state minimizes the integral cost over a long period, in our case, the accumulated energy production calculated by (3-1). This corresponds to the middle phase where the control inputs stabilize to maintain efficient system performance over time. In Lars Grüne's article [40], the turnpike in economic receding horizon control without terminal constraints is systematically and mathematically discussed. The study points out that as the receding horizon grows, the approximate optimal performance can converge to the exact optimal performance exponentially fast. This implies that the middle steady-state phase of the optimal control sequence obtained when the receding horizon is sufficiently long is of significant reference value.

The existence of the two transient phases is explained here. At the beginning of the control sequence, the system is not at the optimal steady-state and needs to adjust quickly from its initial states to approach the optimal steady-state path. This phase accounts for the transient behavior at the start. As the optimization horizon progresses, the remaining time yet to be optimized decreases. This change in the time horizon affects the relative importance of immediate versus long-term costs. Near the end of the horizon, the system's focus shifts toward minimizing short-term costs because the benefit of maintaining the long-term steady-state diminishes. As a result, the system's control strategy adapts to prioritize immediate gains over long-term steady-state benefits, even in the absence of terminal constraints. In other words, the final transient phase arises from the settings of the optimal control problem's running costs, terminal cost, and terminal constraints. It is a byproduct from a purely mathematical perspective of attempting to obtain infinite horizon optimization results using finite horizon optimization.

As a result, in this study, considering the turnpike effect, the two transient phases are omitted from the analysis, and only the middle steady-state phase is focused on. Therefore, under static repositioning, the control sequences for the two turbines are described by the following

analytical expression:

$$u_{\text{Static},T_0}(t) = \gamma_0 \tag{4-1}$$

$$u_{\text{Static},T_1}(t) = \gamma_1 \tag{4-2}$$

where γ_0 represents the constant rotor yaw angle for the upstream turbine T_0, and γ_1 represents the constant rotor yaw angle for the downstream turbine T_1.

4-1-2 Optimal Value Determination for Control Sequence Parameters

This section investigates whether enforcing static repositioning on wind farms with tight mooring lines would bring higher energy production increase. By applying the control signals defined in (4-1) and (4-2), which adjust the rotor yaw angles of the upstream and downstream turbines based on γ_0 and γ_1, we transform the problem into a two-variable optimization.

A grid search on the two parameters will provide insight into the optimization surfaces and identify the control signal pair (γ_0^*, γ_1^*) that maximizes the total power output for the two-turbine wind farm. Grid search is a gradient-free optimization method that explores the solution space without relying on gradient information. This makes it particularly robust for non-convex functions, as it is less likely to get trapped in local minima compared to gradient-based methods. Additionally, grid search is simple to implement and interpret, allowing for clear visualization of the relationship between the variables. It is worth noting that the computational expense increases with the density of grid points. However, in this study, this limitation is not particularly pronounced.

Here, a 2D mesh grid with an interval of 5 degrees, ranging from -40 to +40 degrees, is laid out with the rotor yaw angle of T_0 as the x-axis and that of T_1 as the y-axis. The coordinates of each grid point are used as constant rotor yaw angles γ_0 and γ_1 fed into the system, and each simulation is run for 3500 seconds. This simulation duration is chosen to ensure that the turbines are re-positioned to the new position and have reached the corresponding steady state in terms of the floater's dynamics. The total power output of the wind farm, evaluated from each grid point, is taken as the value, and the contour of the entire mesh grid is shown in Figure 4-2.

4-1-3 Discussion

To facilitate comparison, each sub-figure uses the same color bar, as shown at the top of Figure 4-2. Firstly, it can be observed that when the mooring line is relatively slack (i.e., Figure 4-2a, b and c), there are maxima in both the first and third quadrants, marked by white asterisks ($*$). For instance, for the 737m case, the coordinates of the two maxima are (+10, -25) and (-10, +25). This is due to the symmetry of the two-turbine floating wind farm. The results brought by these two maxima are that T_0 is positioned negatively and T_1 positively in the crosswind direction, and vice versa. Although these are two different layouts, the resulting energy production increase is equivalent.

Secondly, it can be observed that as the mooring line becomes tighter, the two maxima gradually fade and eventually disappear, converging into a single maximum at (0, 0), indicating that no yaw misalignment is the optimal behavior for the wind turbines. In Figure 4-3a, the

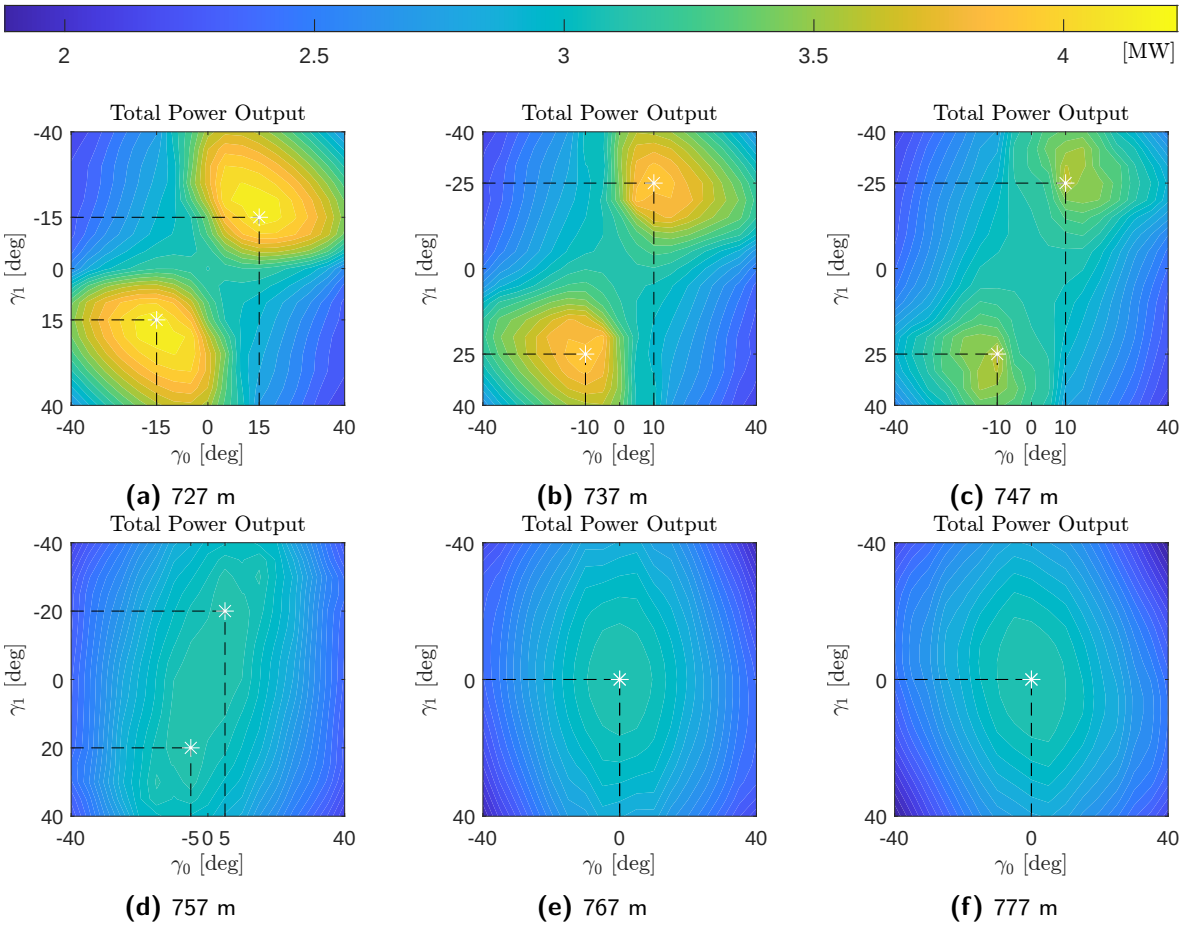

Figure 4-2: Grid Search Evaluation for Different Mooring Stiffness

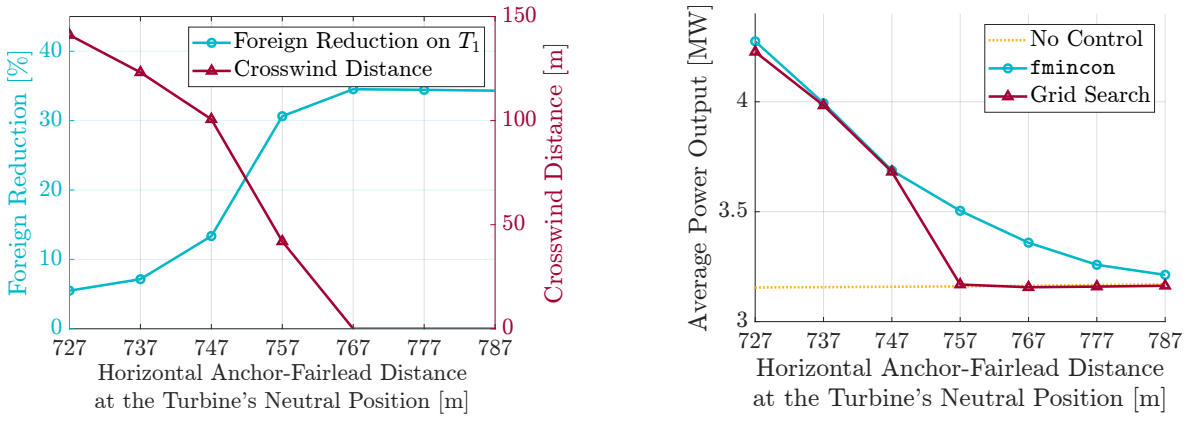

Figure 4-3: (a) Wind speed reduction at T_1 and crosswind distance between two turbines across different mooring line stiffnesses. (b) Optimal average power output under static repositioning using grid search, shown with a ruby line and triangle markers. For comparison, results obtained using `fmincon` from Chapter 3 are also plotted, shown with a cyan line and circle markers.

wind speed reduction due to the upstream wake on T_1 and the separation distance between the two turbines in the crosswind direction are presented. Among these, the 757m case serves as a typical example. Taking the maximum point in the first quadrant of Figure 4-2d as an example, the optimal yaw misalignment of the two turbines creates approximately 42 meters of spacing between them in the crosswind direction. This optimal adjustment reduces the wind speed reduction at T_1 caused by T_0's wake from 34.52% to 30.64%, thereby providing T_1 with a higher wind speed. However, despite these efforts, for this case, the efforts made by both rotors' yawing barely bring any overall power output increase, as shown in Figure 4-3b. Further, as the mooring gets even tighter, if only static repositioning is allowed, the optimal rotor yaw angles fall back to both rotors having no misalignment.

It must be acknowledged that in cases with tight mooring lines, such as the 787m case, whether T_0's rotor misaligns also depends on the downwind distance between the two turbines' neutral positions. In this study, a 5D spacing is set. For this specific setting, the best choice is for T_0 not to misalign at all. However, when the downwind distance between the two turbines' neutral positions is greater, yaw-based wake redirection might be activated. This scenario would manifest as the upstream wake being redirected using yaw misalignment, even though the two turbines cannot be repositioned much due to a very tight mooring line setting.

Finally, a comparison is made between the optimal performance of static repositioning and the optimization results from `fmincon`, as shown in Figure 4-3b. This comparison addresses the previously posed question of whether the static repositioning control strategy can yield higher energy production gains compared to dynamic repositioning for wind farms with tight mooring lines. The findings indicate that it does not.

In summary, as the mooring line tightens, the turbine's movable range becomes smaller. Simultaneously, due to the fact that yaw misalignment sacrifices the turbine's own power output, the optimal behavior of the wind farm under static repositioning gradually evolves from T_0's wake just avoiding T_1's rotor to T_0's wake completely shadowing T_1.

4-2 Dynamic Repositioning

In this section, the control strategy of dynamic repositioning is investigated. The goal of this section is to determine whether applying this dynamic repositioning strategy to wind farms with slack mooring lines can result in higher energy production gains. Section 4-2-1 extracted the dominant frequency domain information of the optimal control sequences under dynamic repositioning using Fast Fourier Transform (FFT). Based on this, six parameters were selected to construct the analytic expression for control sequences that enable the wind farm to undergo dynamic repositioning. Section 4-2-2 proposed an optimization method combining block coordinate descent and grid search to find the optimal values of these six parameters, thereby obtaining the optimal control signals for wind farms with any mooring line stiffness.

4-2-1 Derivation of the Analytical Expression for Control Sequences

To enforce dynamic repositioning behavior on wind farms with any mooring line stiffness, it is only necessary to prescribe the control sequence that each rotor yaw angle should follow.

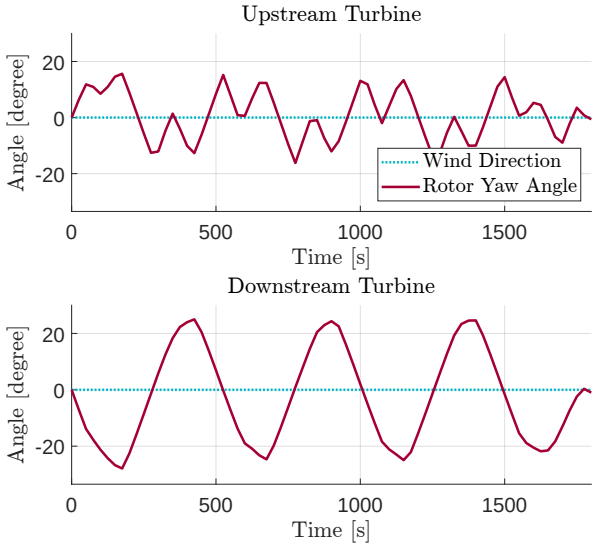

Figure 4-4: Optimal Control Sequences for the 767 m Case

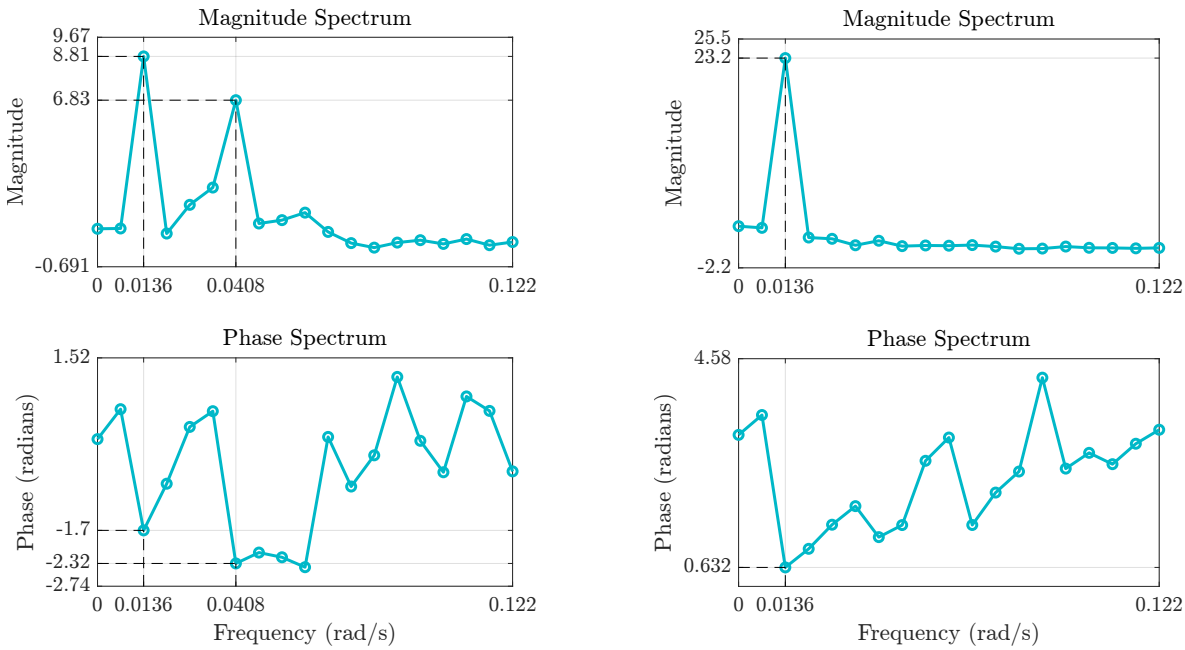

(a) Upstream Turbine T_0 **(b)** Downstream Turbine T_1

Figure 4-5: The magnitude and phase spectra of the optimal control sequences (767 m)

This section selects six parameters to describe the shape of the optimal control sequences under dynamic repositioning. The definition of these six parameters and the reasons for their selection will be explained below, using the 767 m case as an example.

Observing Figure 4-4, it can be seen that the optimal control sequence for the upstream turbine T_0 contains a fundamental signal with harmonic component(s), while the optimal control sequence for the downstream turbine T_1 can be described by a single-frequency sine wave. This observation suggests that the shape of the entire control sequence can be described using a linear combination of sine waves. To extract this frequency-domain information, Fast Fourier Transform (FFT) was performed on both optimal control sequences, with the results shown in Figure 4-5. For those interested, the FFT results for other mooring line stiffness cases are shown in Appendix Section A-1.

Observing the upper panel of Figure 4-5a, it can be seen that the magnitude spectrum of the optimal control sequence for the upstream turbine T_0 contains two spikes, indicating that the control sequence for T_0 is dominated by two frequency signals. The frequency corresponding to the second spike, 0.0408 rad/s, is approximately three times that of the first spike, 0.0136 rad/s. Therefore, the frequency corresponding to the first spike is referred to as the fundamental frequency, denoted by ω_1, while the frequency corresponding to the second spike is referred to as the third harmonic, denoted by ω_3. Observing the lower panel of Figure 4-5a, it can be seen that there is a phase difference between the ω_1 and ω_3 signals. Hence, this phase difference is selected as another parameter in describing the optimal control sequences, denoted by $\Delta\phi_3$.

Furthermore, by examining the magnitude spectrum of the optimal control sequence for the downstream turbine T_1 in Figure 4-5b, it can be observed that this signal is dominated by a single frequency, which matches the fundamental frequency of the optimal control sequence for the upstream turbine. However, despite the upstream and downstream turbines sharing the same fundamental frequency, there is a phase difference according to the phase spectra. Hence, this phase difference between the two fundamental frequency signals is selected as another parameter in describing the optimal control sequences, denoted by $\Delta\phi_1$.

To summarize, the following six parameters are selected to describe the control sequences that enforce dynamic repositioning of the wind farm:

$$\begin{bmatrix} \Delta\phi_1 & \omega_1 \\ A_{1,T_0} & A_{1,T_1} \\ A_{3,T_0} & \Delta\phi_3 \end{bmatrix}$$

where A_{1,T_0} is the amplitude of the fundamental component of the control sequence for the upstream turbine T_0, A_{3,T_0} is the amplitude of the third harmonic component of the control sequence for the upstream turbine T_0, and A_{1,T_1} is the amplitude of the fundamental component of the control sequence for the downstream turbine T_1. Consequently, the control sequences for dynamic repositioning can be represented by the following analytic expressions:

$$u_{\mathrm{Dyn},T_0}(t) = A_{1,T_0}\sin(\omega_1 t) + A_{3,T_0}\sin(3\omega_1 t + \Delta\phi_3) \tag{4-3}$$

$$u_{\mathrm{Dyn},T_1}(t) = A_{1,T_1}\sin(\omega_1 t + \Delta\phi_1) \tag{4-4}$$

4-2-2 Optimal Value Determination for Control Sequence Parameters

In the previous section, we identified six parameters to describe the control sequences that enforce the wind farm to undergo dynamic repositioning. The next step is to determine the optimal values of these parameters to obtain the optimal control sequences for each given mooring line stiffness. Consequently, an optimization method combining block coordinate descent and grid search is proposed.

The specific steps of this optimization approach are shown in Figure 4-6, and explained as follows:

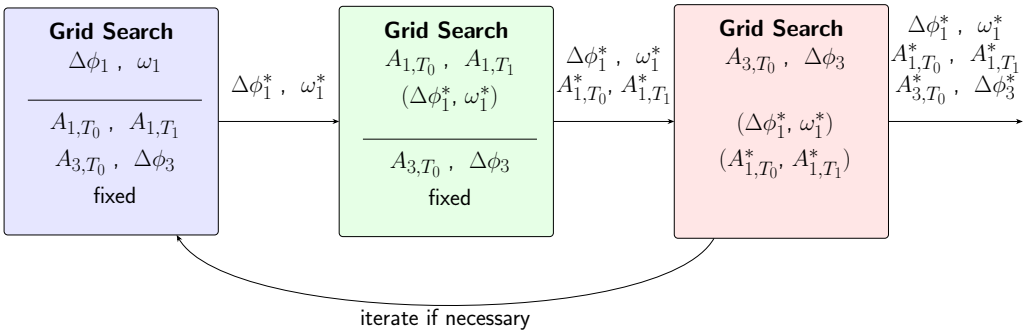

Figure 4-6: This figure illustrates the optimization strategy combining block coordinate descent with grid search used in each block. Each block represents a stage in the optimization process where specific parameters are fixed and others are optimized through grid search.

1. The six optimization parameters are grouped by priority. The parameters are grouped as follows:
   - Group 1: Phase difference $\Delta\phi_1$ and fundamental frequency ω_1.
   - Group 2: Amplitude A_{1,T_0} and A_{1,T_1}.
   - Group 3: Phase difference $\Delta\phi_3$ and amplitude A_{3,T_0}.
2. The values of the parameters in Groups 2 and 3 are fixed at initial values, and a grid search is used to find the current optimal values of the two parameters in Group 1, $\Delta\phi_1^*$ and ω_1^*.
3. Using $\Delta\phi_1^*$ and ω_1^*, a grid search is conducted to find the optimal values of the parameters in Group 2, A_{1,T_0}^* and A_{1,T_1}^*, while keeping the parameters in Group 3 fixed.
4. Using the optimal values of the first four parameters, a grid search is performed to find the optimal values of the parameters in Group 3, A_{3,T_0}^* and $\Delta\phi_3^*$.
5. If necessary, repeat the process starting from step 2.

The rationale for the grouping is explained as follows. $\Delta\phi_1$ coordinates the relationship between the upstream and downstream turbines, ensuring that the upstream wake sweeps across the downstream turbine at the highest relative speed. Without the precise coordination provided by $\Delta\phi_1$, other parameters cannot fundamentally bring about an increase in overall

energy production, making it the most critical parameter. The fundamental frequency ω_1 exploits the floater's frequency response characteristics to minimize the overlap time between the upstream wake and the downstream rotor. This will be elaborated in detail in Section 4-3-1. Hence, these two parameters are prioritized for optimization. A_{1,T_0} and A_{1,T_1} are the next two parameters that determine the maximum speed at which the upstream wake sweeps across the downstream turbine. Experiments have shown that the contribution of the fundamental frequency component to energy production enhancement is significant compared with the third harmonic component under dynamic repositioning. Therefore, these two parameters related to the fundamental frequency are optimized next. Finally, $\Delta\phi_3$ and amplitude A_{3,T_0} are optimized.

To better illustrate the proposed optimization approach, the 767m case is used as an example. The process is carried out in three main stages as described below:

Optimization of $\Delta\phi_1$ and ω_1: The search range for ω_1 is chosen to be between 0.01 to 0.02 rad/s, with an interval of 0.001 rad/s. The rationale for selecting this searching range is based on a key finding of this research: the optimal fundamental frequency ω_1^* is located near the natural frequency of the floater's dynamics in the y-direction. For the 767m setting, this natural frequency is estimated to be 0.0132 rad/s. Therefore, the search range of 0.01 to 0.02 rad/s is chosen for the optimal fundamental frequency. The detailed relationship between the optimal fundamental frequency and the floater dynamics will be discussed in Section 4-3-1, and the calculation process for estimating the natural frequency of 0.0132 rad/s for the 767m setting will also be mentioned. Additionally, the search range for $\Delta\phi_1$ spans from $\pi/2$ to $3\pi/2$ with an interval of $\pi/12$. Meanwhile, the other four parameters are fixed at:

$$[A_{1,T_0}, A_{1,T_1}, A_{3,T_0}, \Delta\phi_3] = [15, 15, 0, 0]$$

The grid search result for this step is shown in the left plot of Figure 4-7.

Optimization of A_{1,T_0} and A_{1,T_1}: With the optimized values for ω_1 and $\Delta\phi_1$, the second round of grid search for A_{1,T_0} and A_{1,T_1} is performed by fixing:

$$[\Delta\phi_1, \omega_1, A_{3,T_0}, \Delta\phi_3] = [2.62, 0.014, 0, 0]$$

The searching range for these two parameters is set to be [0, 50]. The result for this round of grid search is shown in the middle plot of Figure 4-7, indicating that the optimized values are:

$$[A_{1,T_0}^*, A_{1,T_1}^*] = [10, 20]$$

Optimization of A_{3,T_0} and $\Delta\phi_3$: In the third round of grid search, all four previously optimized parameters are utilized to find A_{3,T_0} and $\Delta\phi_3$. The search range for A_{3,T_0} is set to [0, 30], and the range for $\Delta\phi_3$ is set to $[-\pi, \pi]$. The result is shown in the right plot of Figure 4-7.

It should be noted that after completing these three optimization steps, further iterations can be carried out to obtain more optimal parameters. However, additional iterations implemented in the course of this study indicates that further iterations contributed negligibly to performance improvement. The most significant enhancements were observed in the first iteration.

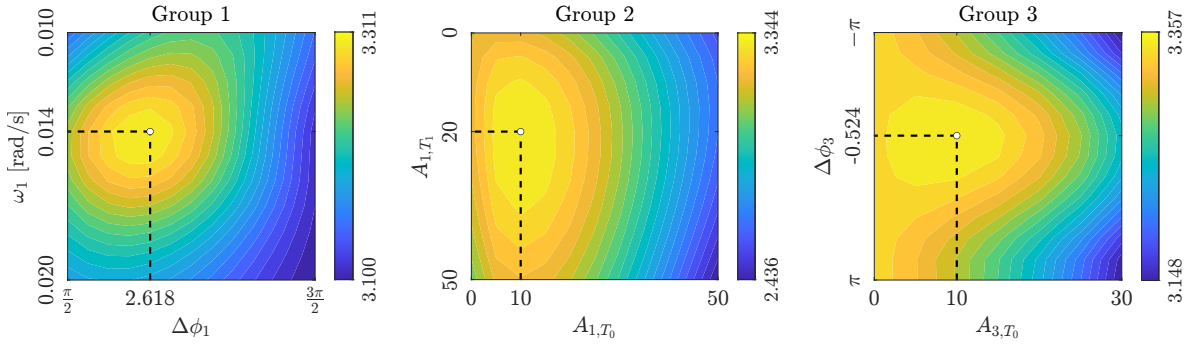

Figure 4-7: These three subfigures illustrate the grid search results for three groups of parameters for the 767m case, presented as contour plots. The optimal value for each parameter is indicated, and the overall average power output up to this step can be found in the top right corner of each subfigure, with units in MW.

In summary, the initial values and the optimized values for the parameters after the first iteration are shown below:

$$\begin{bmatrix} \Delta\phi_1 & \omega_1 \\ A_{1,T_0} & A_{1,T_1} \\ A_{3,T_0} & \Delta\phi_3 \end{bmatrix} = \begin{bmatrix} * & * \\ 15 & 15 \\ 0 & 0 \end{bmatrix} \longrightarrow \begin{bmatrix} 2.618 & 0.014 \\ 10 & 20 \\ 10 & -0.5236 \end{bmatrix}$$

Utilizing the optimized parameters, the optimal control sequences derived from this sequential grid search approach can be reconstructed, as depicted by the dashed lines in Figure 4-8a. It is evident that the sequential grid search yields results that are nearly identical to those obtained using `fmincon`.

4-2-3 Results and Discussion

This proposed grid search optimization procedure was performed for all mooring line stiffness, and the resulting average power outputs are illustrated in Figure 4-9, marked with triangle markers. Additionally, the curves from Figure 4-3b are overlaid here for comparison purposes. Two observations can be made from this comparison. Firstly, the grid search confirms that `fmincon` successfully finds the global optimum for achieving higher power outputs for each mooring line stiffness. Secondly, for wind farms with slack mooring lines, dynamic repositioning does not achieve superior power enhancement compared to static repositioning. This is because, in enforcing dynamic repositioning, we indirectly force the upstream wake to periodically sweep across the downstream turbine. However, in slack mooring settings, the downstream turbine is allowed to consistently avoid the upstream wake effectively. Hence, under dynamic repositioning, the unavoidable foreign shadow cast on the downstream turbine prevents it from outperforming static repositioning.

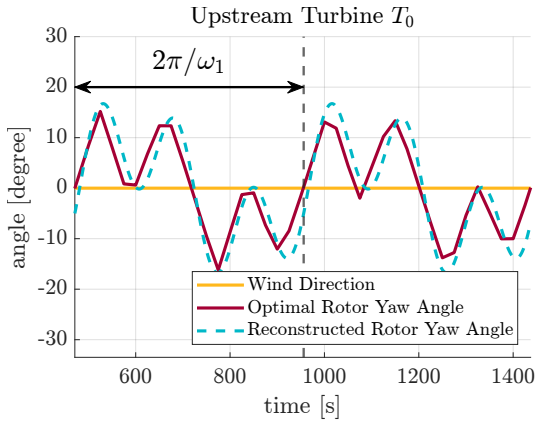

(a) A segment of the optimal control sequences obtained from `fmincon`.

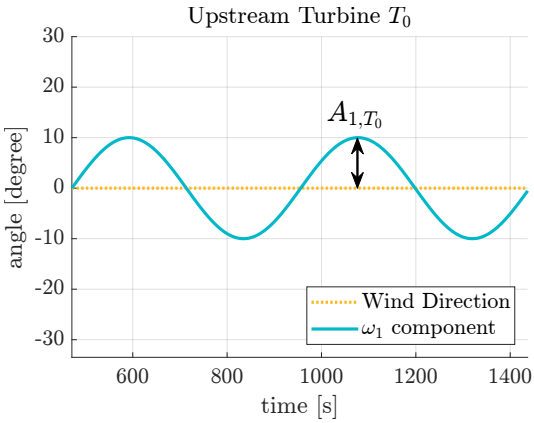

(b) The ω_1 component and the ω_3 component in the optimal control sequence of T_0 are plotted separately.

Figure 4-8: In (a), the optimal control sequence obtained from `fmincon` is re-plotted. Three parameters to be optimized are annotated: the fundamental frequency ω_1, the phase difference of the fundamental frequency component between the optimal control sequences of T_0 and T_1 $\Delta\phi_1$, and the amplitude of the optimal control sequence of T_1 A_{1,T_1}. In (b), the optimal control sequence of T_0 from (a) can be represented as the superposition of its ω_1 component and ω_3 component. Another two parameters to be optimized are annotated: the amplitude of the ω_1 component of T_0 A_{1,T_0}, and the amplitude of the ω_3 component of T_0 A_{3,T_0}.

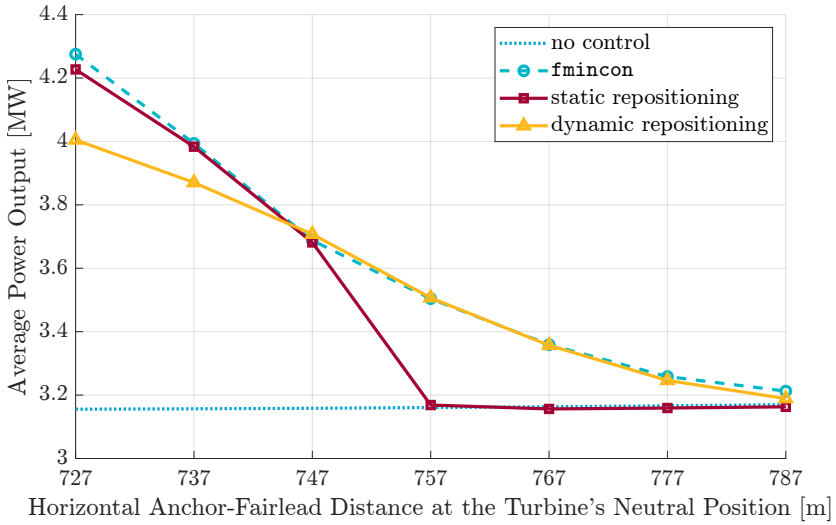

Figure 4-9: Comparison of optimized average power output results using `fmincon`, static repositioning grid search, and dynamic repositioning grid search. This figure illustrates that the results from `fmincon` reflect the superior power enhancement mode between static and dynamic repositioning. The dashed line at the bottom represents the no-control scenario for baseline comparison.

4-3 Analysis of Fundamental and Harmonic Components in Control Sequences

4-3-1 Fundamental Frequency Component

To identify the relationship between the fundamental frequency contained in the optimal control sequences and the floating wind turbine system, we now look into the floater model. Eq. (4-5) describes the floater model.

$$\begin{cases} m\ddot{p}_x = F_{\text{mooring},x}(p_x, p_y) - F_{\text{hydro},x}(v_x, v_y) + F_{\text{aero},x}(v_x, v_y, U_{\text{eff}}, \gamma) \\ m\ddot{p}_y = F_{\text{mooring},y}(p_x, p_y) - F_{\text{hydro},y}(v_x, v_y) + F_{\text{aero},y}(v_x, v_y, U_{\text{eff}}, \gamma) \end{cases} \tag{4-5}$$

where m stands for the summation of m_{turbine} the mass of the turbine and m_{added} the added mass.

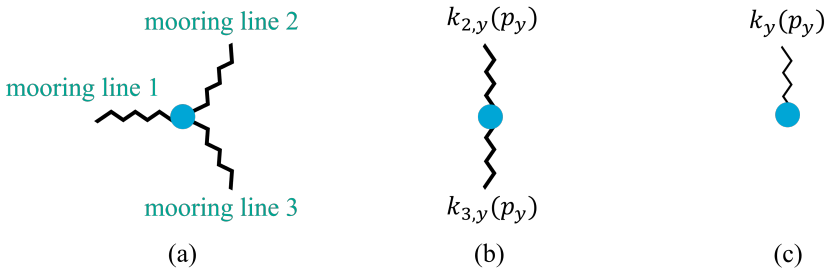

Figure 4-10: Illustration of the Floater Model: (a) 2D Model of the Floater, (b) Simplified Model Focusing on the Crosswind Direction, (c) Equivalent Simplified Model.

The mooring line force depends on the position of the floating turbine (p_x, p_y), essentially acting as a spring; the hydrodynamic drag force depends on the moving speed of the floating turbine (v_x, v_y), essentially acting as a damper; the aerodynamic thrust force depends on the moving speed of the floating turbine (v_x, v_y), the effective wind speed U_{eff} faced by the turbine, and the rotor yaw angle γ, essentially acting as an indirect input to the system, with the rotor yaw angle γ as the actual control input. Therefore, the entire system, connected by three mooring lines in a Y-shape as illustrated in Figure 4-10(a), is a nonlinear mass-spring-damper system. Furthermore, the system equations can be expanded and written as follows:

$$\begin{cases} m\ddot{p}_x = k_x(p_x)p_x - (c\sqrt{v_x^2 + v_y^2})v_x + F_{\text{aero},x}(v_x, v_y, U_{eff}, \gamma) \\ m\ddot{p}_y = k_y(p_y)p_y - (c\sqrt{v_x^2 + v_y^2})v_y + F_{\text{aero},y}(v_x, v_y, U_{eff}, \gamma) \end{cases} \tag{4-6}$$

where c represents all the relevant constants in the hydrodynamic drag force.

An intuitive explanation of $k_y(p_y)$ is provided here. Comparing the distance between the anchor of mooring line 1 and the neutral position (>700m) with the turbine's movement range in the y-direction (<40m), the effect of mooring line 1 on the turbine's movement in the y-direction can be considered negligible due to their difference being more than an order of magnitude. Therefore, the mooring line force acting on the turbine in the y-direction can be considered primarily from the y-components of the forces from mooring line 2 and mooring line 3. This means that, focusing solely on the y-direction movement, it can be regarded as the turbine being connected in series with two springs, one above with stiffness $k_{2,y}(p_y)$ and one below with stiffness $k_{3,y}(p_y)$, as illustrated in Figure 4-10(b). Further, the mooring lines can be simplified to an equivalent spring with stiffness $k_y(p_y)$, as illustrated in Figure 4-10(c).

To further simplify the system, we consider the movement range of the floating turbine. Taking the 767m case as an example, Figure 4-11 shows the position and velocity trajectories of the upstream turbine T_0 under the optimal control sequence as shown in Figure 4-4.

Firstly, it is observed that when the turbine is being dynamically repositioned, the position of the turbine in the x-direction remains almost constant at 45.5 m, i.e., $v_x \approx 0$ m/s. Therefore, for dynamic repositioning, (4-6) can be simplified to the following equation:

$$m\ddot{p}_y = k_y(p_y)p_y - c|v_y|v_y + F_{\text{aero},y}(v_y, U_{\text{eff}}, \gamma) \tag{4-7}$$

where the equivalent stiffness $k_y(p_y)$ is plotted in Figure 4-12.

Secondly, it is observed that v_y fluctuates around ± 0.5 m/s, which is negligible compared to the effective wind speed $U_{\text{eff}} = 8.2$ m/s experienced by an unwaked turbine. Therefore, for an unwaked floating wind turbine, the aerodynamic thrust term in (4-7) can be simplified to depend only on the rotor yaw angle γ, i.e., $F_{\text{aero},y}(\gamma)$.

Next, we examine the relationship between the rotor yaw angle and the aerodynamic thrust force, as shown in Figure 4-13. It can be observed that, although their relationship is not strictly linear, it can be approximated by a linear function. Therefore, the term $F_{\text{aero},y}(\gamma)$ can be approximated as $F_{\text{aero},y}(\gamma) \approx K_{\text{aero}}\gamma$. As a result, the dynamics of the floater during dynamic repositioning can be characterized by the following equation:

$$m\ddot{p}_y = k_y(p_y)p_y - c|\dot{p}_y|\dot{p}_y + K_{\text{aero}}\gamma \tag{4-8}$$

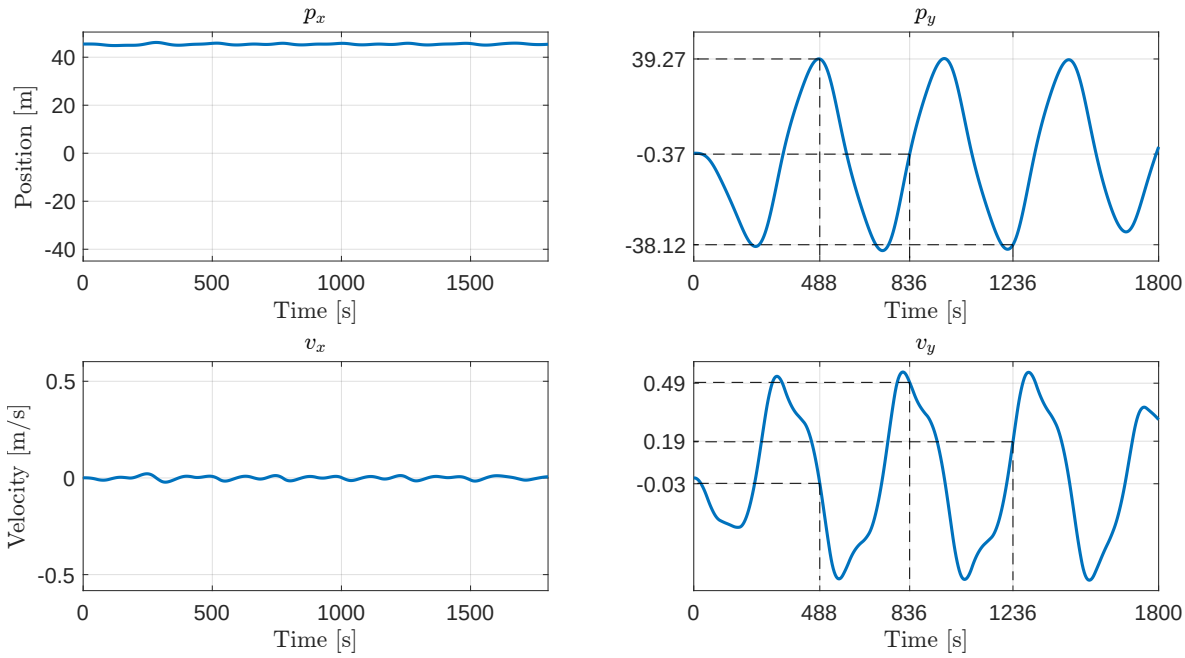

Figure 4-11: Optimized position and velocity trajectories of the upstream turbine T_0 for the 767 m case. It can be seen that the position in the downwind direction (x direction) remains almost constant at 45.5 m, while the velocity in the downwind direction is nearly 0 m/s. In contrast, the position and velocity in the crosswind direction (y direction) exhibit periodic variations.

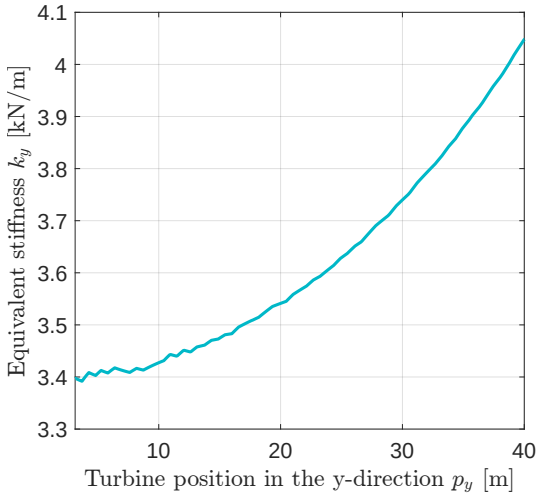

Figure 4-12: Relationship between turbine's position in the y-direction p_y and the equivalent stiffness k_y: the system exhibits large stiffness for large displacement in the y-direction.

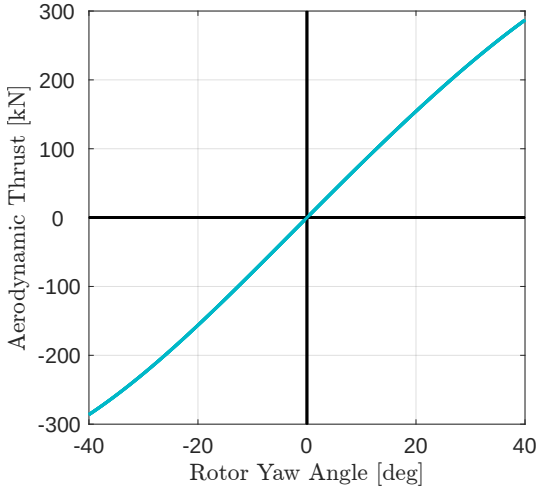

Figure 4-13: Relationship between rotor yaw angle and the aerodynamic thrust force in the y-direction: It can be seen that their relationship can be approximated by a linear function.

At this point, we can see that (4-8) is very close to the expression for a linear mass-spring-damper system, with the exception of two nonlinear components, $k_y(p_y)$ and $c|\dot{p}_y|$. The next step is to examine the degree of non-linearity of these two components by observing the frequency domain response of the linear model at different operating points.

From Figure 4-11, three typical operating points are selected:

	p_x	p_y	$\dot{p}_x$	$\dot{p}_y$
Operating Point 1	45.5	39.27	0	-0.03
Operating Point 2	45.5	-0.37	0	0.49
Operating Point 3	45.5	-38.12	0	0.19

Table 4-1: Selected operating points for linearization.

Operating Point 1 is selected as it corresponds to the maximum position in the y-direction. Operating Point 2 is chosen because it represents the maximum velocity in the y-direction. Operating Point 3 is chosen as it represents an intermediate velocity in the y-direction.

The Bode diagrams (from γ to p_y) of the linearized models at the selected operating points are shown in Figure 4-14a. Additionally, the two dominant frequencies ω_1 and ω_3 contained in the optimal control sequence for the upstream turbine T_0 rotor yaw angle are also marked. Similarly, the Bode diagrams (from γ to v_y) of the linearized models at the selected operating points are shown in Figure 4-14b.

Comparing the three sets of Bode diagrams in Figure 4-14a, it can be seen that the natural frequency of the ruby system is the lowest, the natural frequency of the yellow system is intermediate, and the natural frequency of the cyan system is the highest. This is because the ruby system operates around the point with the smallest displacement in the y-direction, resulting in the smallest equivalent stiffness k_y, as shown in Figure 4-12. Consequently, its natural frequency $\omega_n = \sqrt{k_y/m}$ is the lowest. In terms of the system damping, it is the opposite. The ruby system has the highest damping, the yellow system has intermediate damping, and the cyan system has the lowest damping. This is because the ruby system operates around the point with the highest velocity, resulting in the largest equivalent damping coefficient $c|\dot{p}_y|$.

Observing Figure 4-14, the non-linearity of the system during dynamic repositioning can be described by the area enveloped by the cyan Bode and the ruby Bode. Thus, from a macro perspective, despite the nonlinear components it contains, the system as a whole exhibits the characteristics of a linear mass-spring-damper system, with only slight differences in the mid-frequency range.

By comparing the fundamental frequency $\omega_1 = 0.0136\,\text{rad/s}$ extracted from the optimal control sequence with the frequency characteristics of this quasi-linear mass-spring-damper system, it can be observed that ω_1 is close to but slightly lower than the system's natural frequency. This explains why the optimal control sequence provided by `fmincon` contains this frequency component: the optimizer identified this characteristic frequency of the floater's dynamics and exploited it to provide the maximum total power output for the wind farm.

For those interested, the same procedure was applied to other mooring line stiffness settings, and the resultant Bode diagrams can be found in Appendix Section A-2.

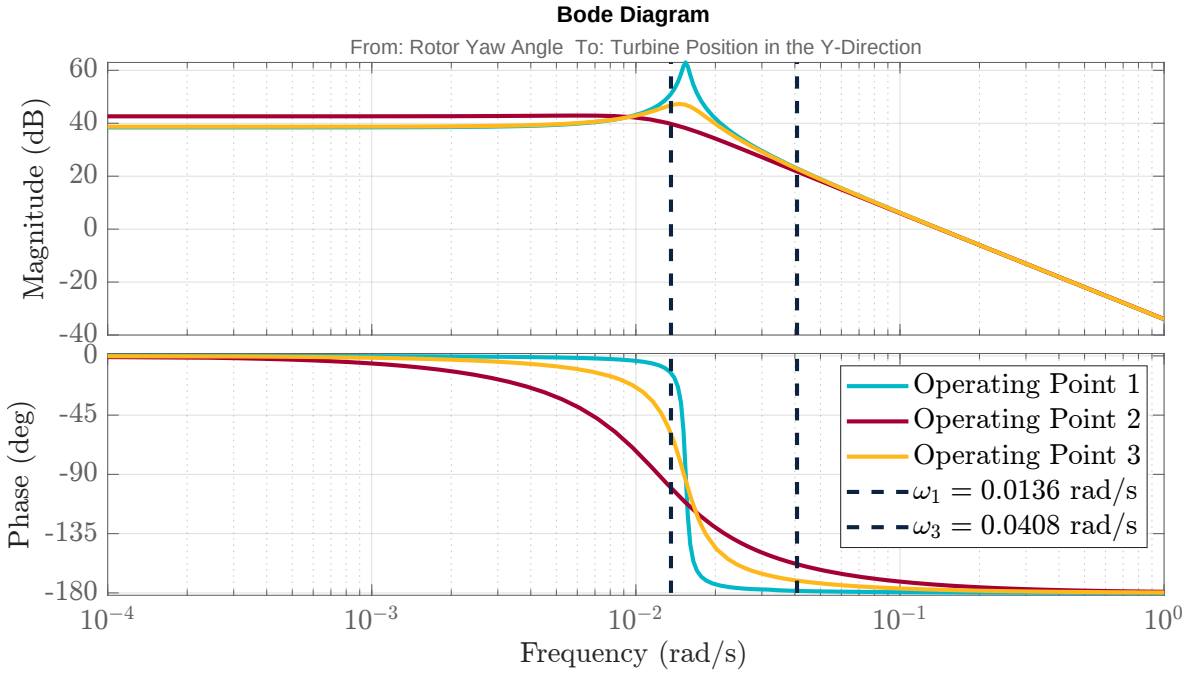

(a) from γ to p_y

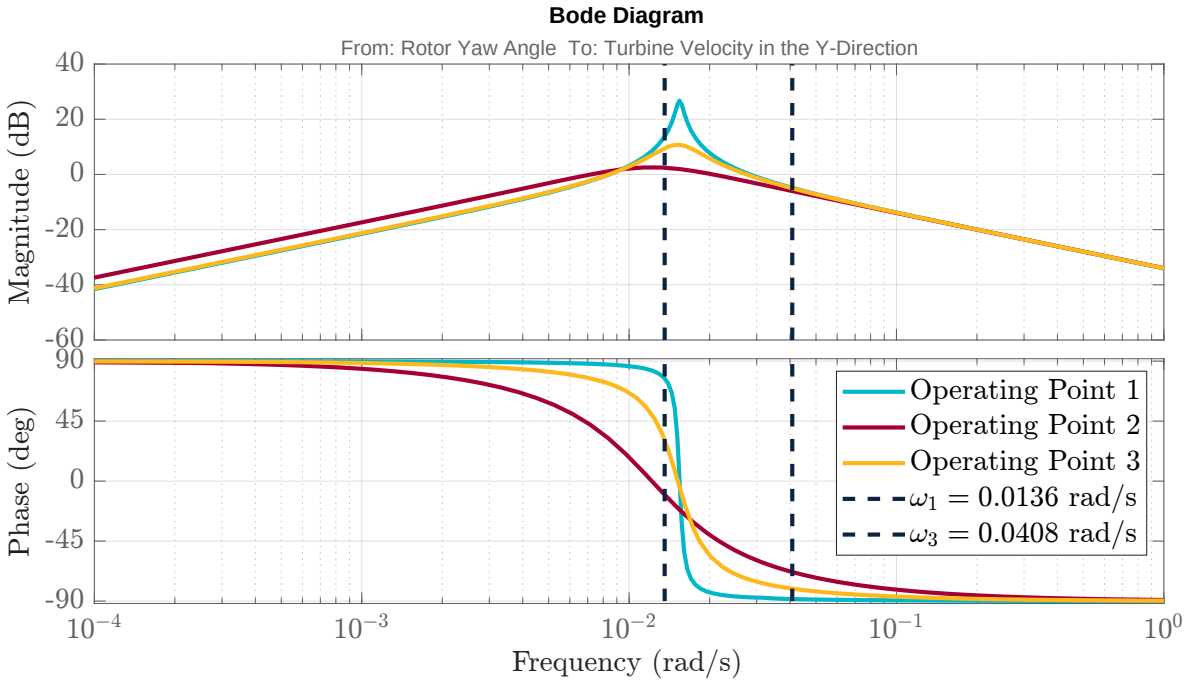

(b) from γ to v_y

Figure 4-14: Bode diagrams of the linearized model at the chosen three operating points for the 767 m case. The two dominating frequencies from the optimized control sequence are overlaid, indicated by vertical dashed lines at $\omega_1 = 0.0136$ rad/s and $\omega_3 = 0.0408$ rad/s.

Next, an explanation will be provided from two perspectives to elucidate why a fundamental frequency close to the system's natural frequency can lead to a decent energy production gain for the wind farm.

- From the perspective of the turbine's displacement in the y-direction, we aim to achieve the largest possible displacement using rotor yaw misalignment. Based on this motivation, observing Figure 4-14a, if the control signal for the rotor yaw angle contains a frequency close to the system's natural frequency, it can fully exploit the system's characteristics. This allows for significant displacement in the y-direction with a relatively small rotor yaw misalignment.
- Due to the inherent nature of dynamic repositioning, which forces the upstream wake to periodically sweep across the downstream rotor, we aim to minimize the overlapping duration. Since the movement of the upstream wake at the downstream turbine is caused by the movement of the upstream turbine, we focus on the effect of the rotor yaw angle on the speed of the upstream turbine. Observing Figure 4-14b, it is evident that only when the control signal includes a frequency close to the system's natural frequency can the turbine's speed be effectively amplified, allowing the upstream wake to quickly sweep across the downstream rotor.

Here, we provide additional details regarding the search range for ω_1 set in Section 4-2-2. Utilizing the fact that the optimal fundamental frequency ω_1^* is close to the natural frequency of the floater's dynamics in the crosswind direction ω_n, the search range for ω_1^* can be based on the estimated ω_n. For the 767m case, from Figure 4-12, the equivalent stiffness k_y in the y-direction is taken as 4000 N/m. Using $m = m_{\text{turbine}} + m_{\text{added}} = 22,800,000\,\text{kg}$, we can then determine that the optimal fundamental frequency ω_1^* is near $\omega_n = \sqrt{k_y/m} = \sqrt{4000/22800000} \approx 0.0132\,\text{rad/s}$.

In summary, under dynamic repositioning, the floater's dynamics exhibit the characteristics of a quasi-linear mass-spring-damper system. The fundamental frequency in the optimal control signal is close to the natural frequency of this quasi-linear mass-spring-damper system.

4-3-2 Third Harmonic Component

In Figure 4-14a, it can be observed that the third harmonic ω_3, falls within the high-frequency range of the system. This indicates that the influence of the ω_3 component on the turbine's y-direction position is attenuated by the system. It can be observed that the system's gain for ω_1 is approximately 40 dB, whereas that for ω_3 is 20 dB, indicating a tenfold relationship when converted back to the original dimensions. This suggests that the role of ω_3 is not strongly related to turbine repositioning.

Since changing the rotor yaw angle either alters the turbine position or steers the wake within the scope of this study, it infers that the third harmonic component ω_3 is involved in wake steering. To validate this hypothesis, we conduct a quantitative study of the impact of the third harmonic and present a visual demonstration.

By plugging the optimized six parameters into (4-3), the control input signal for the upstream turbine contains both the fundamental and third harmonic components. If the two parameters related to the third harmonic component, $\Delta\phi_3$ and A_{3,T_0}, are artificially set to zero, the upstream turbine will receive a control input signal containing only the fundamental component. This approach allows us to visually examine the influence of the two control input signals on the turbine's position in the y-direction. Applying these two control sequences to the system, the y-direction position trajectories of the upstream turbine are shown in Figure 4-15a. The results indicate that the turbine position trajectories are nearly identical regardless of the presence of the third harmonic, suggesting that the third harmonic component indeed does not contribute to turbine repositioning.

By examining the shape of the observation point chain of the upstream turbine in Figure 4-15b, we notice a higher frequency serpentine shape compared to the observation point chain of the upstream wake in Figure 4-15c. Therefore, we can conclude that the purpose of the third harmonic component in the control signal of the upstream turbine is to achieve wake steering.

4-4 Summary

The primary objective of this chapter was to investigate the enhancement in overall wind farm energy production through static and dynamic repositioning under constant wind conditions, considering different levels of mooring line tightness. Our analysis revealed that:

1. The static repositioning control mode is suitable for slack mooring line settings. When the system stiffness is low, a sufficient movable range is provided to the turbines, enabling the static repositioning mode to effectively enhance the wind farm power output. Compared to the baseline case, this enhancement can numerically reach up to 36%. However, as the system stiffness increases, the reduced movable range significantly diminishes the effectiveness of static repositioning.

2. The dynamic repositioning control mode becomes more effective than static repositioning for relatively tight mooring line settings. When the high stiffness of the system results in a limited movable range for the turbines, the turbines can periodically move

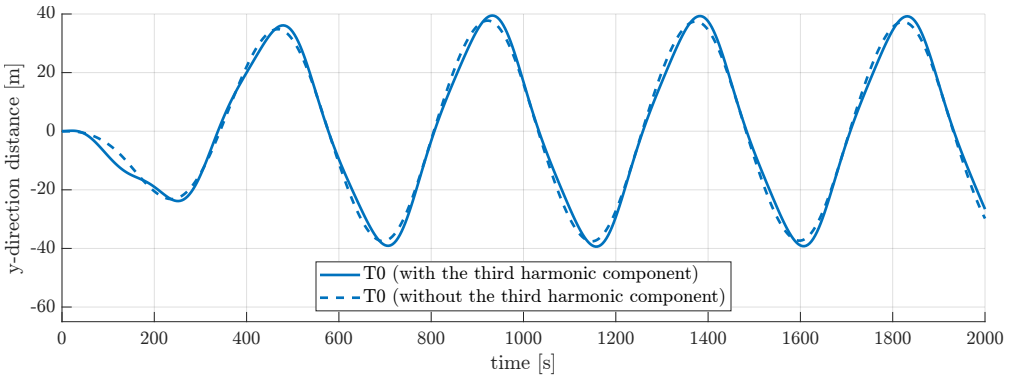

(a) The y-direction trajectories of the upstream turbine for two rotor yaw angle sequences are shown: one with the third harmonic component included (solid), and one without (dashed).

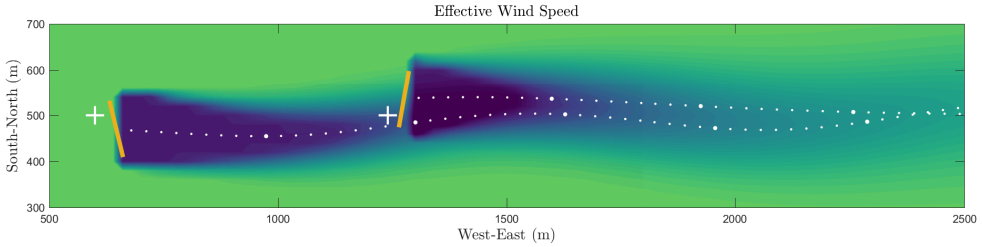

(b) Upstream Wake Meandering: Control Sequence with the Third Harmonic Included

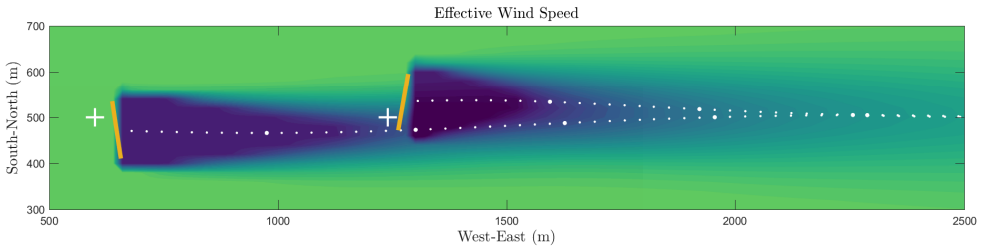

(c) Upstream Wake No Meandering: Control Sequence without the Third Harmonic

Figure 4-15: These figures illustrate the effect of the third harmonic component in the control input sequence of the upstream turbine, highlighting its role in creating high-frequency wake meandering. In (a), it can be observed that the third harmonic component has a negligible effect on the turbine's y-direction position, indicating that the effectiveness of this harmonic component is not related to turbine repositioning. Comparing the observation point chains of the upstream turbine in (b) and (c), it is evident that when the control signal includes the third harmonic component, the wake exhibits higher frequency meandering.

in the crosswind direction. This movement intermittently brings higher wind speeds to the downstream turbines, resulting in a higher power output.

3. Under dynamic repositioning control, the optimal control signals exhibit a sinusoidal form. The control signal for the upstream turbine includes a fundamental frequency component and a third harmonic component, while the control signal for the downstream turbine includes only the fundamental component. The optimal fundamental frequency is directly related to the system stiffness. For each level of mooring line tightness, the optimal fundamental frequency exploits the frequency domain characteristics of the floater's dynamics in the y-direction. This ensures that the upstream wake sweeps past the downstream wake as quickly as possible, while maximizing the time the downstream turbine is exposed to higher wind speeds.

Secondly, during the analysis of dynamic repositioning, an optimization method based on block coordinate descent and grid search was employed. Six parameters, used to describe the optimal control sequence for dynamic repositioning, were selected and sequentially optimized two by two. This optimization approach has three advantages: first, the optimal control sequence is presented in an analytical form with respect to time; second, it requires few iterations, as studies show that a single iteration can bring the optimized parameters close to their optima; third, it is extensible—if more details of the control input signals, such as additional frequency components or a DC component, need to be covered, new parameters can simply be appended to the optimization procedure at each iteration.

Lastly, we provide an outlook on the reference value of this study on dynamic repositioning. From the perspective of investors, the structural load and stability of the turbine always come first before turbine repositioning. Therefore, during the design of floating wind turbines, load analysis and stability analysis are performed first to provide constraints on the profile of the mooring system, such as limitations on mooring line length, material choice, and seabed anchor positions.

Two scenarios may arise under these constraints. In the first scenario, the constraints result in a fixed profile for the mooring system, with no flexibility in terms of length, material, or anchor points to ensure reasonable structural load and stability. In this case, the analysis performed in this chapter can be applied to evaluate the effectiveness and feasible control methods of turbine repositioning under this fixed design, providing valuable reference for power generation companies.

In the second scenario, the constraints still allow for some flexibility in the design of the mooring system profile, such as a range of permissible mooring line lengths or anchor points. Here, the analysis in this chapter can be performed to further narrow down the design choices for the mooring system profile, providing useful guidance for floating turbine manufacturers.

Chapter 5

Conclusion

5-1 Summary of the Key Findings

This study aimed to maximize the energy production of a two-turbine wind farm over a period of time by exploring and analyzing how the floating wind turbines should be repositioned under constant wind conditions. This study found that a floating wind farm can operate under two working modes: static repositioning and dynamic repositioning. When the mooring lines are relatively slack, static repositioning yields higher energy production gains. Conversely, when the mooring lines are relatively tight, dynamic repositioning provides superior energy production gains. A summary of these two modes is stated as follows:

- **Static Repositioning:** In this mode, the rotor yaw angles of the upstream and downstream turbines are maintained at constant values with opposite signs, respectively, in steady state. This results in the turbines being statically repositioned on opposite sides of the crosswind direction. For relatively slack mooring line settings, a small rotor yaw misalignment of the floating turbines can result in sufficient displacement in the crosswind direction. This effectively reduces the overlap of the wake of the upstream turbine with the downstream rotor. From the perspective of individual energy production, this approach results in a small sacrifice in the upstream turbine's power output to achieve a significant increase in the downstream turbine's power output, thereby enhancing the overall energy production of the wind farm. However, for relatively tight mooring line settings, the movable range of the turbines is restricted; thus, the rotor yaw misalignment of the floating turbines does not result in significant displacement in the crosswind direction. Consequently, the effectiveness of the static repositioning mode is noticeably reduced under tight mooring line settings.
- **Dynamic Repositioning:** In this mode, the rotor yaw angles of the upstream and downstream turbines vary in a sinusoidal manner, resulting in the turbines being dynamically repositioned in the crosswind direction. The fundamental difference from static repositioning is that in dynamic repositioning, the turbines are continuously moving

rather than being relocated to fixed new positions. This continuous motion allows the turbines to travel further in the crosswind direction. As a result, the downstream turbine can periodically experience higher wind speeds, thereby increasing the overall energy production of the wind farm. Floating wind farms with tight mooring line settings can utilize this characteristic to achieve some energy production gains. However, for wind farms with relatively slack mooring line settings, the energy production gains from dynamic repositioning cannot surpass that of static repositioning. This is because dynamic repositioning inherently forces the upstream wake to periodically sweep over the downstream rotor, which cannot be better than the case where the upstream wake never needs to sweep over the downstream rotor.

Further, this study also explored the main characteristics of the optimal control sequences for the rotor yaw angles of both the upstream and downstream turbines under dynamic repositioning in the frequency domain. The study reveals that the optimal control sequence of the rotor yaw angle for the upstream turbine consists of a fundamental component u_{1,T_0} and its third harmonic component u_{3,T_0}, while the optimal control sequence for the downstream turbine's rotor yaw angle consists solely of a fundamental component u_{1,T_1}. The fundamental components u_{1,T_0} and u_{1,T_1} share the same frequency ω_1, but there is a phase difference $\Delta\phi_1$ between them. Below, we summarize the study findings from the aspects of the fundamental phase difference $\Delta\phi_1$, the fundamental components u_{1,T_0} and u_{1,T_1}, and the third harmonic component u_{3,T_0}.

- **The Fundamental Phase Difference $\Delta\phi_1$:** This parameter is responsible for coordinating the motions of the upstream and downstream turbines. It ensures that when the upstream wake sweeps to one side of the crosswind direction, the downstream turbine moves to the opposite side of the crosswind direction, minimizing the overlapping duration.
- **The Fundamental Components u_{1,T_0} and u_{1,T_1}:** These two control signals cause the turbines to move back and forth in the crosswind direction in a sinusoidal manner. According to this study, the optimal value of their frequency ω_1 is located close to, but slightly smaller than, the natural frequency of the linearized floater model which takes the rotor yaw angle as input and the crosswind direction position as output.
- **The Third Harmonic Component u_{3,T_0}:** This control signal exists only in the control signal for the upstream turbine. Due to the frequency domain characteristics of the floater, its contribution is not in repositioning the turbine. Instead, it steers the wake, further reducing the duration that the upstream wake sweeps over the downstream rotor.

Finally, for dynamic repositioning, based on the aforementioned extracted frequency-domain parameters, a new approach to finding the optimal control sequences for dynamic repositioning is proposed. The proposed optimization method combines block coordinate descent with grid search. A major advantage of this method is that it can provide an analytical expression for the optimal control sequences. Additionally, experiments show that the first iteration of this optimization method can bring the parameters close to their optimal values, demonstrating the potential for faster optimization times compared to time-domain optimization using `fmincon`.

5-2 Limitations and Considerations

- The mooring line model used in this study is a static model subject only to turbine position. Although it captures the spring-like behavior of the mooring line, it does not consider the forces exerted by seawater on the mooring line. To achieve higher model accuracy, future research should incorporate a dynamic mooring line model. However, incorporating a dynamic mooring line model may increase computational complexity, potentially hindering the feasibility of real-time optimization. Therefore, future studies should also consider the trade-off between incorporating more dynamics and managing computational costs.
- The floating wind farm model used in this study requires further validation through comparison with high-fidelity floating wind farm models or field experimental data. The integration of floater dynamics and FLORIDyn in this study is based on the assumption that new turbine positions do not affect the positions of existing observation points (OPs). The validity of this assumption needs to be justified through comparison with high-fidelity CFD models. Therefore, this aspect of the work should be addressed in future research.
- The floating turbine stabilization task is not included in this study. This research treats turbine stabilization and turbine repositioning as two separate objectives. However, in reality, the actuators driving turbine repositioning are also used for turbine stabilization. Therefore, a future research task is to study the impact of control signals used for turbine repositioning on turbine stabilization.
- This study considers the effectiveness of turbine repositioning from a macroscopic perspective based solely on turbine positions. However, it does not account for the impact of turbine movement on the fatigue of turbine components and mooring line loads. Since mechanical fatigue affects the lifespan of the turbines and indirectly influences the cost of electricity generation, future research should incorporate the effects of fatigue into the objective function to ensure closer alignment with practical applications.

5-3 Future Directions and Outlook

Based on the limitations discussed in the previous section, this section outlines future directions in the following three areas:

- **Floating Wind Farm Model:** Firstly, the current dynamic floating wind farm model should be validated using data from either CFD or field experiments. If the accuracy is found to be lacking, the modules within the model should be updated accordingly. Secondly, as this study shows that the primary source of increased simulation time is the nonlinear floater dynamics, and the optimal control sequence for dynamic repositioning is largely related to only the linearized model near the neutral position, another future research direction is to develop a linearized floating wind farm model for real-time control. Lastly, the floating wind farm model can be extended from 2D to 3D to incorporate more wake mitigation strategies, such as rotor tilting.

- **Optimization Framework:** The objective function of this study focuses on maximizing accumulated energy production but does not consider turbine stabilization or mechanical fatigue, which are factors that influence the cost of energy generation. Therefore, to better align with future practical applications, a multi-objective optimization function should be established. This function should aim to reduce the cost of electricity generation, rather than solely maximizing energy production.
- **Wind Farm Setup:** In future research, more complex and general floating wind farm layouts should be studied. Furthermore, the wind field experienced by the floating wind farm should be extended from constant wind conditions to time-varying conditions. Lastly, the water settings should transition from still water to conditions that include waves.

Appendix A

A-1 Magnitude and Phase Spectra of Optimal Control Sequences Under Various Mooring Line Stiffness Settings

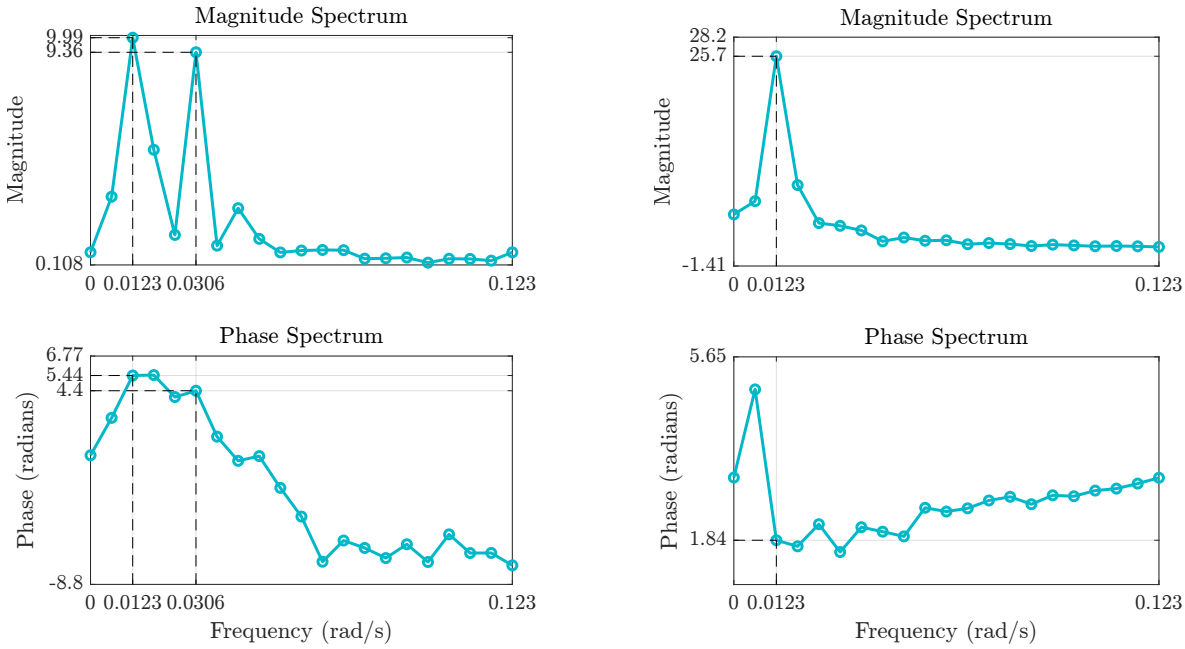

(a) Upstream Turbine T_0 **(b)** Downstream Turbine T_1

Figure A-1: The magnitude and phase spectra of the optimal control sequences (757 m)

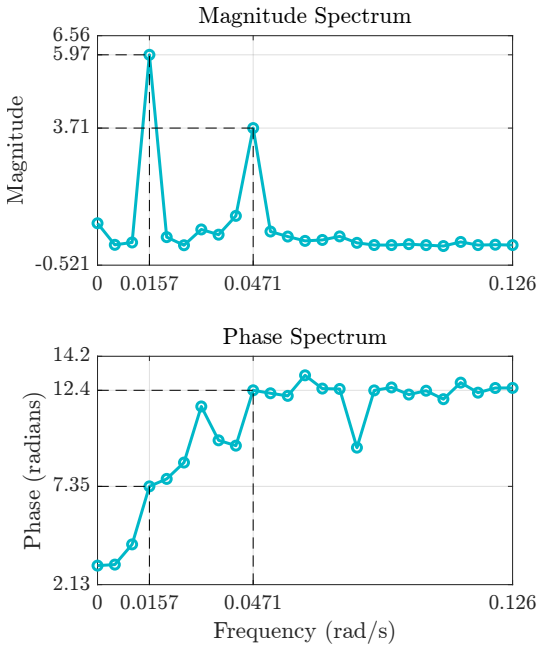

(a) Upstream Turbine T_0

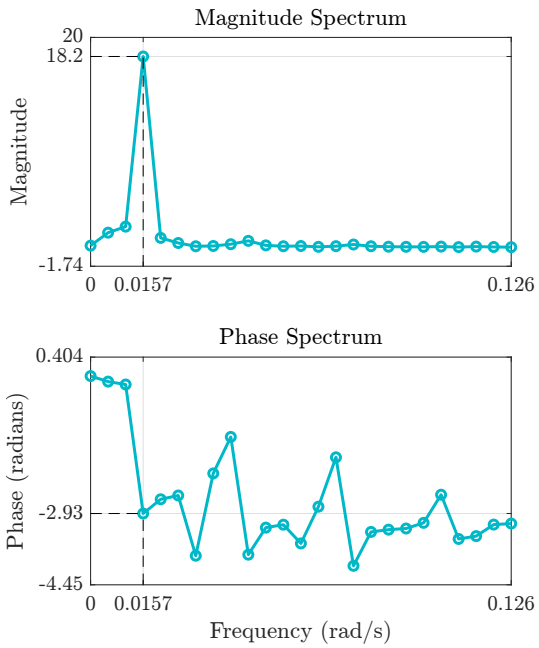

(b) Downstream Turbine T_1

Figure A-2: The magnitude and phase spectra of the optimal control sequences (777 m)

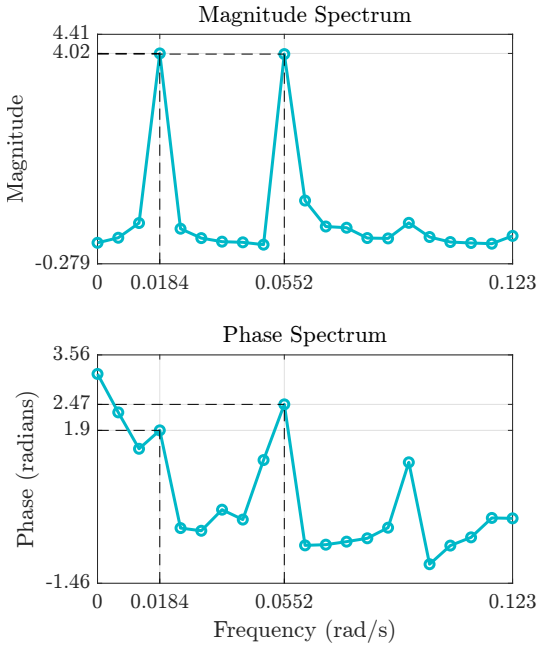

(a) Upstream Turbine T_0

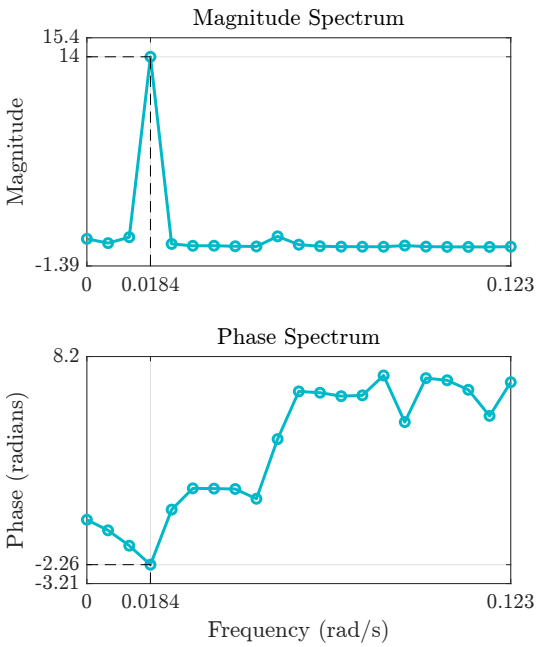

(b) Downstream Turbine T_1

Figure A-3: The magnitude and phase spectra of the optimal control sequences (787 m)

A-2 Bode Diagrams of Linearized Models at Different Operating Points Under Various Mooring Line Stiffness Settings

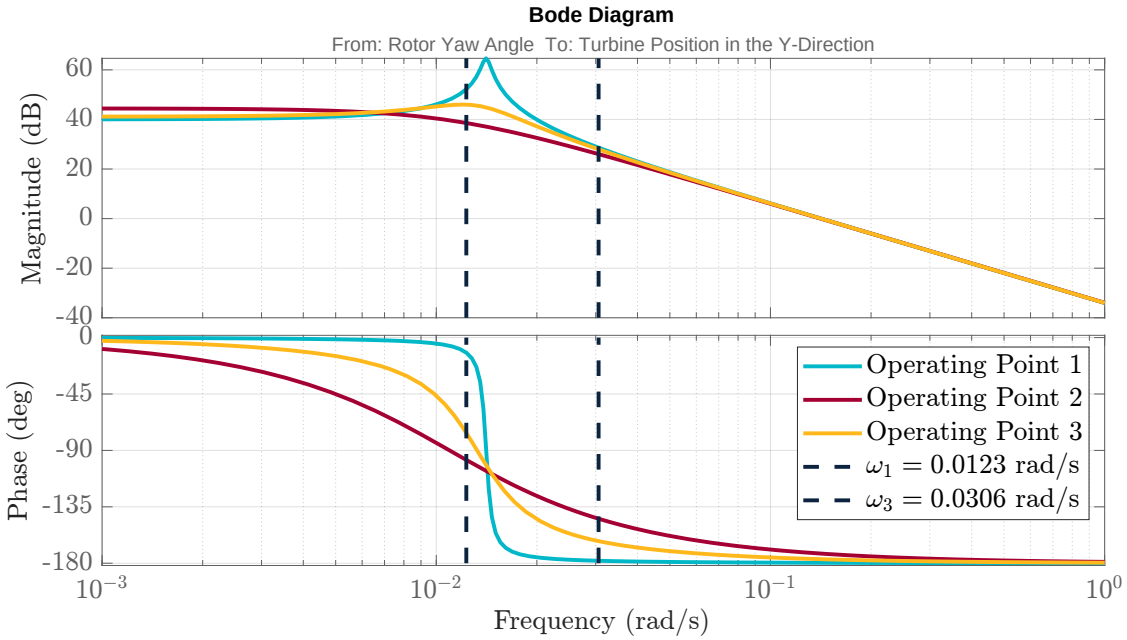

(a) from γ to p_y

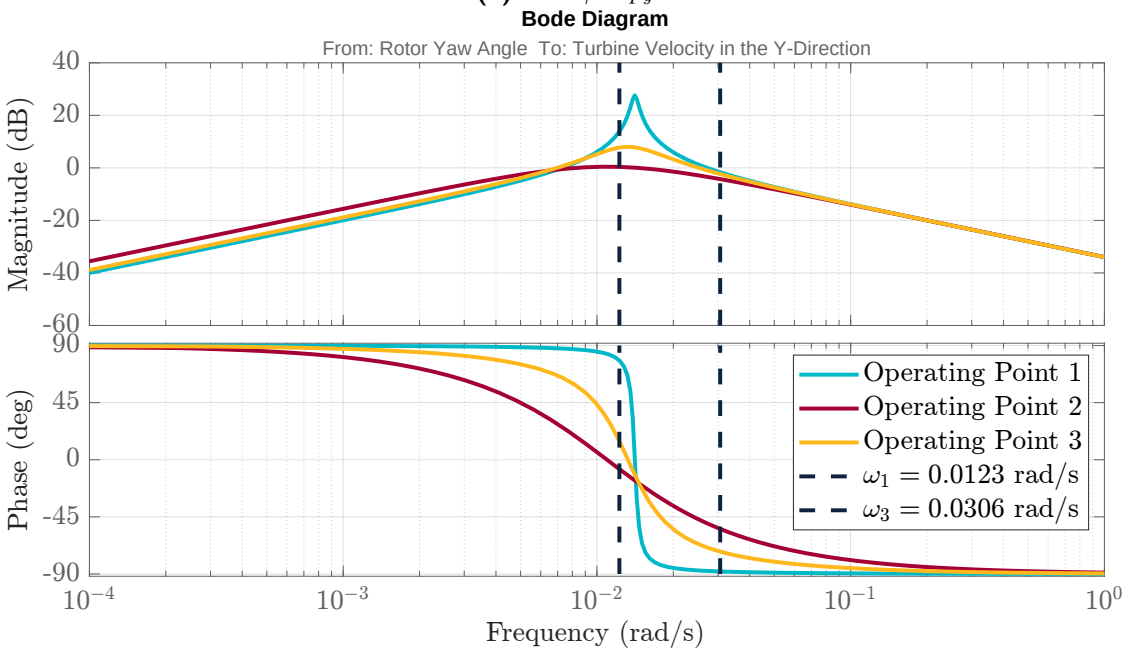

(b) from γ to v_y

Figure A-4: Bode diagrams of the linearized model at the chosen three operating points for the 757 m case. The two dominating frequencies from the optimized control sequence are overlaid, indicated by vertical dashed lines at $\omega_1 = 0.0123$ rad/s and $\omega_3 = 0.0306$ rad/s.

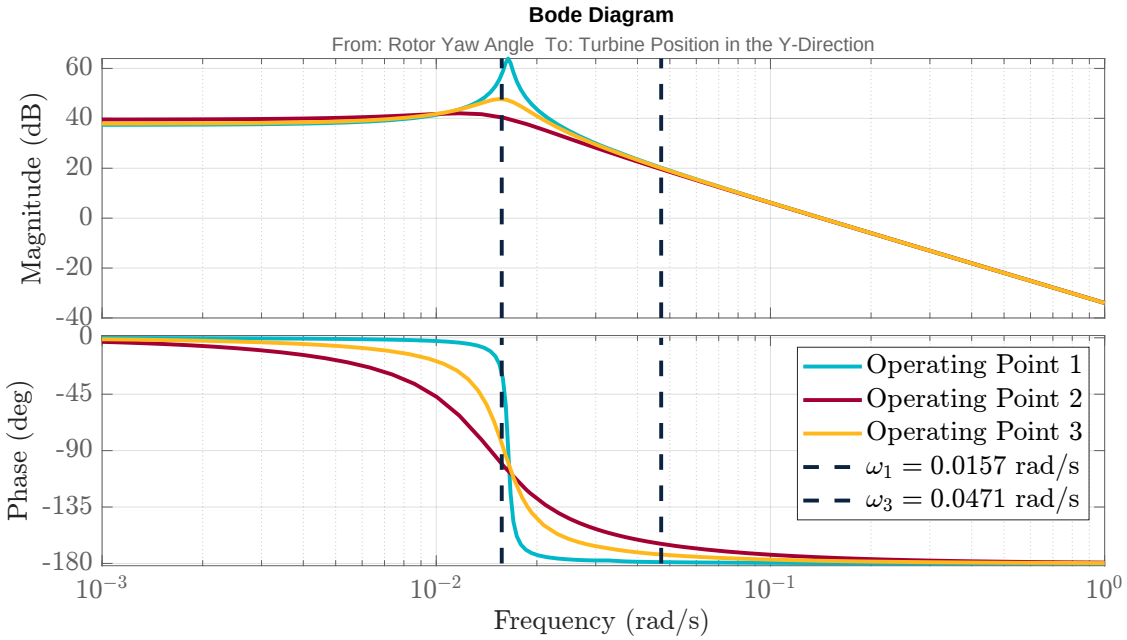

(a) from γ to p_y

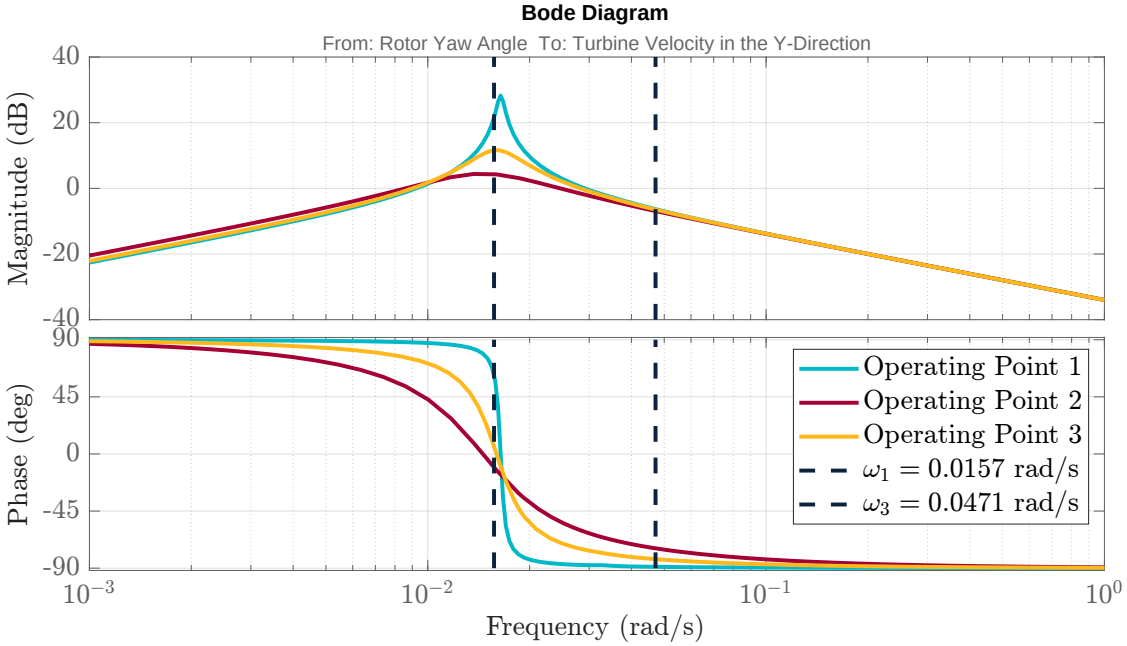

(b) from γ to v_y

Figure A-5: Bode diagrams of the linearized model at the chosen three operating points for the 777 m case. The two dominating frequencies from the optimized control sequence are overlaid, indicated by vertical dashed lines at $\omega_1 = 0.0157$ rad/s and $\omega_3 = 0.0471$ rad/s.

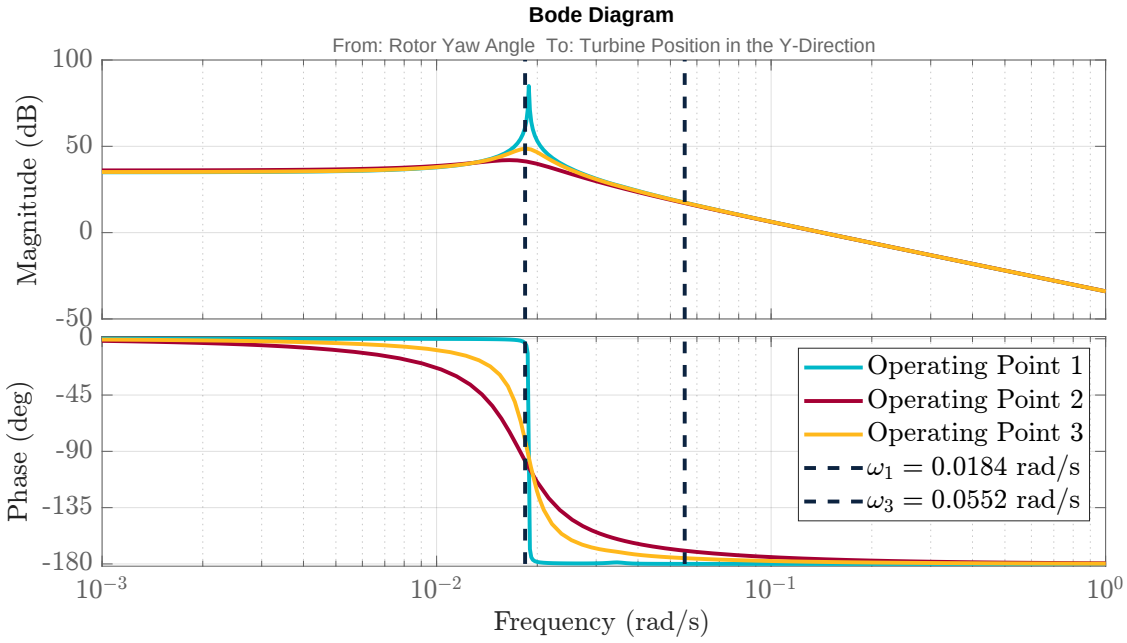

(a) from γ to p_y

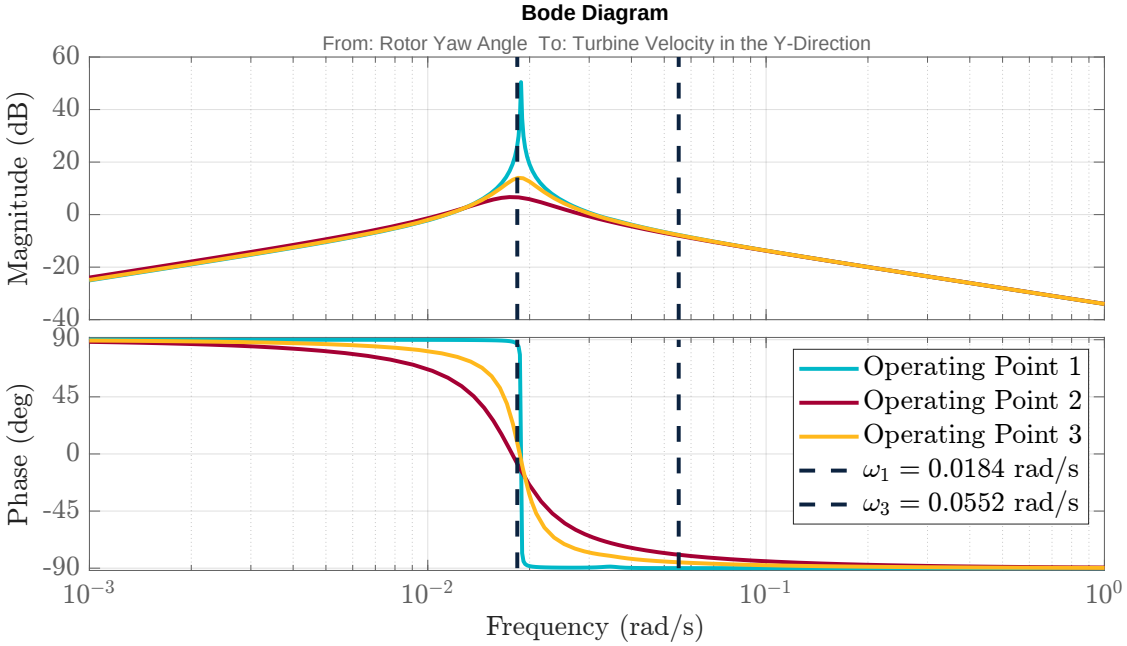

(b) from γ to v_y

Figure A-6: Bode diagrams of the linearized model at the chosen three operating points for the 787 m case. The two dominating frequencies from the optimized control sequence are overlaid, indicated by vertical dashed lines at $\omega_1 = 0.0184$ rad/s and $\omega_3 = 0.0552$ rad/s.

Bibliography

[1] M.S. Adaramola and P.-Å. Krogstad. Experimental investigation of wake effects on wind turbine performance. *Renewable Energy*, 36(8):2078–2086, 2011.

[2] Adesoji Adelaja, Charles McKeown, Benjamin Calnin, and Yohannes Hailu. Assessing offshore wind potential. *Energy Policy*, 42:191–200, 2012.

[3] Yuksel R Alkarem, Kimberly Huguenard, Amrit S Verma, Diederik Van Binsbergen, Erin Bachynski-Polić, and Amir R Nejad. Passive mooring-based turbine repositioning technique for wake steering in floating offshore wind farms. In *Journal of Physics: Conference Series*, volume 2767, page 092056. IOP Publishing, 2024.

[4] Jennifer Annoni, Pieter M. O. Gebraad, Andrew K. Scholbrock, Paul A. Fleming, and Jan-Willem van Wingerden. Analysis of axial-induction-based wind plant control using an engineering and a high-order wind plant model. *Wind Energy*, 19(6):1135–1150, 2016.

[5] Raj Kiran Balakrishnan and Sung-ho Hur. Maximization of the power production of an offshore wind farm. *Applied Sciences*, 12(8), 2022.

[6] R. J. Barthelmie, K. Hansen, S. T. Frandsen, O. Rathmann, J. G. Schepers, W. Schlez, J. Phillips, K. Rados, A. Zervos, E. S. Politis, and P. K. Chaviaropoulos. Modelling and measuring flow and wind turbine wakes in large wind farms offshore. *Wind Energy*, 12(5):431–444, 2009.

[7] R. J. Barthelmie and L. E. Jensen. Evaluation of wind farm efficiency and wind turbine wakes at the nysted offshore wind farm. *Wind Energy*, 13(6):573–586, 2010.

[8] R. J. Barthelmie, S. C. Pryor, S. T. Frandsen, K. S. Hansen, J. G. Schepers, K. Rados, W. Schlez, A. Neubert, L. E. Jensen, and S. Neckelmann. Quantifying the impact of wind turbine wakes on power output at offshore wind farms. *Journal of Atmospheric and Oceanic Technology*, 27(8):1302 – 1317, 2010.

[9] Jan Bartl and Lars Sætran. Experimental testing of axial induction based control strategies for wake control and wind farm optimization. In *Journal of Physics: Conference Series*, volume 753, page 032035. IOP Publishing, 2016.

[10] Majid Bastankhah and Fernando Porté-Agel. Experimental and theoretical study of wind turbine wakes in yawed conditions. *Journal of Fluid Mechanics*, 806:506–541, 2016.

[11] Majid Bastankhah and Fernando Porté-Agel. Wind farm power optimization via yaw angle control: A wind tunnel study. *Journal of Renewable and Sustainable Energy*, 11(2):023301, 03 2019.

[12] M Becker, D Allaerts, and JW Van Wingerden. Floridyn-a dynamic and flexible framework for real-time wind farm control. In *Journal of Physics: Conference Series*, volume 2265, page 032103. IOP Publishing, 2022.

[13] M. Becker, B. Ritter, B. Doekemeijer, D. van der Hoek, U. Konigorski, D. Allaerts, and J.-W. van Wingerden. The revised floridyn model: implementation of heterogeneous flow and the gaussian wake. *Wind Energy Science*, 7(6):2163–2179, 2022.

[14] Mehmet Bilgili, Abdulkadir Yasar, and Erdogan Simsek. Offshore wind power development in europe and its comparison with onshore counterpart. *Renewable and Sustainable Energy Reviews*, 15(2):905–915, 2011.

[15] Maria Isabel Blanco and Glória Rodrigues. Can the future eu ets support wind energy investments? *Energy Policy*, 36(4):1509–1520, 2008.

[16] María Isabel Blanco. The economics of wind energy. *Renewable and Sustainable Energy Reviews*, 13(6):1372–1382, 2009.

[17] S. Boersma, B. Doekemeijer, M. Vali, J. Meyers, and J.-W. van Wingerden. A control-oriented dynamic wind farm model: Wfsim. *Wind Energy Science*, 3(1):75–95, 2018.

[18] Sjoerd Boersma, Bart M Doekemeijer, Pieter MO Gebraad, Paul A Fleming, Jennifer Annoni, Andrew K Scholbrock, Joeri Alexis Frederik, and Jan-Willem van Wingerden. A tutorial on control-oriented modeling and control of wind farms. In *2017 American control conference (ACC)*, pages 1–18. IEEE, 2017.

[19] Tony Burton, Nick Jenkins, David Sharpe, and Ervin Bossanyi. *Wind energy handbook*. John Wiley & Sons, 2011.

[20] Filippo Campagnolo, Lejla Imširović, Robert Braunbehrens, and Carlo L Bottasso. Further calibration and validation of floris with wind tunnel data. In *Journal of Physics: Conference Series*, volume 2265, page 022019. IOP Publishing, 2022.

[21] Vincenzo Ceriello. Wake effect mitigation of floating offshore wind farms: Combining layout optimization, turbine repositioning and yaw-based wake redirection. 2023.

[22] R. Chitteth Ramachandran, C. Desmond, F. Judge, J.-J. Serraris, and J. Murphy. Floating wind turbines: marine operations challenges and opportunities. *Wind Energy Science*, 7(2):903–924, 2022.

[23] M Churchfield and S Lee. Nwtc design codes-sowfa. *URL: http://wind. nrel. gov/designcodes/simulator s/SOWFA*, 2012.

[24] Zamiyad Dar, Koushik Kar, Onkar Sahni, and Joe H. Chow. Windfarm power optimization using yaw angle control. *IEEE Transactions on Sustainable Energy*, 8(1):104–116, 2017.

[25] Belachew Desalegn, Desta Gebeyehu, Bimrew Tamrat, Tassew Tadiwose, and Ababa Lata. Onshore versus offshore wind power trends and recent study practices in modeling of wind turbines' life-cycle impact assessments. *Cleaner Engineering and Technology*, 17:100691, 2023.

[26] Michael Durstewitz and Martin Hoppe-Kilpper. Wind energy experience curve from the german '250 mw wind'-programme. In *IEA International Workshop on Experience Curves for Policy Making-the case of energy technologies*, pages 10–11, 1999.

[27] Equinor. Hywind Tampen: the world's first renewable power for offshore oil and gas. Online, 2023. Accessed: 2023-11-19.

[28] Eduardo Eribert Escobar Aquino and Ryozo Nagamune. H∞ position transfer and regulation for floating offshore wind turbines. *Control Theory and Technology*, 18:231–245, 2020.

[29] Timm Faulwasser, Milan Korda, Colin N. Jones, and Dominique Bonvin. On turnpike and dissipativity properties of continuous-time optimal control problems. *Automatica*, 81:297–304, 2017.

[30] Paul Fleming, Pieter M.O. Gebraad, Sang Lee, Jan-Willem van Wingerden, Kathryn Johnson, Matt Churchfield, John Michalakes, Philippe Spalart, and Patrick Moriarty. Simulation comparison of wake mitigation control strategies for a two-turbine case. *Wind Energy*, 18(12):2135–2143, 2015.

[31] Sten Frandsen and Morten L. Thøgersen. Integrated fatigue loading for wind turbines in wind farms by combining ambient turbulence and wakes. *Wind Engineering*, 23(6):327–339, 1999.

[32] Bohumil Frantál, Marina Frolova, and Javier Liñán-Chacón. Conceptualizing the patterns of land use conflicts in wind energy development: Towards a typology and implications for practice. *Energy Research & Social Science*, 95:102907, 2023.

[33] Yuan Gao, Aravindh Padmanabhan, Ouyang Chen, Ali C. Kheirabadi, and Ryozo Nagamune. A baseline repositioning controller for a floating offshore wind farm. In *2022 American Control Conference (ACC)*, pages 4224–4229, 2022.

[34] P. M. O. Gebraad, F. W. Teeuwisse, J. W. van Wingerden, P. A. Fleming, S. D. Ruben, J. R. Marden, and L. Y. Pao. Wind plant power optimization through yaw control using a parametric model for wake effects—a cfd simulation study. *Wind Energy*, 19(1):95–114, 2016.

[35] P. M. O. Gebraad, F. W. Teeuwisse, J. W. van Wingerden, Paul A. Fleming, S. D. Ruben, J. R. Marden, and L. Y. Pao. Wind plant power optimization through yaw

control using a parametric model for wake effects – a cfd simulation study. *Wind Energy*, 19(1), 1 2016.

[36] P. M. O. Gebraad, F.W. Teeuwisse, J.W. van Wingerden, P. A. Fleming, S. D. Ruben, J. R. Marden, and L. Y. Pao. A data-driven model for wind plant power optimization by yaw control. In *2014 American Control Conference*, pages 3128–3134, 2014.

[37] Pieter MO Gebraad and JW Van Wingerden. A control-oriented dynamic model for wakes in wind plants. In *Journal of Physics: Conference Series*, volume 524, page 012186. IOP Publishing, 2014.

[38] P.M.O. Gebraad, P.A. Fleming, and J.W. van Wingerden. Wind turbine wake estimation and control using floridyn, a control-oriented dynamic wind plant model. In *2015 American Control Conference (ACC)*, pages 1702–1708, 2015.

[39] F. González-Longatt, P. Wall, and V. Terzija. Wake effect in wind farm performance: Steady-state and dynamic behavior. *Renewable Energy*, 39(1):329–338, 2012.

[40] Lars Grüne. Economic receding horizon control without terminal constraints. *Automatica*, 49(3):725–734, 2013.

[41] Matthew Hall. Mooring line modelling and design optimization of floating offshore wind turbines. 2013.

[42] Chenlu Han and Ryozo Nagamune. Platform position control of floating wind turbines using aerodynamic force. *Renewable Energy*, 151:896–907, 2020.

[43] Jeffrey R. Homer and Ryozo Nagamune. Physics-based 3-d control-oriented modeling of floating wind turbines. *IEEE Transactions on Control Systems Technology*, 26(1):14–26, 2018.

[44] Tomislav Horvat, Vedrana Spudić, and Mato Baotić. Quasi-stationary optimal control for wind farm with closely spaced turbines. In *2012 Proceedings of the 35th International Convention MIPRO*, pages 829–834, 2012.

[45] Michael F. Howland, Sanjiva K. Lele, and John O. Dabiri. Wind farm power optimization through wake steering. *Proceedings of the National Academy of Sciences*, 116(29):14495–14500, 2019.

[46] International Energy Agency. Net zero by 2050: A roadmap for the global energy sector, 2021. Accessed: [Insert Date of Access].

[47] Timothé Jard and Reda Snaiki. Real-time repositioning of floating wind turbines using model predictive control for position and power regulation. *Wind*, 3(2):131–150, 2023.

[48] Niels Otto Jensen. *A note on wind generator interaction*, volume 2411. Citeseer, 1983.

[49] Ángel Jiménez, Antonio Crespo, and Emilio Migoya. Application of a les technique to characterize the wake deflection of a wind turbine in yaw. *Wind Energy*, 13(6):559–572, 2010.

[50] Kathryn E. Johnson and Geraldine Fritsch. Assessment of extremum seeking control for wind farm energy production. *Wind Engineering*, 36(6):701–715, 2012.

[51] Jason Jonkman, Sandy Butterfield, Walter Musial, and George Scott. Definition of a 5-mw reference wind turbine for offshore system development. Technical report, National Renewable Energy Lab.(NREL), Golden, CO (United States), 2009.

[52] Kai Karikomi, M Ohta, A Nakamura, S Iwasaki, Y Hayashi, and A Honda. Wind tunnel testing on negative-damped responses of a 7mw floating offshore wind turbine. *EWEA2015*, 2015.

[53] I Katic, Jørgen Højstrup, and Niels Otto Jensen. A simple model for cluster efficiency. In *European wind energy association conference and exhibition*, volume 1, pages 407–410. A. Raguzzi Rome, Italy, 1986.

[54] Ali C. Kheirabadi and Ryozo Nagamune. Modeling and power optimization of floating offshore wind farms with yaw and induction-based turbine repositioning. In *2019 American Control Conference (ACC)*, pages 5458–5463, 2019.

[55] Ali C. Kheirabadi and Ryozo Nagamune. A quantitative review of wind farm control with the objective of wind farm power maximization. *Journal of Wind Engineering and Industrial Aerodynamics*, 192:45–73, 2019.

[56] Ali C. Kheirabadi and Ryozo Nagamune. Real-time relocation of floating offshore wind turbine platforms for wind farm efficiency maximization: An assessment of feasibility and steady-state potential. *Ocean Engineering*, 208:107445, 2020.

[57] Ali C. Kheirabadi and Ryozo Nagamune. A low-fidelity dynamic wind farm model for simulating time-varying wind conditions and floating platform motion. *Ocean Engineering*, 234:109313, 2021.

[58] Ali C. Kheirabadi and Ryozo Nagamune. Real-time relocation of floating offshore wind turbines for power maximization using distributed economic model predictive control. In *2021 American Control Conference (ACC)*, pages 3077–3081, 2021.

[59] Ufuktan Kilinç. Dynamic wind farm layout optimization: To find the optimal spots for movable floating offshore wind turbines through dynamic repositioning. 2022.

[60] F. Koch, M. Gresch, F. Shewarega, I. Erlich, and U. Bachmann. Consideration of wind farm wake effect in power system dynamic simulation. In *2005 IEEE Russia Power Tech*, pages 1–7, 2005.

[61] Torben J Larsen and Tor D Hanson. A method to avoid negative damped low frequent tower vibrations for a floating, pitch controlled wind turbine. In *Journal of Physics: Conference Series*, volume 75, page 012073. IOP Publishing, 2007.

[62] Sang Lee, Matthew Churchfield, Patrick Moriarty, Jason Jonkman, and John Michalakes. Atmospheric and wake turbulence impacts on wind turbine fatigue loadings. In *50th AIAA Aerospace Sciences Meeting including the New Horizons Forum and Aerospace Exposition*, page 540, 2012.

[63] Mareike Leimeister, Athanasios Kolios, and Maurizio Collu. Critical review of floating support structures for offshore wind farm deployment. In *Journal of Physics: Conference Series*, volume 1104, page 012007. IOP Publishing, 2018.

[64] Rui Li, Jincheng Zhang, and Xiaowei Zhao. Dynamic wind farm wake modeling based on a bilateral convolutional neural network and high-fidelity les data. *Energy*, 258:124845, 2022.

[65] Yi Li, Xuan Huang, Kong Fah Tee, Qiusheng Li, and Xiao-Peng Wu. Comparative study of onshore and offshore wind characteristics and wind energy potentials: A case study for southeast coastal region of china. *Sustainable Energy Technologies and Assessments*, 39:100711, 2020.

[66] Ericka Lozon, Matthew Hall, and Mohammad Youssef Mahfouz. Coupled modeling of wake steering and platform offsets for floating wind arrays. In *Journal of Physics: Conference Series*, volume 2767, page 062035. IOP Publishing, 2024.

[67] Peter T Madsen, Magnus Wahlberg, Jakob Tougaard, Klaus Lucke, and Peter Tyack. Wind turbine underwater noise and marine mammals: implications of current knowledge and data needs. *Marine ecology progress series*, 309:279–295, 2006.

[68] Luis A Martínez-Tossas, Matthew J Churchfield, and Stefano Leonardi. Large eddy simulations of the flow past wind turbines: actuator line and disk modeling. *Wind Energy*, 18(6):1047–1060, 2015.

[69] Sara M. Maxwell, Francine Kershaw, Cameron C. Locke, Melinda G. Conners, Cyndi Dawson, Sandy Aylesworth, Rebecca Loomis, and Andrew F. Johnson. Potential impacts of floating wind turbine technology for marine species and habitats. *Journal of Environmental Management*, 307:114577, 2022.

[70] D Milborrow. Generation costs rise across the board. *Wind Power Monthly*, 2008.

[71] Doug Mills and Harvey Rosen. New jersey shore opinions about off-shore wind turbines. *Great Neck, NY, USA*, pages 1–33, 2006.

[72] H. Namik and K. Stol. Individual blade pitch control of floating offshore wind turbines. *Wind Energy*, 13(1):74–85, 2010.

[73] Hazim Namik and Karl Stol. Individual blade pitch control of a spar-buoy floating wind turbine. *IEEE transactions on control systems technology*, 22(1):214–223, 2013.

[74] Lena Neij. Cost dynamics of wind power. *Energy*, 24(5):375–389, 1999.

[75] Ahmet Ozbay, Wei Tian, Zifeng Yang, and Hui Hu. Interference of wind turbines with different yaw angles of the upstream wind turbine. In *42nd AIAA fluid dynamics conference and exhibit*, page 2719, 2012.

[76] Thanh-Dam Pham, Minh-Chau Dinh, Hak-Man Kim, and Thai-Thanh Nguyen. Simplified floating wind turbine for real-time simulation of large-scale floating offshore wind farms. *Energies*, 14(15), 2021.

[77] A. Pouliezos. 2.11 - wind turbine control systems and power electronics. In Ali Sayigh, editor, *Comprehensive Renewable Energy*, pages 329–370. Elsevier, Oxford, 2012.

[78] Steffen Raach, David Schlipf, Frank Sandner, Denis Matha, and Po Wen Cheng. Nonlinear model predictive control of floating wind turbines with individual pitch control. In *2014 American control conference*, pages 4434–4439. IEEE, 2014.

[79] Hannah Ritchie, Max Roser, and Pablo Rosado. Energy. *Our World in Data*, 2022. https://ourworldindata.org/energy.

[80] Amy Robertson, Jason Jonkman, Marco Masciola, Huimin Song, Andrew Goupee, Alexander Coulling, and C Luan. Definition of the semisubmersible floating system for phase ii of oc4. Technical report, National Renewable Energy Lab.(NREL), Golden, CO (United States), 2014.

[81] S.F. Rodrigues, R. Teixeira Pinto, M. Soleimanzadeh, Peter A.N. Bosman, and P. Bauer. Wake losses optimization of offshore wind farms with moveable floating wind turbines. *Energy Conversion and Management*, 89:933–941, 2015.

[82] Tom Salic, Jean Frédéric Charpentier, Mohamed Benbouzid, and Marc Le Boulluec. Control strategies for floating offshore wind turbine: Challenges and trends. *Electronics*, 8(10), 2019.

[83] Michele Samorani. *The wind farm layout optimization problem.* Springer, 2013.

[84] Filipe Duarte Santos, Paulo Lopes Ferreira, and Jiesper Strandsbjerg Tristan Pedersen. The climate change challenge: A review of the barriers and solutions to deliver a paris solution. *Climate*, 10(5), 2022.

[85] Rabia Shakoor, Mohammad Yusri Hassan, Abdur Raheem, and Yuan-Kang Wu. Wake effect modeling: A review of wind farm layout optimization using jensen's model. *Renewable and Sustainable Energy Reviews*, 58:1048–1059, 2016.

[86] Carl R. Shapiro, Pieter Bauweraerts, Johan Meyers, Charles Meneveau, and Dennice F. Gayme. Model-based receding horizon control of wind farms for secondary frequency regulation. *Wind Energy*, 20(7):1261–1275, 2017.

[87] Carl R Shapiro, Dennice F Gayme, and Charles Meneveau. Modelling yawed wind turbine wakes: a lifting line approach. *Journal of Fluid Mechanics*, 841:R1, 2018.

[88] M. Steinbuch, W.W. de Boer, O.H. Bosgra, S.A.W.M. Peters, and J. Ploeg. Optimal control of wind power plants. *Journal of Wind Engineering and Industrial Aerodynamics*, 27(1):237–246, 1988.

[89] David Stockhouse, Mandar Phadnis, Aoife Henry, Nikhar Abbas, Michael Sinner, Manuel Pusch, and Lucy Y. Pao. Sink or swim: A tutorial on the control of floating wind turbines. In *2023 American Control Conference (ACC)*, pages 2512–2529, 2023.

[90] B Mutlu Sumer et al. *Hydrodynamics around cylindrical strucures*, volume 26. World scientific, 2006.

[91] The MathWorks, Inc. *MATLAB Optimization Toolbox: fmincon.* The MathWorks, Inc., Natick, Massachusetts, 2023. Accessed: 2023-06-19.

[92] Kenneth Thomsen and Poul Sørensen. Fatigue loads for wind turbines operating in wakes. *Journal of Wind Engineering and Industrial Aerodynamics*, 80(1):121–136, 1999.

[93] Zilong Ti, Xiao Wei Deng, and Hongxing Yang. Wake modeling of wind turbines using machine learning. *Applied Energy*, 257:114025, 2020.

[94] Emmanuel Trélat and Enrique Zuazua. The turnpike property in finite-dimensional nonlinear optimal control. *Journal of Differential Equations*, 258(1):81–114, 2015.

[95] United Nations Framework Convention on Climate Change. The paris agreement, Accessed 2023. [Online; accessed 7-December-2023].

[96] Maarten T. van Beek, Axelle Viré, and Søren J. Andersen. Sensitivity and uncertainty of the floris model applied on the lillgrund wind farm. *Energies*, 14(5), 2021.

[97] M. J. van den Broek, M. Becker, B. Sanderse, and J.-W. van Wingerden. Dynamic wind farm flow control using free-vortex wake models. *Wind Energy Science*, 9(3):721–740, 2024.

[98] Daan van der Hoek, Stoyan Kanev, Julian Allin, David Bieniek, and Niko Mittelmeier. Effects of axial induction control on wind farm energy production - a field test. *Renewable Energy*, 140:994–1003, 2019.

[99] Mike T. van Dijk, Jan-Willem van Wingerden, Turaj Ashuri, and Yaoyu Li. Wind farm multi-objective wake redirection for optimizing power production and loads. *Energy*, 121:561–569, 2017.

[100] Longyan Wang, Andy Tan, and Yuantong Gu. A novel control strategy approach to optimally design a wind farm layout. *Renewable Energy*, 95:10–21, 2016.

[101] Shengwen Xu, Motohiko Murai, Xuefeng Wang, and Kensaku Takahashi. A novel conceptual design of a dynamically positioned floating wind turbine. *Ocean Engineering*, 221:108528, 2021.

[102] Yue Yao, Jin-Hua Xu, and De-Qiang Sun. Untangling global levelised cost of electricity based on multi-factor learning curve for renewable energy: Wind, solar, geothermal, hydropower and bioenergy. *Journal of Cleaner Production*, 285:124827, 2021.

[103] Jincheng Zhang and Xiaowei Zhao. A novel dynamic wind farm wake model based on deep learning. *Applied Energy*, 277:115552, 2020.

[104] Jincheng Zhang and Xiaowei Zhao. Quantification of parameter uncertainty in wind farm wake modeling. *Energy*, 196:117065, 2020.

Glossary

List of Acronyms

TLP	Tension Leg Platform
CFD	Computational Fluid Dynamics
LES	Large Eddy Simulation
SOWFA	Simulator fOr Wind Farm Applications
FLORIS	FLOw Redirection and Induction in Steady-state
FAST	Fatigue, Aerodynamics, Structures, and Turbulence
FLORIDyn	FLOw Redirection and Induction Dynamics
OP	Observation Point
TWF	Temporary Wind Farm
TSR	Tip-speed ratio
DPS	Dynamic Positioning System
TRTLE	Turbine Repositioning Technique for Layout Economics
MPC	Model Predictive Control
NREL	National Renewable Energy Laboratory
AM	After the Movement
BM	Before the Movement
SQP	Sequential quadratic programming
MW	Megawatt
FFT	Fast Fourier Transform